Title
NUCLEAR MATERIALS RESEARCH PROGRESS REPORTS FOR 1978

Author
Olander, D.R.

Publication Date
1978-12-01

Lawrence Berkeley Laboratory
UNIVERSITY OF CALIFORNIA

Materials & Molecular Research Division

NUCLEAR MATERIALS RESEARCH PROGRESS REPORTS FOR 1978

D. R. Olander

December 1978

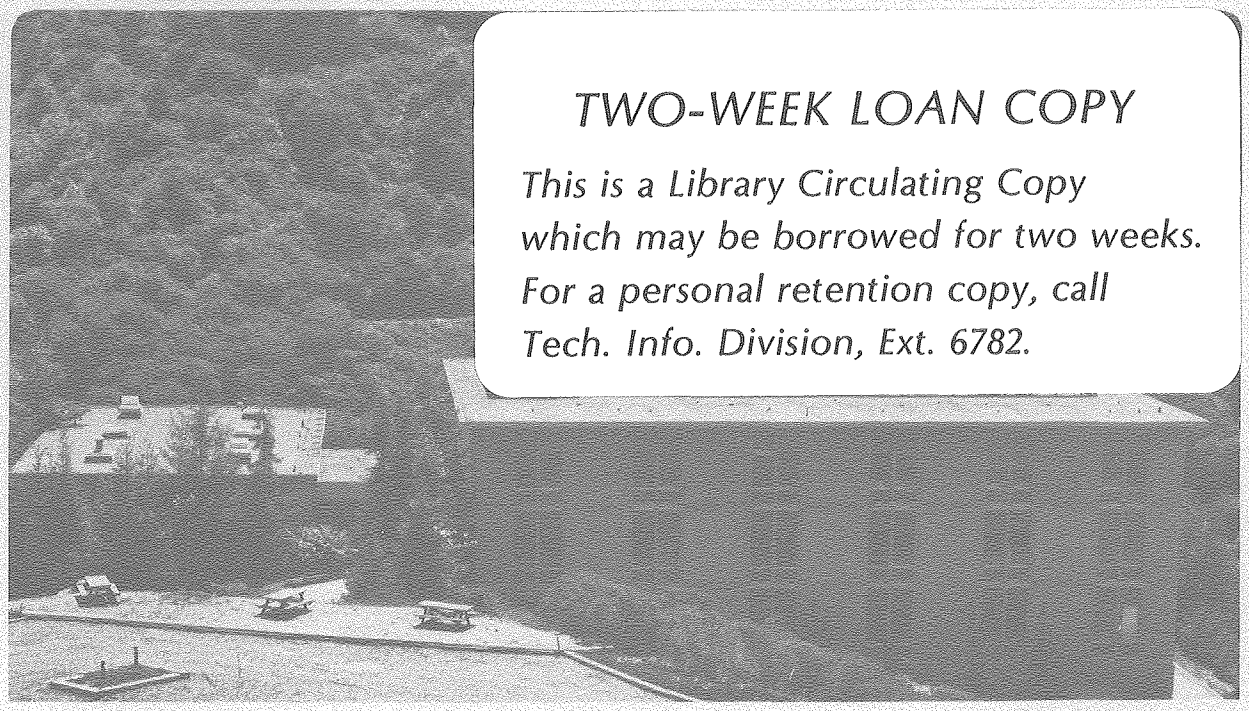

Prepared for the U.S. Department of Energy under Contract W-7405-ENG-48

DISCLAIMER

LBL-10375

NUCLEAR MATERIALS RESEARCH PROGRESS REPORTS

FOR 1978

Materials and Molecular Research Division
Lawrence Berkeley Laboratory
University of California
Berkeley, California 94720

D. R. Olander,
Principal Investigator

This work was supported by the U. S. Department of Energy under Contract W-7405-ENG-48

CONTENTS

IODINE STRESS CORROSION CRACKING OF ZIRCALOY

by Shih-Hsiung Shann
[December 1978]

I. INTRODUCTION

The outstanding high temperature water corrosion resistance and highly desirable nuclear characteristics of zircaloy have made it an excellent cladding material of light water reactors. However, low-ductility failures of the cladding still occasionally occur, pointing to the need for understanding of the fracture mechansim and prevention methods.

The temperature range of fuel cladding eliminates the possibility of liquid metal embrittlement(7), and the fractography of cracked cladding resembles that of stress corrosion cracking in the laboratory (7). Previous works (1-12, 23, 24) have been studied mainly unirradiated specimens in iodine and Wood et.al. (6.11) tested irradiated samples, but nothing concerning simultaneous irradiation and stress corrosion has been reported.

Iodine is present as low yield fission product in irradiated fuel rods. However, according to thermodynamics, all of this iodine should be combined with the more abundant fission product cesium to produce the stable solid CsI. This substance is not an active stress corrosion cracking agent to zircaloy, as demonstrated by out-of-pile tests (8,23). The main purpose of this project is to determine how iodine is released from CsI inside the fuel rod in order to activate the stress corrosion cracking process. Our hypothesis is that the strong radiation field inside the fuel rod decomposes the thermodynamically stable CsI (14) and liberates enough free iodine to permit stress corrosion cracking to occur. To achieve this long-range objective, establishment of a complete iodine-zircaloy stress corrosion cracking data base is necessary for a reference system and for better understanding of fracture mechanism.

II. EXPERIMENTAL

The present experiment utilizes a tube-burst (biaxial) test mode. One half

inch OD tube samples (ground to 10 mil wall thickness) internally pressurized by argon are connected to a pressure transducer (Statham PA-891-3M) and a filling valve (Fig. 1). The assembly is placed in an enclosure and heated resistively.

For temperature measurement and control, a thermocouple is pushed against the zircaloy tube by a stainless steel spring, the force of which is enough for the good contact between thermocouple and zircaloy, but is too small to cause indentation of the tube. Thin thermocouple wire (0.01" diameter) is used in order to keep the heat loss through thermocouple wires as small as possible. An electronic control system (Omega Engineer, Inc. Model 49) has been installed to compare the output voltage of the thermocouple with preset standard and to operate a relay in order to turn on or turn off the heating current. The temperature can be controlled within $\pm$ 5°C of the set temperature.

The tube is pressurized by an inert gas prior to closing the filling valve and inserting into the vacuum system. The initial hoop stress in the zircaloy tube is calculated from the thin-wall tube formula

$$\sigma_o = \frac{PR}{w} \qquad (1)$$

where σ_o = initial hoop stress

P = internal gas pressure

R = tube radius

W = tube wall thickness

As the crack propagates, the net section thickness (initial wall thickness-crack length) decreases, and the stress increases. To prevent damage to the diffusion pump following a burst of the internally pressurized test specimen, a loose-fitting glass rod is inserted in the tube specimen to reduce the gas volume. When the specimen fails, <0.01 moles of gas flow into the vacuum system.

Molecular iodine is supplied to the surface through 4.57 mm diameter tubing (doser) which is 2-5 mm from the specimen surface. With this delivery system, iodine impinges on a spot ~5 mm in diameter on the outside surface of the zircaloy specimen.

The iodine flow rate ℓ^* (moles/sec) through the doser is calculated from Shock's model (17) for flow through small diameter, long tubes.

$$\frac{L}{D} = \frac{\sqrt{\frac{1}{2}\pi}}{64} \left[(\dot{m}^{-1} - \dot{m} + 2\dot{m} \log \dot{m})\ p_1 + 22(1 - \dot{m})^2/\dot{m} \right]$$

where:

D = diameter of doser tube

L = length of doser tube

$\dot{m}$ = mass flow rate

p_1 = dimensionless pressure at tube inlet

$$p_1 = \frac{P_1}{\sqrt{\frac{1}{2}\pi RT}\ (\mu/D)}$$

P_1 = pressure at tube inlet (iodine reservoir)

μ = viscosity

The intensity I^* (moles/cm^{2}sec) of iodine impinging on the surface of the tube at a distance d from the outlet of doser is given by

$$I^* = \frac{\chi(\dot{m}/254)}{\pi d^2}$$

where χ is the peaking factor (18), which characterizes noncosine emission from long channels.

The equivalent pressure of iodine at the zircaloy surface (P_{eq}) is calculated from

$$I^* = \frac{P_{eq}}{\sqrt{2\pi mkT}}$$

where m = molecular weight of iodine

k = gas constant

T = temperature

Two lots of stress relieved zircaloy-2 were tested. One lot was obtained from Stanford Research Institute with unknown lot number (O.D. = 0.503", I.D. = 0.453"), the other lot was purchased from Sandvik Special Metals, lot number 9AX32 (O.D. = 0.486 ±0.002", I.D. = 0.414"±0.002"). Table 1 gives the chemical composition.

III. RESULTS

A. Failure Modes

With iodine, specimens exhibited pinhole-type failure (Figs. 2-6), which was completely different from the burst-type failure which occurs in the absence of iodine (Fig. 7).

The Sandvik specimens, with stress level between 54ksi and 42ksi, all fractured in the pinhole mode. Three specimens with stress ≥55ksi fractured in non-pinhole mode, even in the presence of iodine.

The fractography of pinhole and ductile failures are completely different. Fig. 8 is a scanning electron micrograph of a pinhole type failure. Fig. 9 is for ductile failure. Fig. 10 shows that besides the penetrating cracks, there are a number of non-penetrating cracks on the outside surface in the iodine-affected region. There are numerous small cracks branching out from main crack at an angle to main crack propagation direction (Fig. 11). As the main crack propagates, the remaining intact wall thickness decreases, so the net section stress increases. After the crack length reaches a critical length, a transition to ductile failure occurs (Fig. 12) when the net section stress reaches the ultimate tensile stress and the tube fails immediately. A few grains fail by cleavage, as shown in Fig. 13. Fig. 14 is a detail of Fig. 13.

B. Time to Rupture

The results from unflawed specimens from SRI are plotted in Fig. 15. Pre-flawed (0.001" depth, 1" long notches) data are shown in Fig. 16. Stress corrosion cracking was observed at iodine pressure as low as 10^{-3} torr.

Control specimen results for the Sandvik tubes at 300°C are shown in Fig. 17. Fig. 18 gives the time-to-failure versus temperature for 0.05 torr iodine pressure. Fig. 19 and 20 record the times to failure versus stress for two different iodine pressures. Fig. 21 is a time-to-failure/equivalent iodine pressure relationship.

The iodine pressure necessary to cause stress corrosion cracking is much less than previously reported(19).

IV. DISCUSSION

A. Iodine Concentration

Most previous works use mg/cm^2 as a unit to describe the iodine potential. According to basic chemistry, the partial pressure is the correct measure of chemical potential. Une(19) performed experiments with different volume-to-surface ratios, keeping one variable constant and changing the other. The influence of two variables on the time to failure was recorded. He concluded that in zircaloy stress corrosion cracking, iodine partial pressure (e.g., torr), not the surface density (mg/cm^2) is the correct unit for correlating the stress corrosion cracking phenoemnon.

Let us consider the experimental methods for establishing the iodine concentration used in previous investigations:

(a) A fixed amount of iodine is sealed in the inside of zircaloy tube (23). In this case, there is considerable surface other than zircaloy on which iodine can plate out. In addition, only the zircaloy is heated and the iodine will condense on the cold regions of the system. The actual iodine

responsible for stress corrosion cracking is much lower than what is reported.

(b) A fixed amount of iodine is sealed inside the zircaloy tube, and the tube is plugged at both ends (1, 4, 5, 8, 24), or iodine is sealed with zircaloy in closed system, as in some mandrel tests (6, 7, 11). In those cases, the amount of iodine first decreases with time. After certain period, there may be an equilibrium between iodine and zircaloy. But we do not know what the equilibrium iodine pressure is, or how long it will take to achieve the equilibrium.

From the discussion above, it is clear that in previous investigations, insufficient attention has been given to maintaining contant, known iodine concentration or even using the correct units to describe the iodine concentration.

B. Biaxiality

In our specimen assembly (Fig. 1), one end is free. Under internal pressure, the hoop-axial stress ratio is two (in other works, the ratio is between 0.5 and 1 (8) or not given). The yielding condition of anisotropic materials such as zircaloy under biaxial loading depends on the ratio of two principal stresses (15, 20), so a hoop stress measurement alone is not a sufficient condition for fixing the time to failure. The time to failure can change with different stress biaxiality ratios even though the hoop stress, iodine pressure, and temperature are fixed.

C. Stress and Iodine Pressure Thershold

One Sandvik specimen, held at 300°C and 47.6 Kpsi, did not fail after 89 hours at an iodine pressure of .013 torr. A possible explation is that the stress was below the threshold stress for stress corrosion cracking for the particular iodine partial pressure used. Alternatively, the iodine pressure was

below the threshold value for that stress level. The threshold concepts are accepted by most previous workers (1-12, 23). The threshold concept implies a change in fracture mechanism in narrow ranges of stress and iodine pressure, so that time to failure is greatly affected.

D. High Stress Failure

Three Sandvik specimens stressed near 55Ksi did not exhibit pinhole type failure under iodine. The argument that stress corrosion cracking can occur only within a limited stress range (21) can explain this phenomenon. According to this explanation, stress of 55Ksi is too high for pinhole-type stress corrosion cracking.

E. Data Correlation

Stress corrosion cracking of zircaloy is a low ductility fracture process (strain in the range of a few percent). If crack propagation dominates the life-time of specimens, the model of slow crack growth under chemical attack for brittle solid may be applied to this situation(22).

In this model, the crack growth rate is described in chemical reaction rate terminology by:

$$\frac{da}{dt} = A[P_{eq}]^n \exp(-\frac{E^*}{RT}) F(K) \qquad (2)$$

where a = crack length

E* = activation energy of the chemical step responsible for stress corrosion

n = reaction order

A = constant

F in Eq.(2) is the functional dependence of the crack growth rate on the stress intensity factor, which is

$$K = Y\sigma\sqrt{a} \tag{3}$$

Y = geometric factor

The hoop stress in the intact section of the wall is:

$$\sigma = \sigma_o \frac{w}{w-a} \tag{4}$$

where σ_o = initial hoop stress (see eq. 1)

w = initial wall thickness

$w-a$ = intact wall thickness

Integrating Eq 2:

$$t_f = \frac{1}{A\ [P_{eq}]^n} \exp\left(\frac{E^*}{RT}\right) \int_{a_o}^{a_c} \frac{da}{F(K)} \tag{5}$$

a_o = initial length of the crack pre-existing through manufacture or machining ($a_o \approx 0.22 \times 10^{-3}$ in)

a_c = crack length at which the section stress is equal to the ultimate tensile stress:

$$\frac{\sigma_o w}{(w-a_c)} = \sigma_{UTS} \tag{6}$$

Here it is supposed that stress corrosion propagates the crack from length a_o to a_c where ductile failure takes place very rapidly. This final process can be seen on the SEM picture of Fig. 12.

Least square curve fittion of the T and P_{eq} data gives:

$$E^* = 7.12 \pm 0.9 \text{ Kcal/mole} \tag{7}$$

$$n = 0.51 \pm .03 \tag{8}$$

Three crack velocity and stress intensity factor relations (22) were tried:

$$F(K) = \exp\left(\frac{BK}{T}\right) \tag{9}$$

$$F(K) = K^m \tag{10}$$

$$F(K) = \exp(-B/K) \tag{11}$$

where B and m are constants. These relationships all fit the stress-dependence data to the same accuracy. $F(K) = K^m$ case gives $m = 4.0 \pm 0.1$, which is consistent with the results of Tuck, et.al. (5) and Polan et.al. (24).

V. PLANNED EXPERIMENTS

A. Perform the experiment using FeI_2, AlI_3, ZrI_4, and CsI, to see if these species, cause stress corrosion cracking.

B. Determine whether crack initiation or crack propagation is the slow step. We plan to use a camera to record the surface condition during the experiment, in order to determine when the surface crack first appears on the specimen. If this method does not work (i.e., if the resolution of the film is not good enough), we will have to use several specimens exposed to iodine for different time periods and removed them from the system for inspection of crack length.

C. Apply stress, CsI (or other corrosive agent), and radiation simultaneously to the zircaloy specimen to see if radiation liberates iodine and causes stress corrosion cracking.

REFERENCES

1. C. C. Busby, R. P. Tucker and J. E. McCauley, J. Nucl. Mater., 55 (1975) 64-82.

2. A. Garlick and P. D. Wolfenden, J. Nucl. Mater., 41 (1971) 274-272.

3. P. H. Kreyns, G. L. Spahr and J. E. McCanley, WAPD-TM-1203. (1976)

4. J. G. Weinberg, WAPD-TM-1048. (1974)

5. R. P. Tucker, P. H. Kreyns and J. J. Kearns, WAPD-TM-1248.

6. J. C. Wood, J. Nucl. Mater., 45 (1972/1973) 105-122.

7. J. C. Wood, B. A. Surette, I. M. London and J. Baird, J. Nucl. Mater., 57, (1975) 155-197.

8. K. Videm and L. Lunde, Annals of Nuclear Energy, 3 (1976) 305-313.

9. I. Aitchison and B. Cox, Corrosion, 28 (1972) 83-87.

10. B. Cox, Corrosion, 28 (1972) 207-217.

11. J. C. Wood, Nucl. Technology, 23 (1974) 63-79.

12. A. Garlick, J. Nucl. Mater., 49 (1973/74) 207-224.

13. K. Elayaperumal, P. K. De and J. Balachandra, J. Nucl. Mater., 45 (1972/73) 323-330.

14. D. Cubicciotti and J. H. Davis, Nuclear Science and Engineering, 60 (1976) 314-319.

15. W. A. Backofon, W. F. Hosford, Jr. and J. J. Burke, Trans. ASM, 1962, 264-267.

16. R. A. Gough, R. Lam, C. Martinez and D. Morris, Nuclear Instruments and Methods, 138 (1976) 415-419.

17. A. Schock, FSEC-NSG-217-74/37B (1974).

18. D. R. Olander and R. H. Jones, Entropie, No. 30, Nov./Dec. 1969, 42-47.

19. Katsumi Une, J. of Nucl. Sci. and Tech., 14 (1977) 443-451.

20. E.I.H. Lin, Trans. ANS, 27 (1977) 597-599.

21. W. J. Baily, C. L. Wilson, L. J. MacGowan and P. J. Pankaskie, COO-4066-2, PNL-2488, UC-78 (1977).

22. A. G. Evans and T. G. Longdon, Progress in Materials Science, 21 3/4 (1976).

23. D. Cubicciotti and R. L. Jones, EPRI NP-717 (1978).

24. N. W. Polan and R. P. Tucker, WAPD-1313 (1977).

Table 1. Composition of Sandvik Zr-Z (9AX-32)

INGOT ANALYSIS

COMPOSITION IN PERCENT

	Spec.	Top	Middle	Bottom
Sn	1.20-1.70	1.55	1.47	1.46
Fe	0.07-0.20	0.14	0.13	0.14
Cr	0.05-0.15	0.10	0.09	0.09
Ni	0.03-0.08	0.05	0.04	0.04
Fe+Cr+Ni	0.18-0.38	0.29	0.27	0.28
Zr	B A L A N C E			

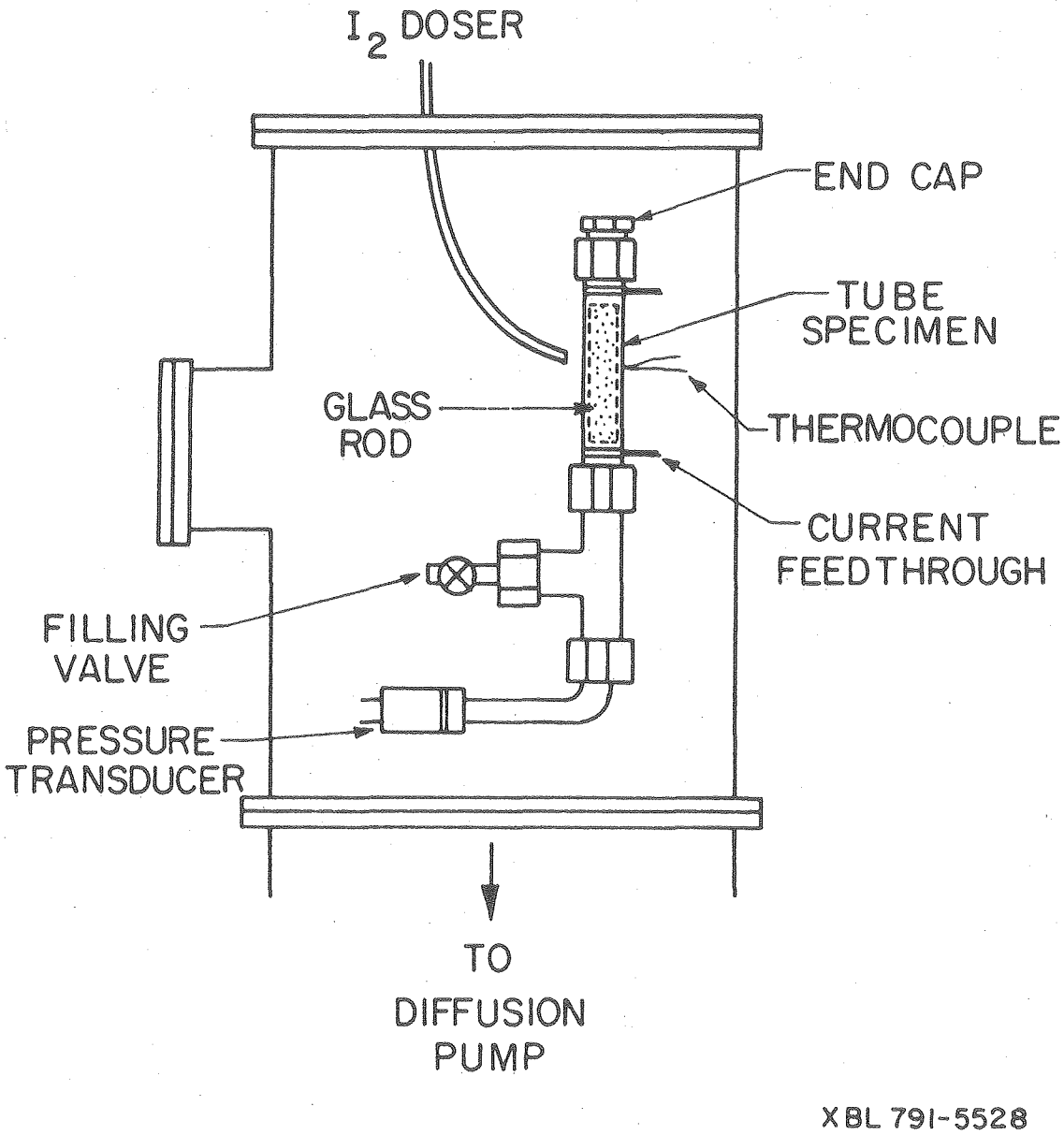

Figure 1. Stress corrosion cracking apparatus.

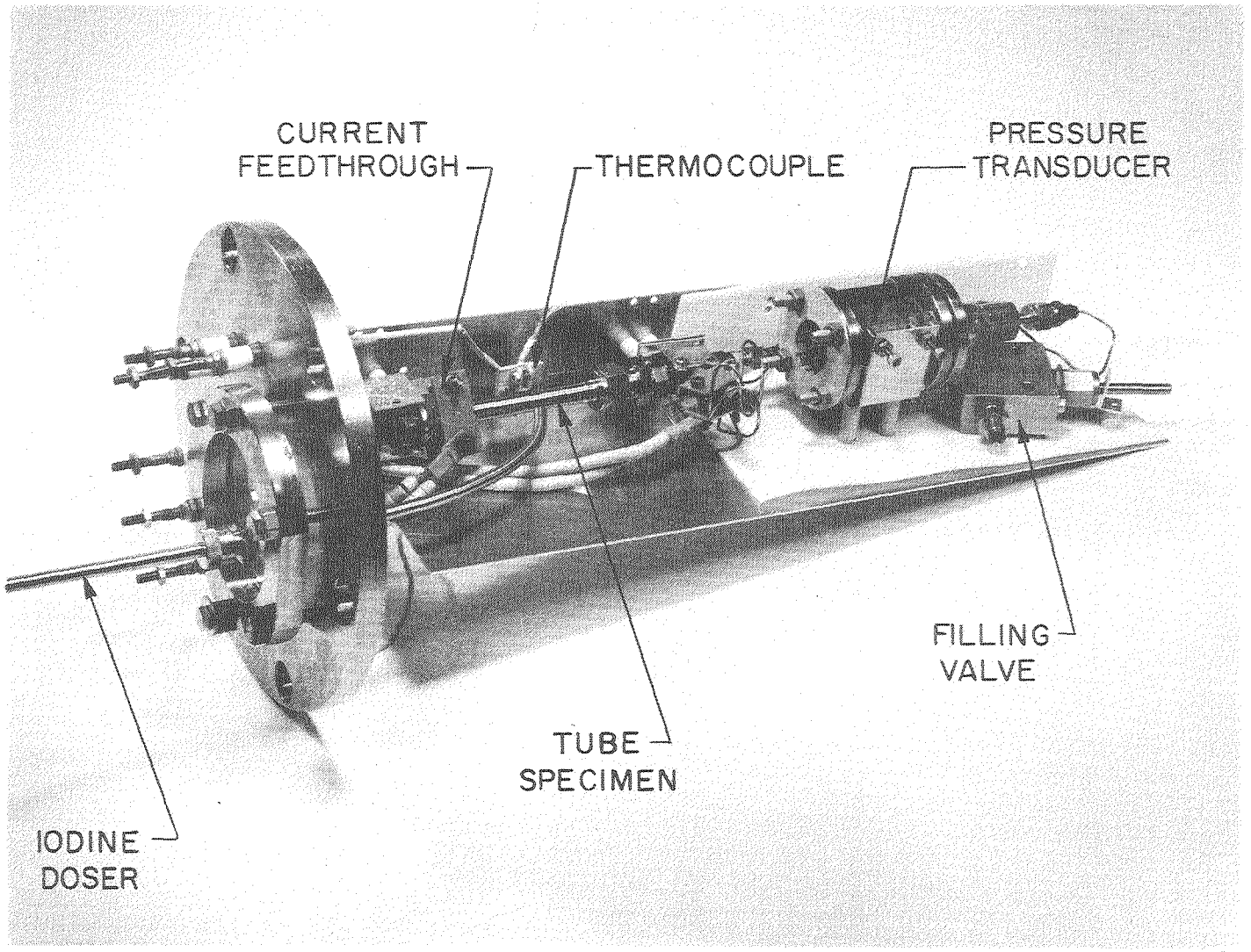

CBB 795-6560A

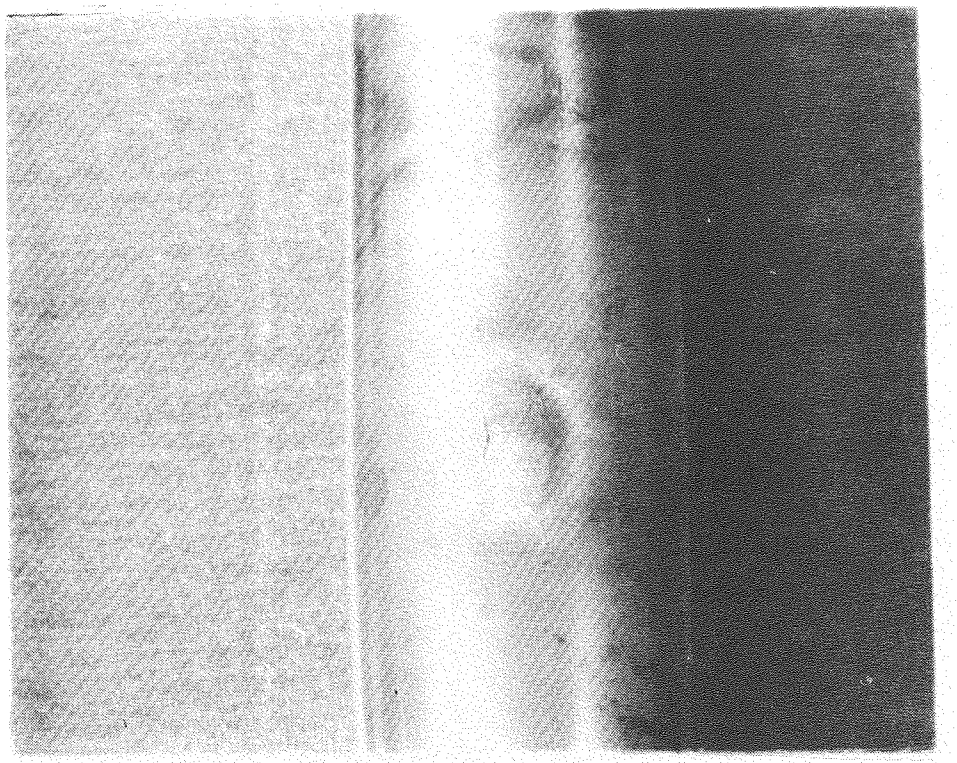

XBB791-473

Figure 2. Stress-relieved Zr-Z (Sandvik lot no. 9AX32) failed after 13.17 hrs under 45.8 Ksi and 0.05 torr iodine at 300°C.

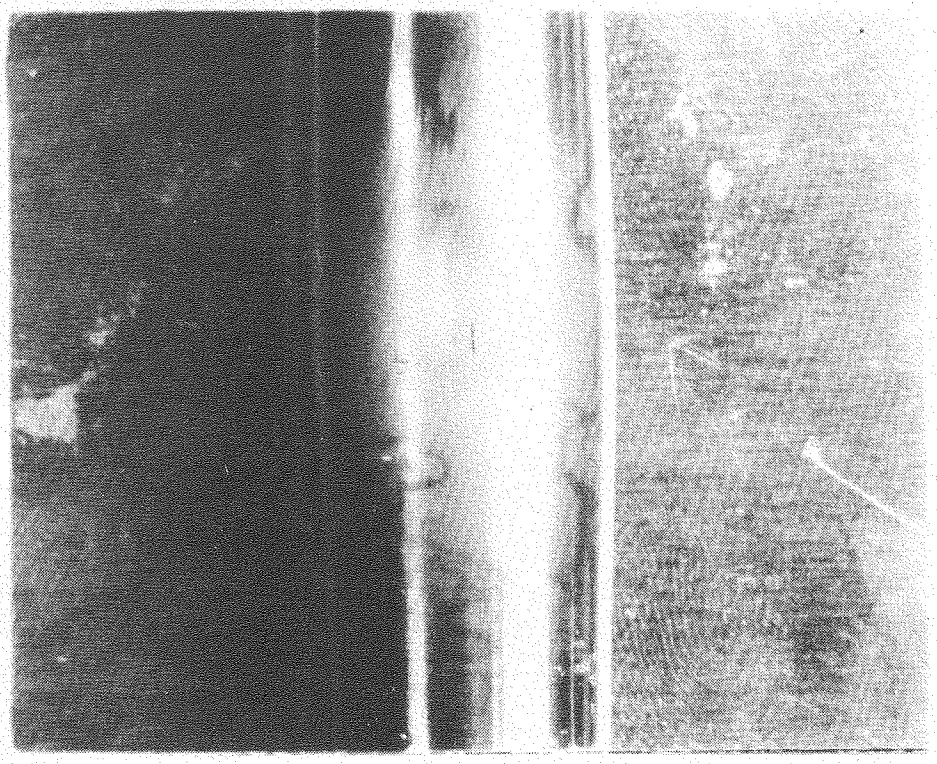

XBB791-482

Figure 3. Stress-relieved Zr-2 (Sandvik lot no. 9AX32) failed after 5.02 hrs under 53.5 Ksi and 0.05 torr iodine at 300°C.

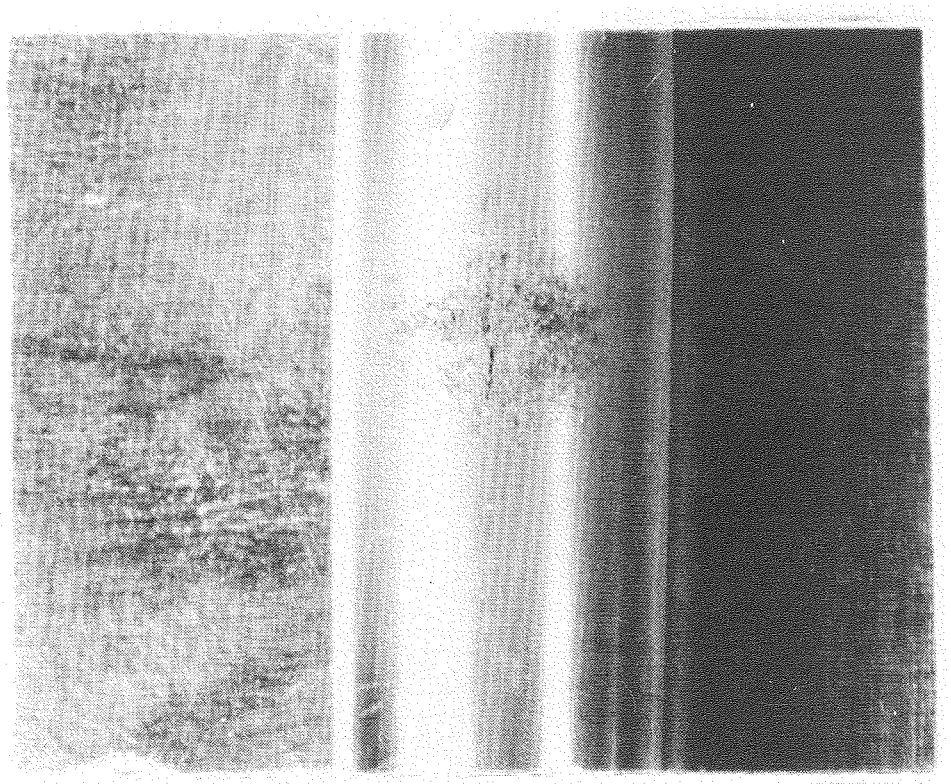

XBB791-474

Figure 4. Stress-relieved Zr-2 (Sandvik lot no. 9AX32) failed after 9.01 hrs under 53.5 Ksi and 0.032 torr iodine at 300°C.

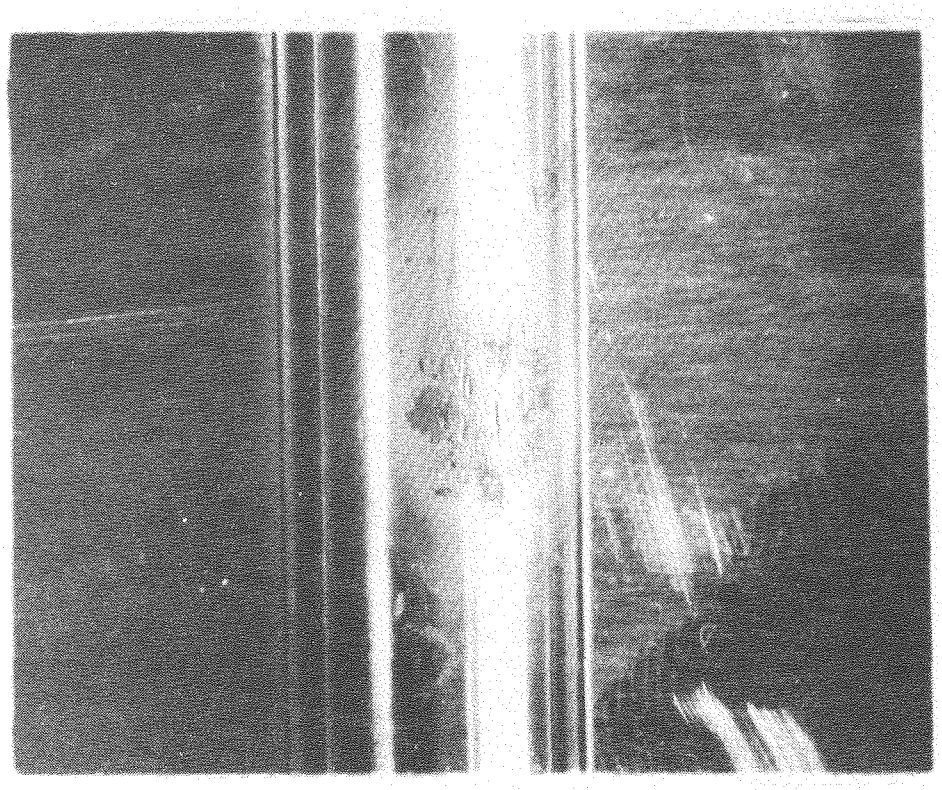

XBB791-476

Figure 5. Stress-relieved Zr-2 (Sandvik lot no. 9AX32) failed after 3.23 hrs under 47.0 Ksi and 0.16 torr iodine at 325°C.

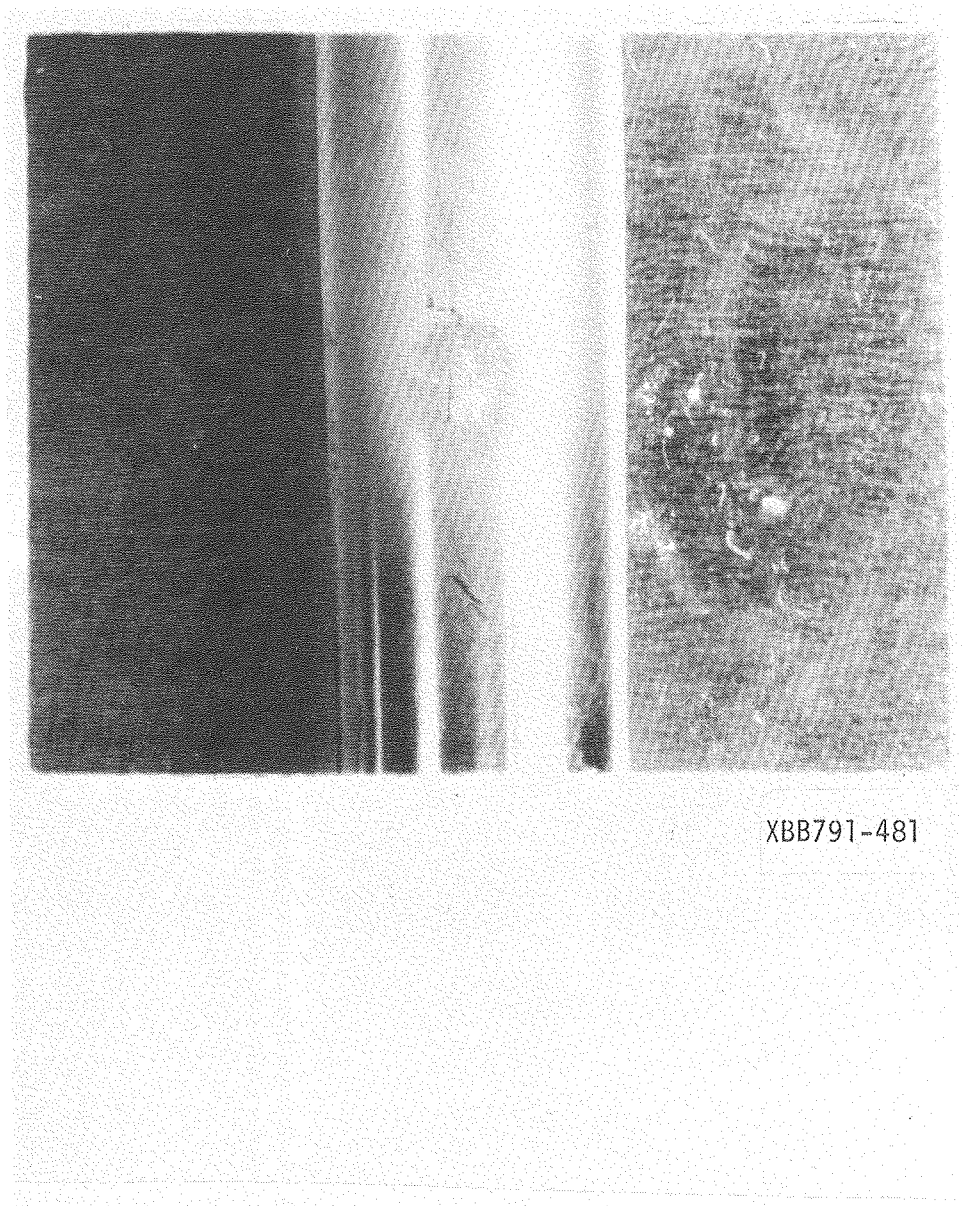

Figure 6. Stress-relieved Zr-2 (Sandvik lot no.9AX32) failed after 17.03 hrs under 45.1 Ksi and 0.05 torr iodine at 270°C.

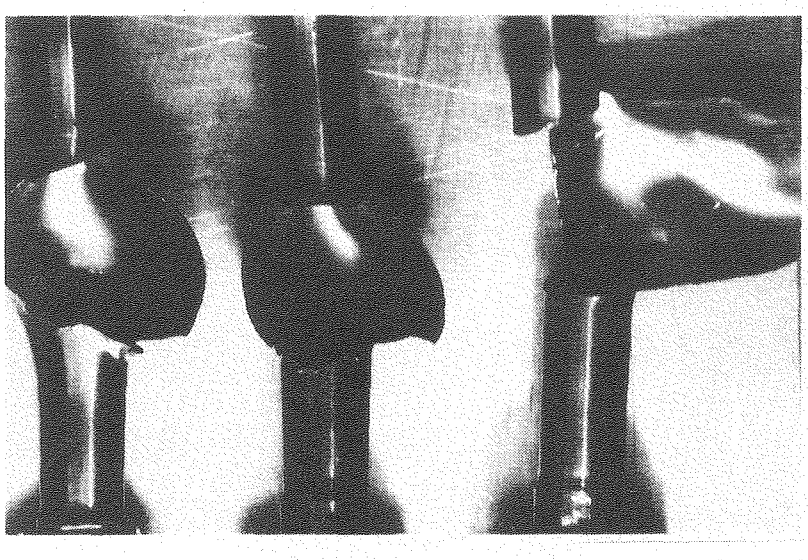

XBB 791-329A

Figure 7. Control specimens of Sandvik lot no. 9AX32 ruptured at 300°C without iodine at stresses of 55.5, 53.6, and 49.7 Ksi.

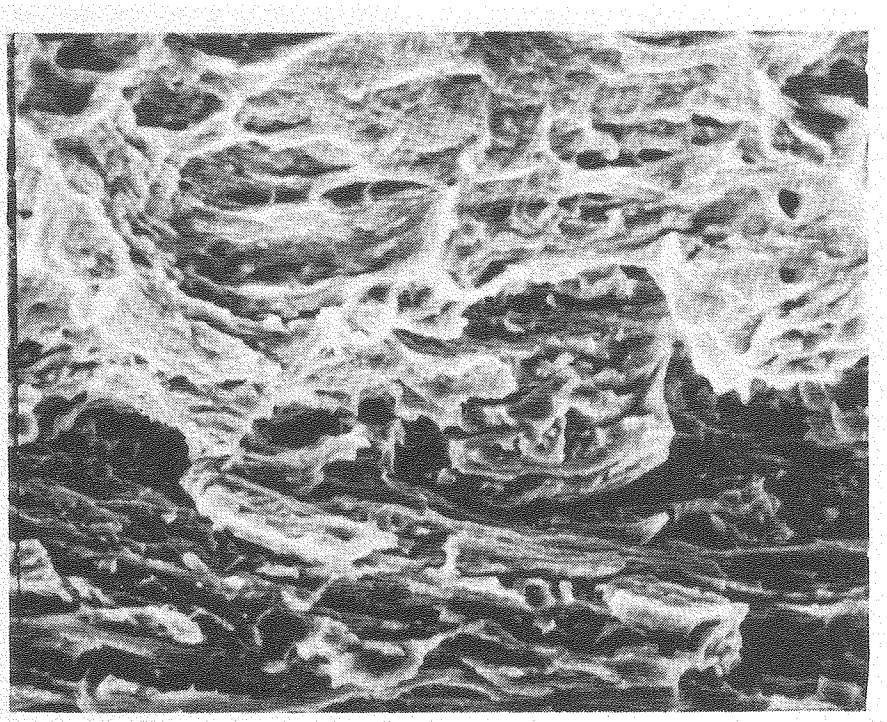

10 μ

XBB 791-309A

Figure 8. SEM fractography of pin-hole type failure (preflawed stress relieved Zr-2 from SRI) failed after 20.5 hrs, 52.3 Ksi, 0.017 torr iodine at 320°C.

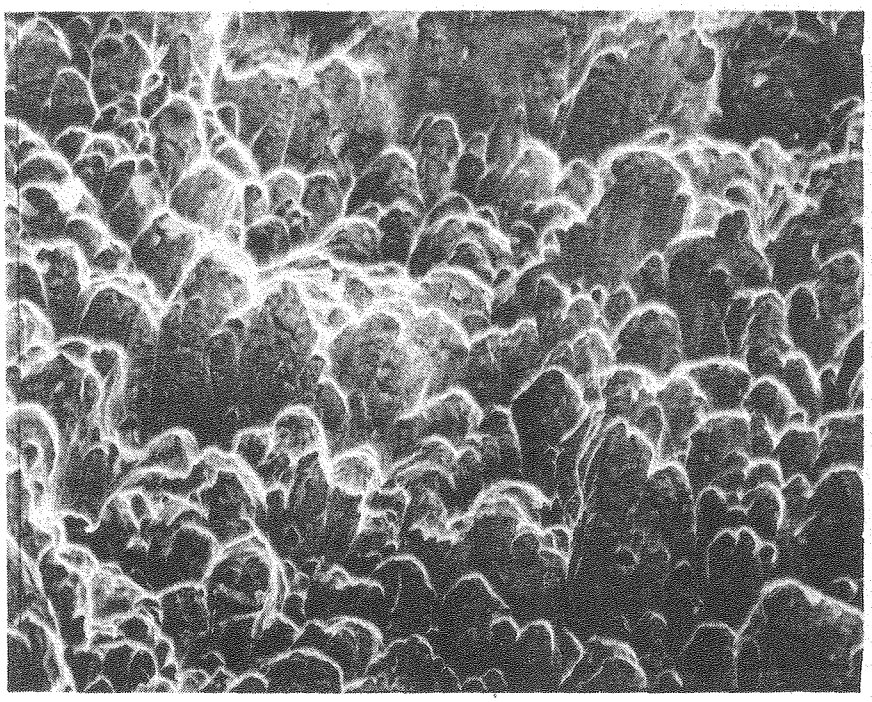

20 μ

XBB 791-314A

Figure 9. SEM fractography of ductile failure (unflawed, stress-relieved Zr-2 from SRI) failed after 51.8 hrs; 320°C, without iodine.

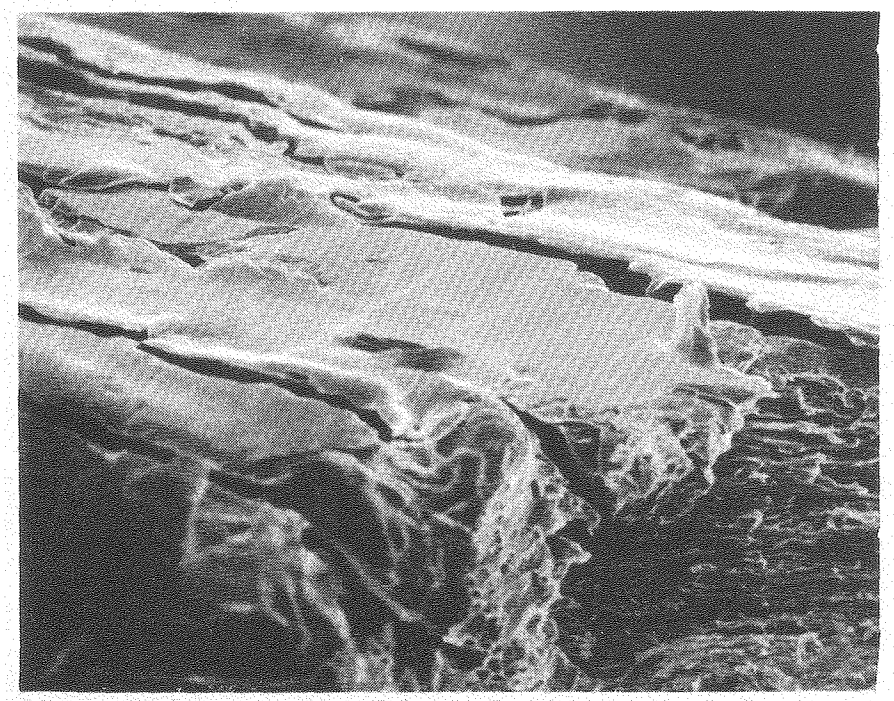

40 μ

XBB 791-312A

Figure 10. Besides main penetrating crack, there are alot of small cracks in iodine-affected area. (Preflawed stress-relieved Zr-2 from SRI failed after 59.3 hrs, 52.3 Ksi, 0.045 torr iodine, 320°C.)

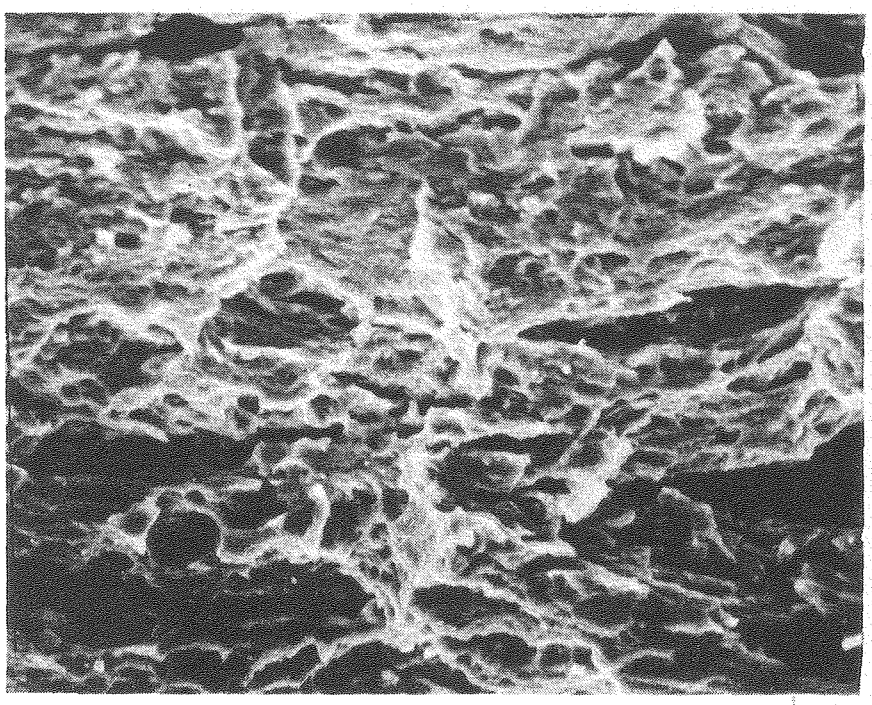

10 μ

XBB 791-308A

Figure 11. Same specimen as Fig. 10 showing many small cracks branching out from main crack.

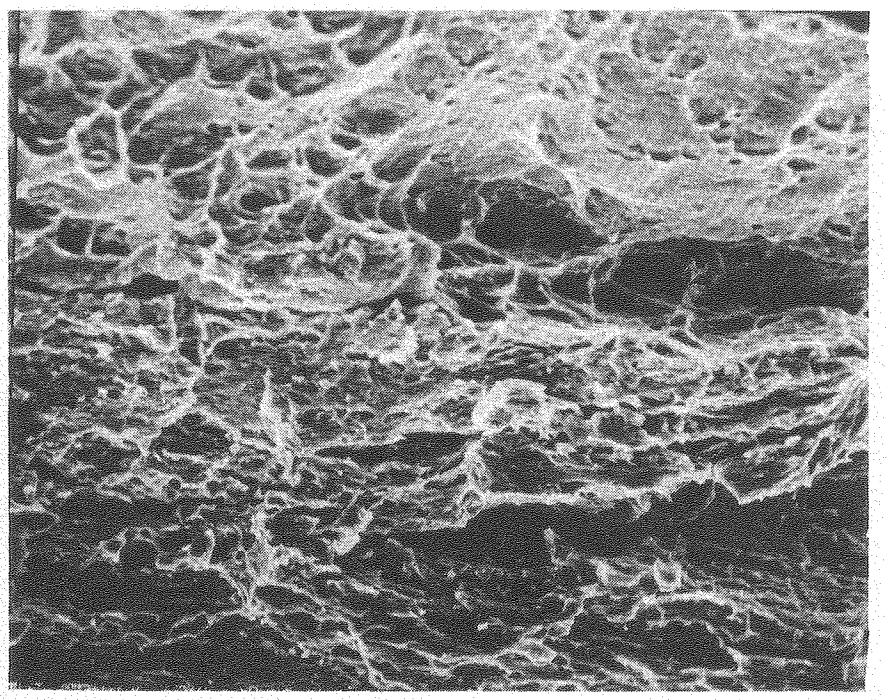

20 μ

XBB 791-311A

Figure 12. Transition from brittle mode to ductile (dimple) mode.

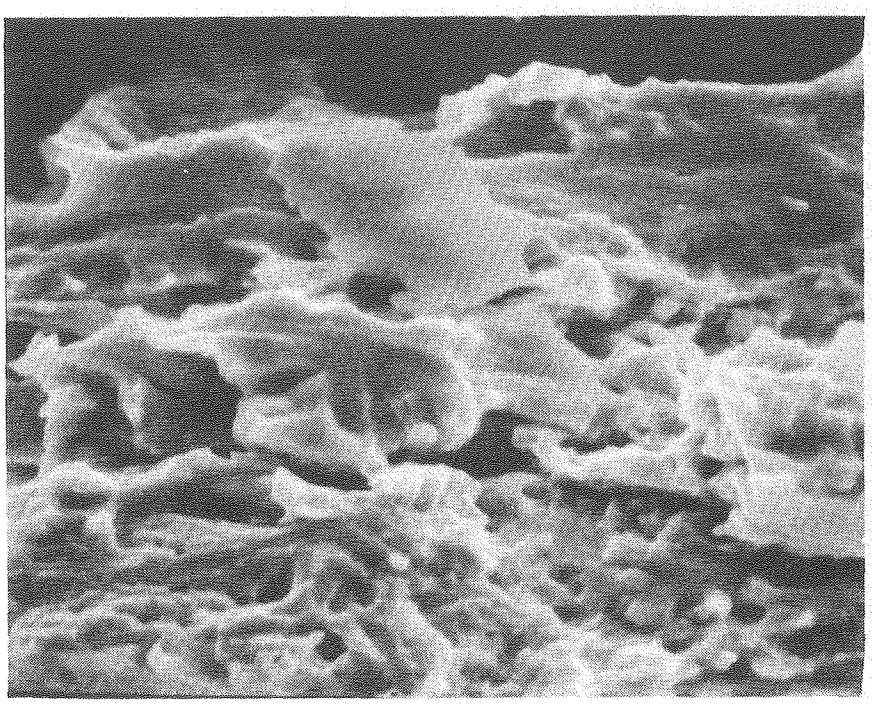

4 μ

XBB 791-315A

Figure 13. Grain failed by cleavage (preflawed stress-relieved Zr-2 from SRI) failed after 5.93 hrs; 52.3 Ksi, 0.045 torr iodine, 320°C.

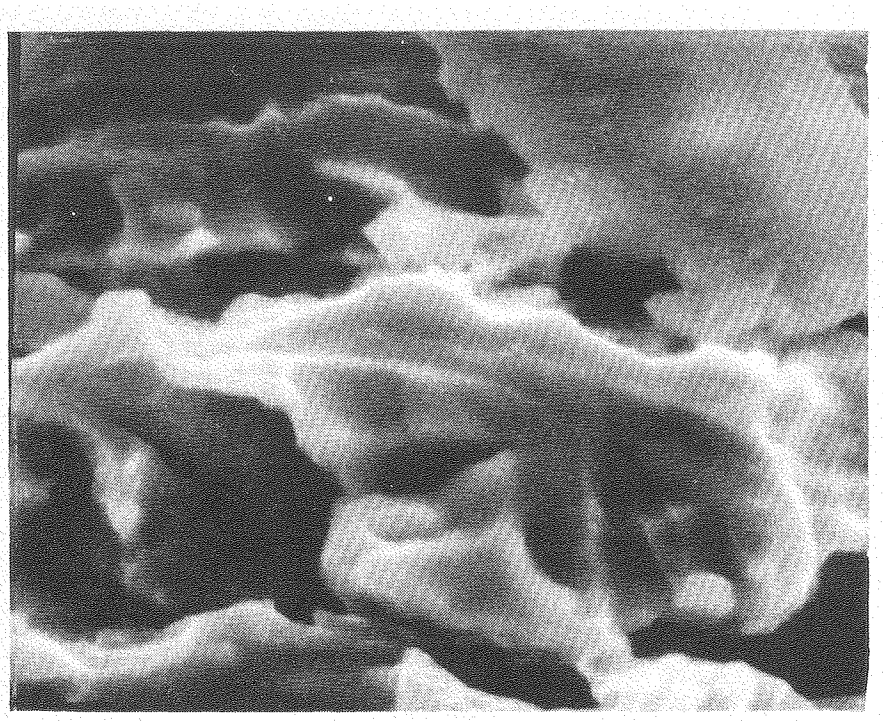

2 μ

XBB 791-313A

Figure 14. Cleaved grain of Fig. 13 at higher magnification.

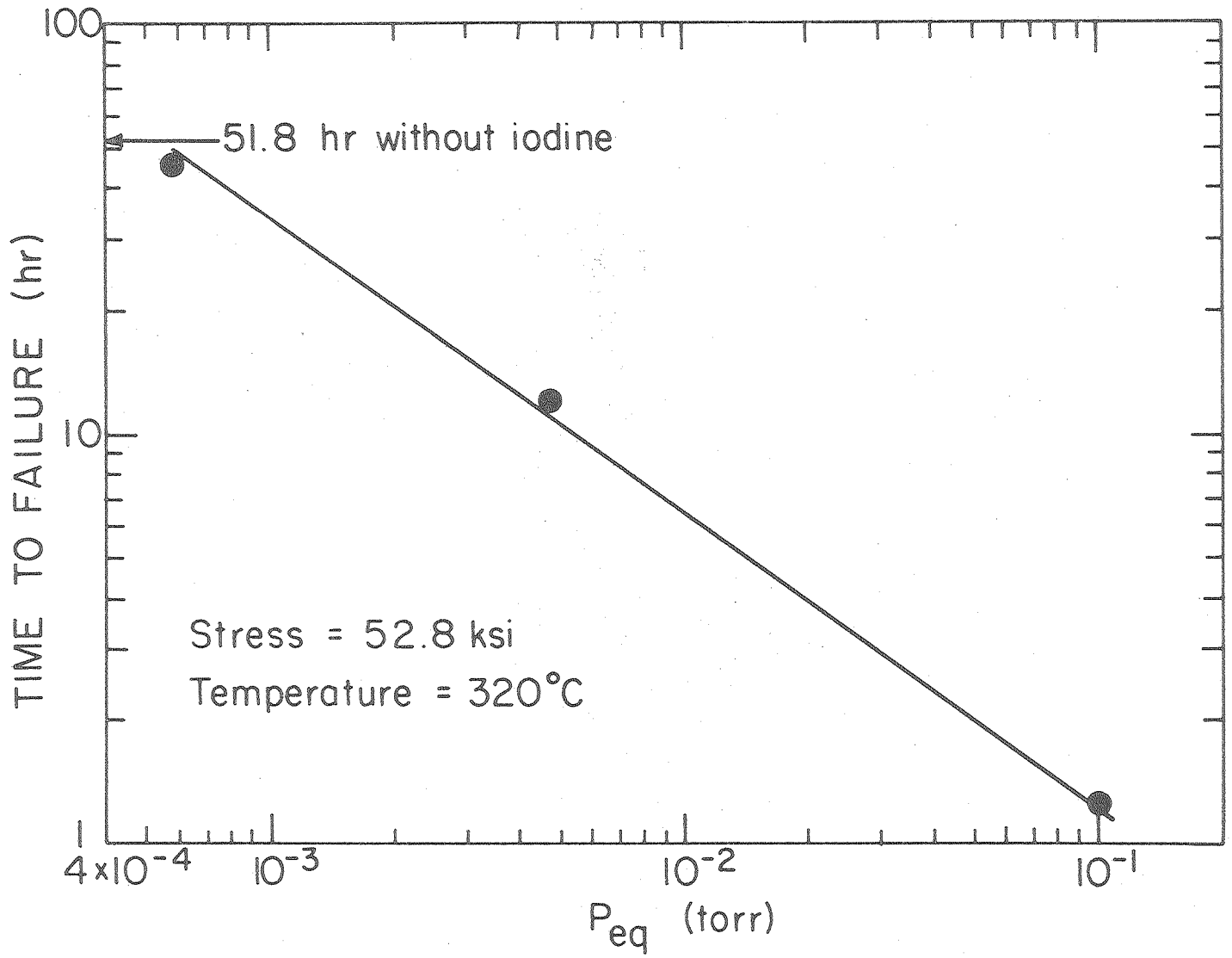

XBL 792-5665

Figure 15. Time to failure vs. iodine pressure relation for unflawed SRI specimens.

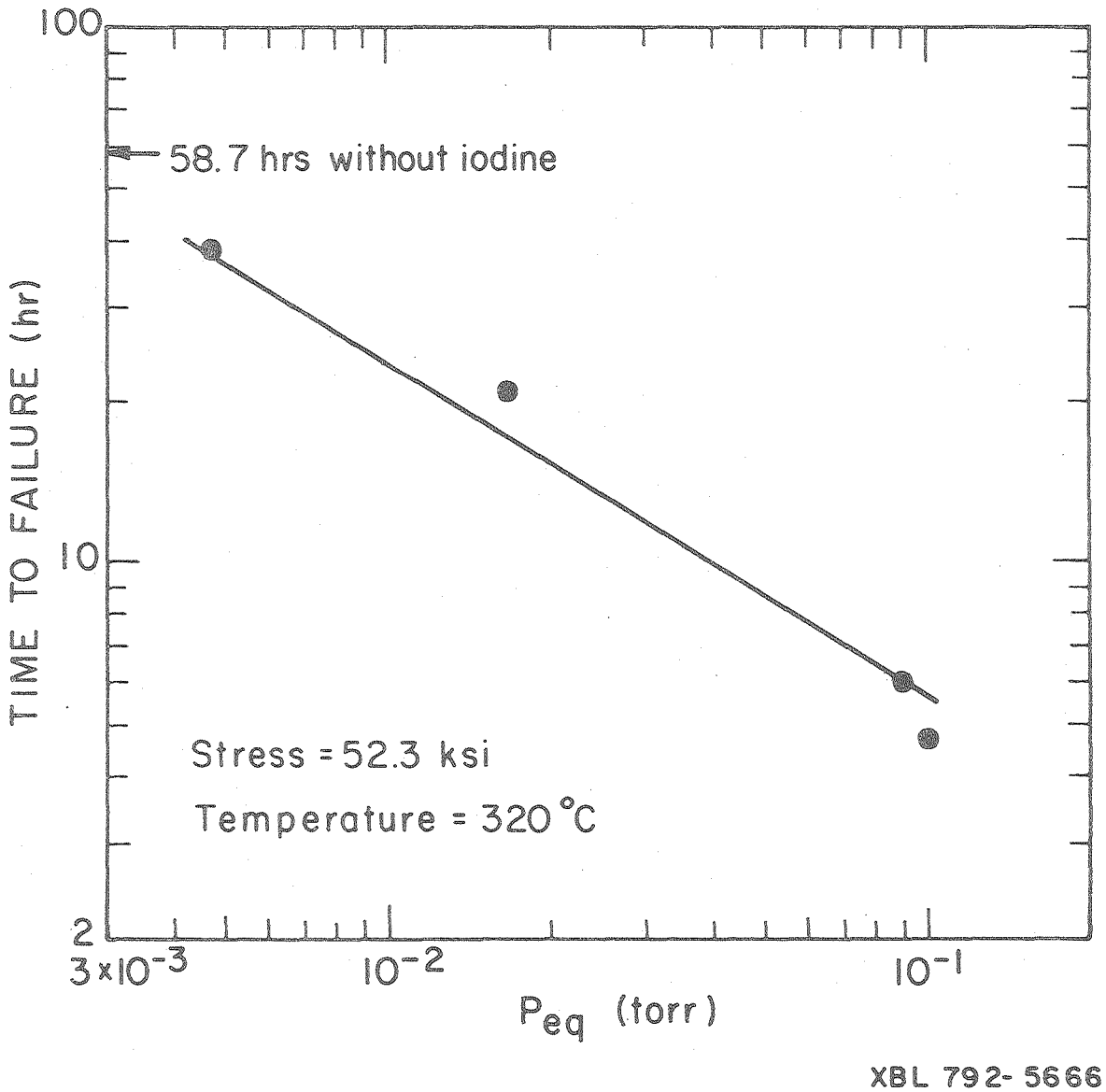

Figure 16. Time to failure vs. iodine pressure for preflawed SRI specimens.

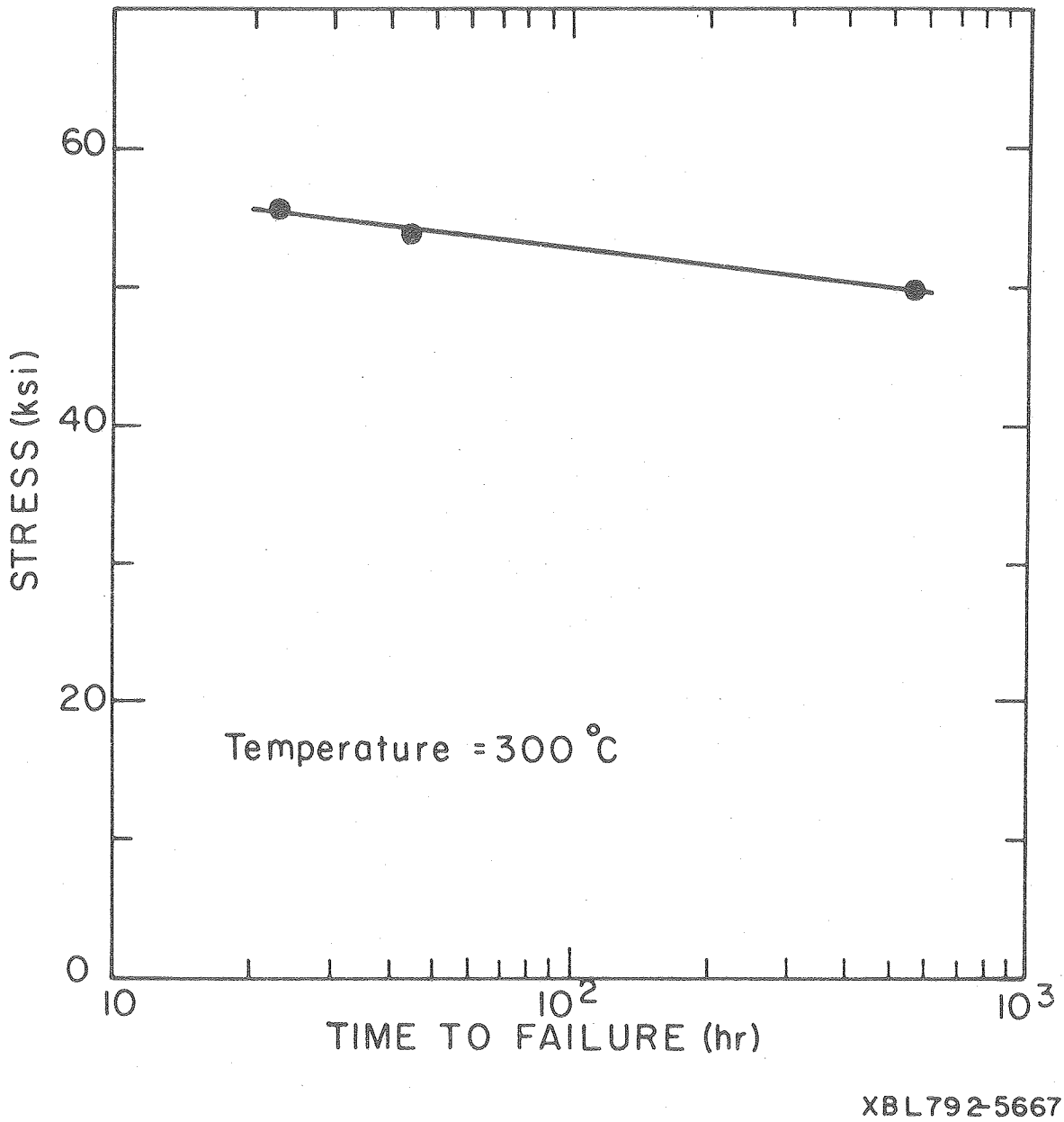

Figure 17. Time to failure vs. stress for control specimens (Sandvik) at 300°C without iodine.

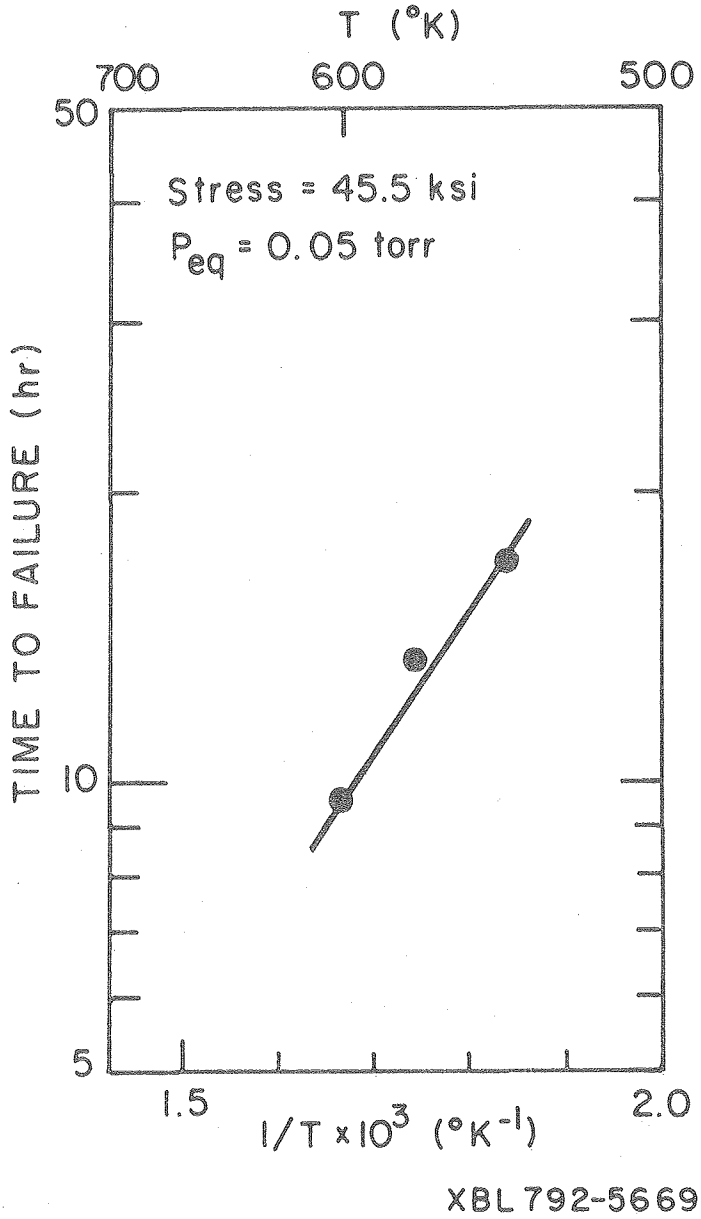

Figure 18. Time to failure vs. temperature for Sandvik specimens at 45.5 Ksi and 0.05 torr iodine pressure.

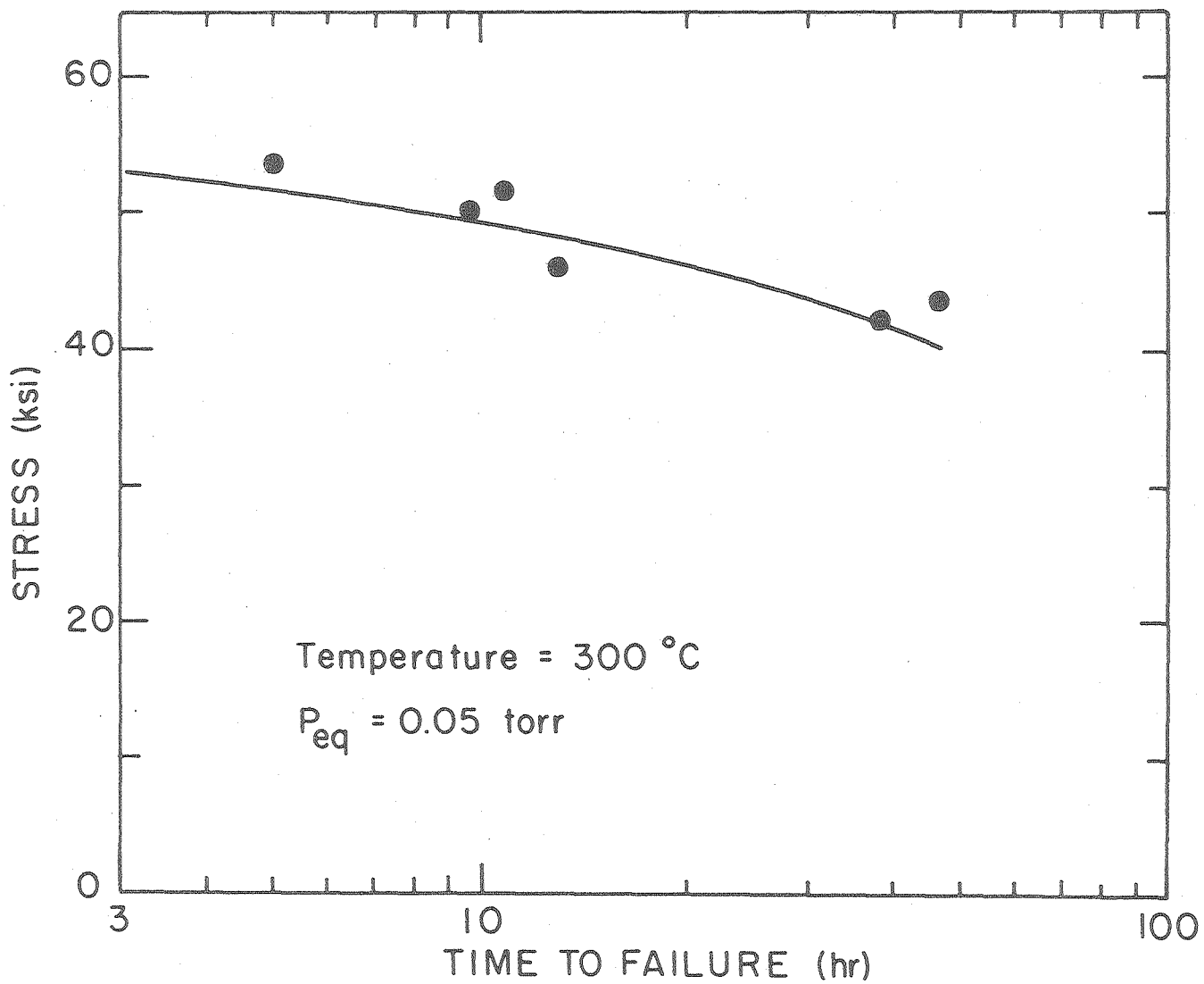

XBL792-5663

Figure 19. Time to failure vs. stress for Sandvik specimens at 300°C and 0.05 torr iodine pressure.

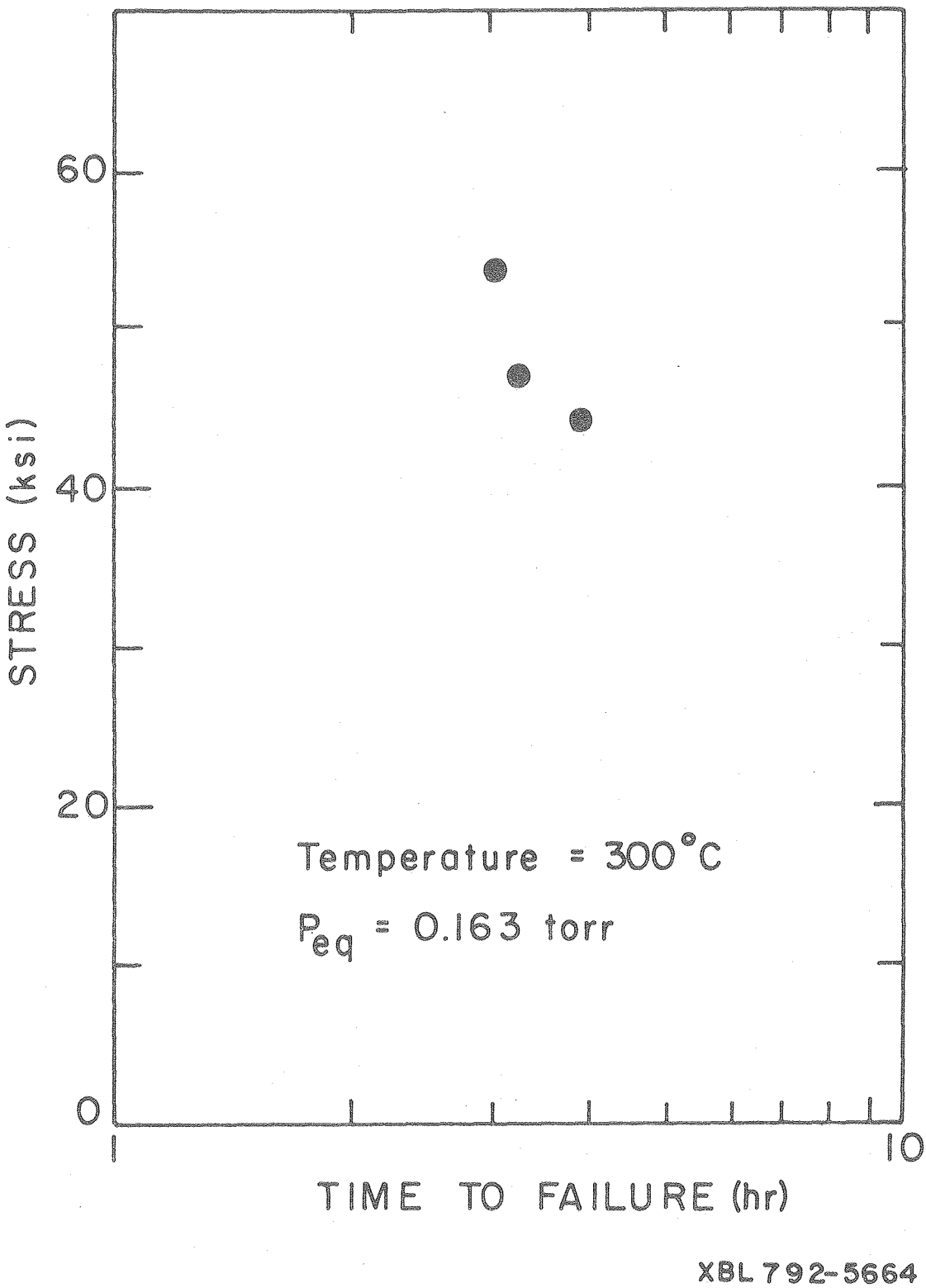

Figure 20. Time to failure vs. stress for Sandvik specimens at 300°C and 0.163 torr iodine pressure.

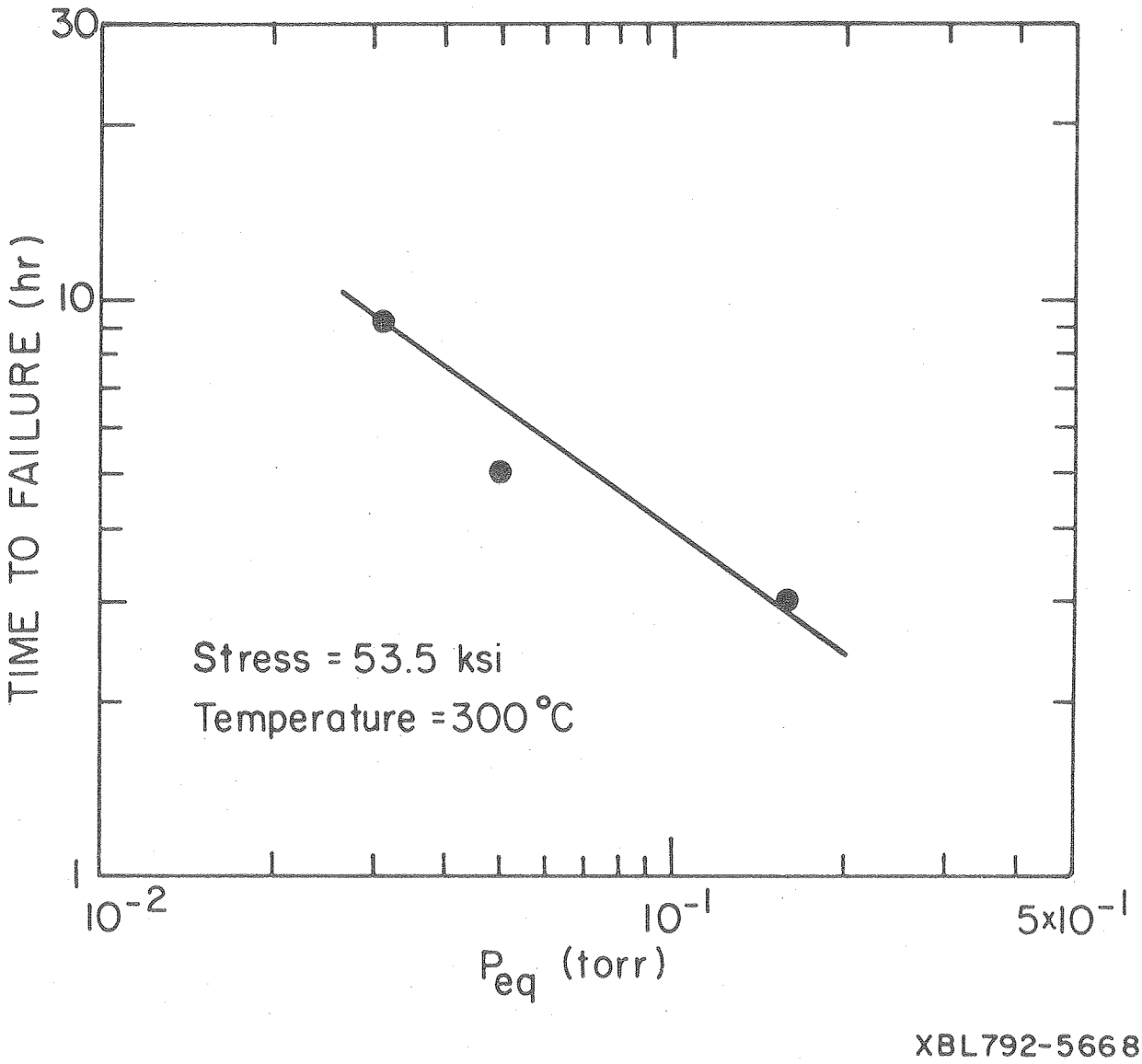

Figure 21. Time to failure vs. iodine pressure for Sandvik specimens at 53.5 Ksi and 300°C (t_F = 44.3 hrs for specimen without iodine).

Reduction of UO_2 and Measurement of the Oxygen-Metal Ratio

by: Kee Kim

I. Introduction

Oxygen self-diffusion in hypostoichiometric uranium oxides is of importance in predicting the rate of oxygen redistribution and other physicochemical processes occuring in an irradiated fuel pin. Although there have been many measurements of oxygen diffusion in ordinary oxides and in hyperstoichiometric uranium dioxide (UO_{2+x}) (1), similar measurements in UO_{2-x} have been proven very difficult mainly because UO_{2-x} is a defect structure stable only at $T > 1300^{\circ}C$, and its oxygen diffusivity is likely to be large enough to render convertional methods unworkable (i.e., gas phase mass transfer of surface isotope exchange are rate limiting). The method proposed involves a diffusion couple consisting of UO_{2-x}^{18} wafer sandwiched to a UO_{2-x}^{16} water by a bond of liquid uranium. When heated, the O^{18} and O^{16} will interdiffuse. The liquid uranium at the interface is intended to eliminate a gap resistance to oxygen transfer in a manner similar to a sodium bond in carbide LMFBR fuel pin. The hypostoichiometric samples are to be prepared by hydrogen reduction of UO_2 at high temperature:

$$UO_2 + xH_2 = UO_{2-x} + xH_2O$$

The course of the reduction process will be followed by an electromicro-balance which continuously monitors the weight of sample. Before each diffusion test the stoichiometry of the sample should be determined.

II. Theory of the O/U Determination

Since there is a substantial amount of evaporation at high temperature the stoichiometry can not be measured directly by the total weight change during the reduction step. This problem can be overcome simply by having another piece of urania present during the reduction step and subsequently oxidizing this test specimen back to UO_2 at lower temperature while measuring the weight gain from which the stoichiometry can be calculated by:

$$O/U = 2.0 - \frac{270}{16} \frac{dw}{w} \qquad (1)$$

where dw = weight gain and w = specimen weight. The oxidation of UO_{2-x} can be achieved by flowing gas which has the equilibrium oxygen potential of stoichiometric UO_2. The equilibrium oxygen potential of $UO_{2\pm x}$, $\overline{\Delta G}_{02}$, is well known as a function of temperature and stoichiometry and is shown in Fig. 1 (2,3). As can be seen in fig. 1, the oxygen potential changes sharply in the vicinity of stoichiometric UO_2. By using known ratios of H_2O and H_2 and controlling the temperature, the desired oxygen potential can be obtained as follows:

$$H_2 + \frac{1}{2} O_2 \leftrightharpoons H_2O(g)$$

If $\Delta G^o_{H_2O}$ is the standard free energy of formation of H_2O (g), have:

$$k = \frac{P_{H_2O}}{P_{H_2} P_{O_2}{}^{1/2}} = \exp\left[-\Delta G^0_{H_2O} / RT\right]$$

For gas-solid equilibrium the oxygen potential of the fuel must be equal to that of the H_2/H_2O gas mixture or:

$$\overline{\Delta G}_{O_2} = RT \ln P_{O_2} = 2RT\ln\frac{P_{H_2O}}{P_{H_2}} + 2\,\Delta G^0_{H_2O} \qquad (2)$$

Using this relationship, the ordinate of the Fig. 1 can be converted to the H_2O/H_2 ratio, as is shown in Fig. 2. According to this graph, at 1550 C stoichiometric UO_2 is obtained in hydrogen-water mixtures ranging from $H_2O/H_2 = 10^{-7}$ to $H_2O/H_2 = 10^{-1}$. The desired H_2O/H_2 ratio is obtained by bubbling hydrogen through water and by controlling the temperature of water. The hydrogen does not have to be saturated by water because of the extremely wide range of oxygen potential of UO_2. In this experiment the water was kept at 7°C, which gives H_2O/H_2 ratio of 10^{-2} or less.

III. Experimental

Fig. 3 shows the setup of the furance. The samples are suspended from the electromicrobalance by a rhenium wire. The gas is fed into the bottom of the molybdenum crucible and flows upward. The crucible is heated by a tungsten mesh heating element from the outside. The temperature is measured by a tungsten-rhenium thermocouple located inside the crucible. The UO_2 wafers are 0.5-1 mm thick and 1.2 cm diameter. Fig. 4 is a flow diagram of the system. Hydrogen is purified by charcoal filled liquid nitrogen trap. Gas is exhausted into the air through diffusion pump oil to prevent back diffusion of air into the crucible. Samples are reduced in pure hydrogen at a flow rate of 20cc/sec at 1950°C and 15cc/sec at 1850°C. Before oxidizing the reduced samples, its weight is measured by Mettler microbalance. Then it is placed in a rhenium basket suspended from the electromicrobalance by a rhenium wire. The reduced samples are oxidized to UO_2 using hydrogen stream of $H_2O/H_2 \leq 10^{-2}$ at temperature range of 1200-1400°C. The experimental procedures is:

1. Pump out the whole system and degas the sample at 200°C.
2. Cool down to room temperature and fill the system with helium.
3. Heat the sample to 800°C and record the electromicrobalance weight of the sample in this condition.
4. Flow hydrogen at 10 cc/sec. (Valves 1 and 2 in fig 4 closed; valves 3 and 4 open).
5. In flowing H_2, heat the sample up to 1300°C.
6. Flow H_2O/H_2 the mixture by opening valves 1 and 2 and closing valves 3 and 4 until the weight reaches steady state.
7. Flow dry hydrogen.
8. Cool down to 800°C.
9. Flush the system with helium and record the electromicrobalance weight.
10. Cool down to room temperature.

11. Take out the sample and measure the final weight using the Mettler balance.

The weight measurements of step 3 and 9 give the weight increases. The measurement of the initial and final weights by the Mettler microbalance also gives the weight increasment to be compared with the value obtained by electromicrobalance in septs 3 and 9. In order to make sure that the rhenium wire and basket do not react with H_2O-H_2 in the operating condition, a dummy test was done without any sample in the basket. This test showed no weight changes through 1500°C, so that all the weight increase is attributed to oxidation of the sample.

IV. Results

Reducing Conditions			Oxidizing back to $UO_{2.0}$			
Temp, °C	H_2(std) cc/sec flow rate	time, hrs	w_i (g)	dw_1 (mg)	dw_2 (mg)	O/U
1850°C	20	1	0.6039	--	0.99	1.972
1850°C	10	1	0.5728	--	1.00	1.970
1850°C	20	2	0.5702	--	1.57	1.954
1950°C	20	2	1.1532	2.651	2.65	1.951
1950°C	20	4	1.1886	--	3.20	1.955
1950°C	20	4	1.2080	3.298	3.30	1.954

w_i = weight of the reduced sample before oxidation

dw_1 = weight gain measured by Mettler balance

dw_2 = weight gain measured by electrobalance

O/U = calculated stoichiometry of the reduced sample.

For example, the first row is for a sample which was reduced for 1 hr at 1850°C and H_2 flow rate of 20 cc/sec. The reduced sample weight is 0.6039 g, which increased by 0.99 mg when oxidized to UO_2. The stoichiometry was calculated from Eq (1) to be 1.972. Precision of O/U values is $\pm$ 0.007. As can be seen the reduction rates rapidly slow down with time (i.e. for the 4 hr run, more than half of the reduction was achieved in the first 1 hr.)

Future Experiments

In order to make the UO_{2-x}^{18} wafer which is part of the diffusion couple, O^{16} in a UO_2^{16} wafer will be substituted by O^{18} using H_2O^{18}-H_2 mixtures using the same method is employed in oxidation of UO_{2-x} (i.e. flow H_2 thru H_2O^{18} and expose UO_{2-x}^{16} to this stream at 1200°C - 1500°C). One wafer of UO_2^{16} and one of UO_2^{18} will be reduced to UO_{2-x}^{16} and UO_{2-x}^{16} respectively, and the diffusion couple will be fabricated.

References

1. J.F. Marin and P. Contamin, J. Nucl. Mater. 30, 16 (1969)

2. N.A. Javed, J. Nucl. Mater. 43, 219 (1972)

3. P.E. Blackburn, J. Nucl. Mater. 46, 244 (1973)

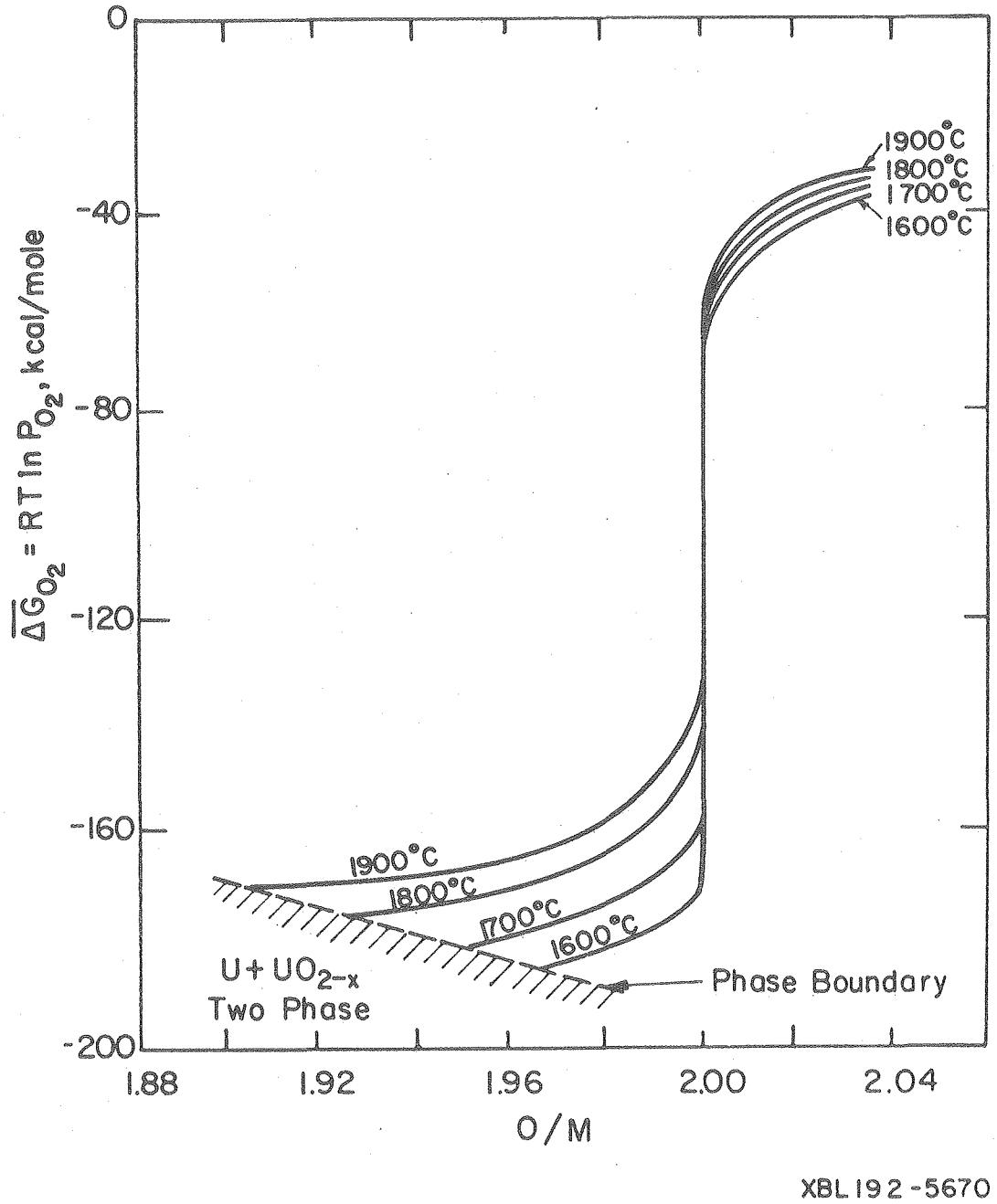

Figure 1. Variation of oxygen potential with temperature and o/M ratio.

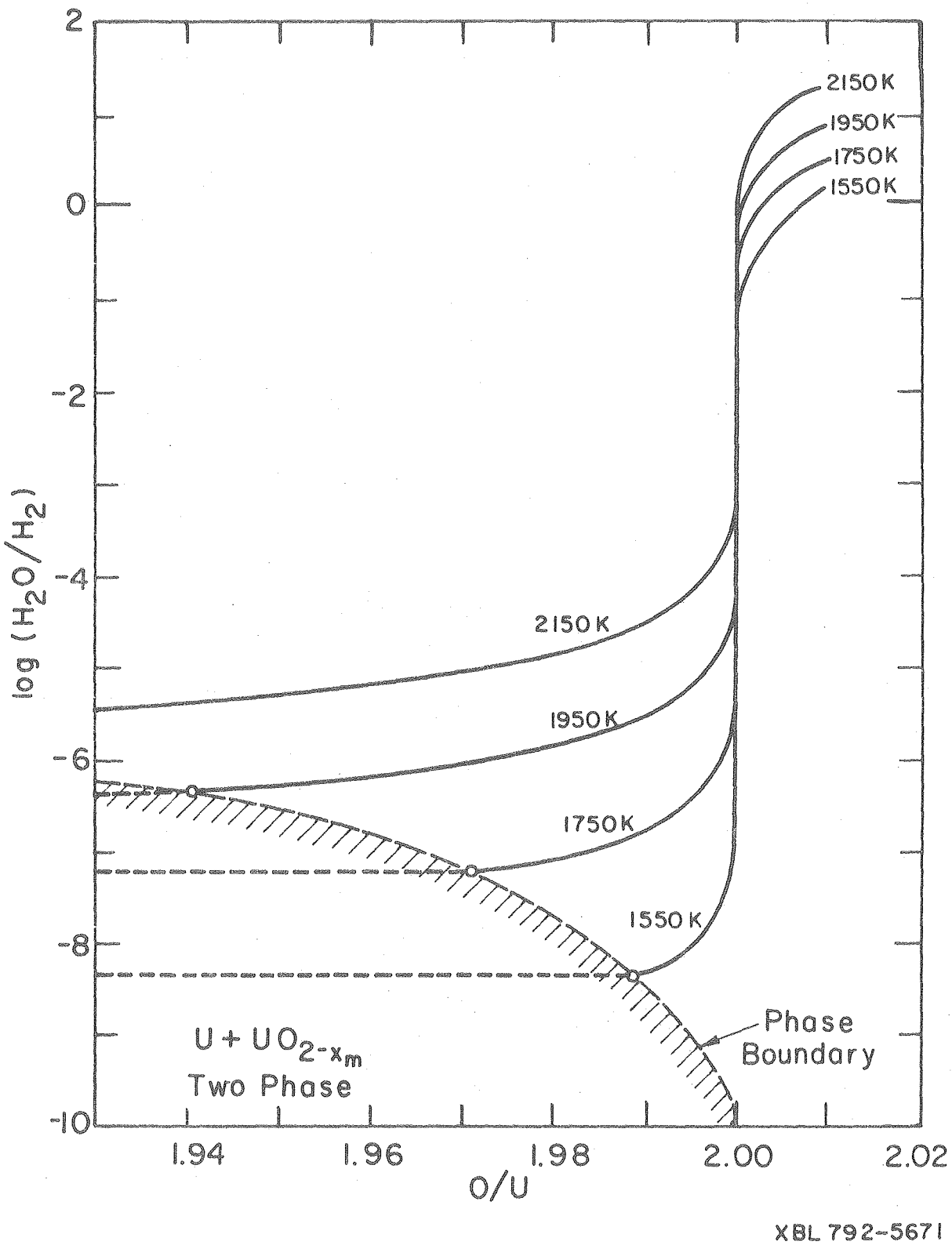

Figure 2. H_2O/H_2 ratios.

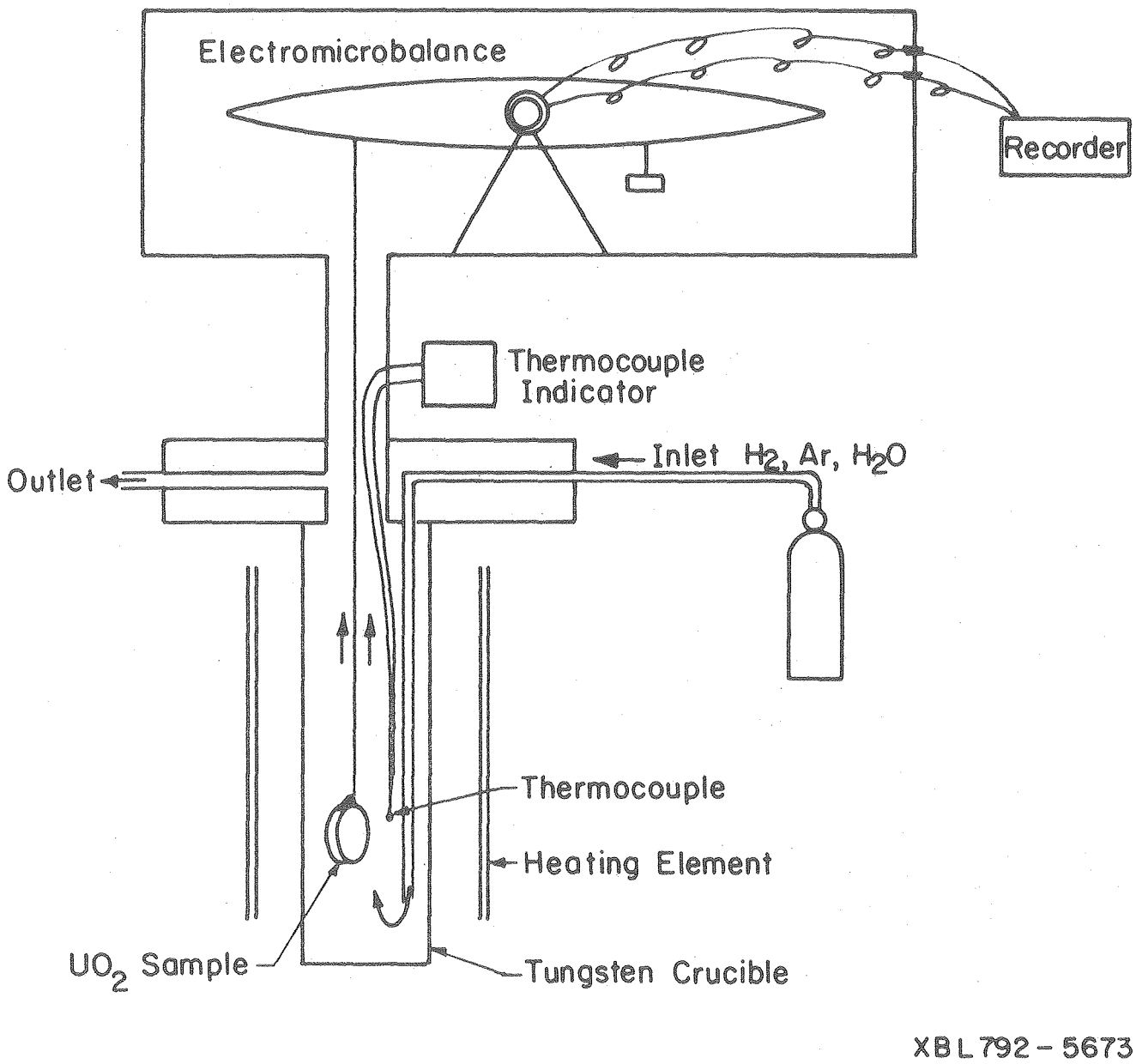

Figure 3. Apparatus for reduction/oxidation of UO_2.

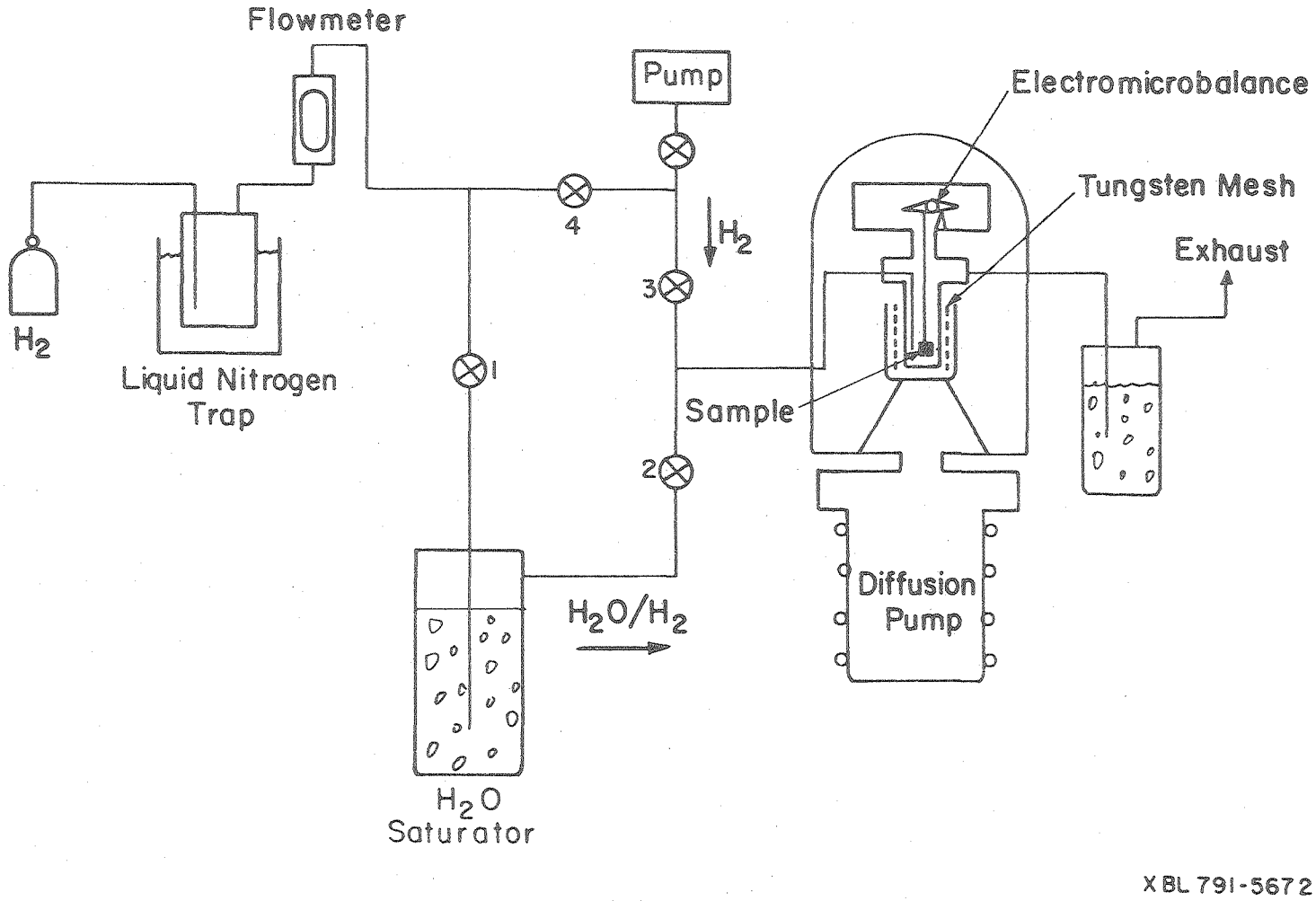

Figure 4. Diagram of gas handling system.

The Surface Chemistry of Epitaxial Silicon Deposition by Thermal Cracking

By M. Farnaam

I. Introduction

Thermal cracking of silane by the reaction $SiH_4(g) \rightarrow Si + 2H_2(g)$ is widely used for production of epitaxial layers of silicon on a substrate. This technique is extensively used in the semiconductor industry and in the Fabrication of Photovoltaic devices for direct solar energy conversion to electricity. Until a couple of years ago, atmospheric pressure reaction was the standard chemical vapor deposition (CVD) growth process. However, the low pressure chemical vapor deposition (LPCVD) reaction (0.5 torr .640°C) was found to give lower costs, higher productivity, and better uniformity compared to the atmospheric pressure method(1). Apparently higher vacuum levels and lower pressures result in a better control of the deposition process, thus encouraging investigators to decrease the pressures and even turn to molecular beam techniques.

Deposition of the epitaxial layers of silicon takes place by the incorporation of silicon adatoms into the growing epitaxial layers, and whether these adatoms are produced from a CVD process or by condensation of silicon vapor or by any other process does not affect the growth process, which is driven by the superstauration of the surface with silicon adatoms. In a CVD process, the adatoms are produced by decomposition of the molecules of the silicon bearing gas on the surface.

Application of the conventional techniques for investigation of the silane-cracking reaction (i.e., measurement of the rate of the steady state production of H_2 by heterogeneous reactions) have resulted in contradictory

mechanistic interpretation for this process (2,3,4). In order to permit more detailed probing of the surface processes than can be achieved by steady state kinetic studies, our experiment utilizes a modulated molecular beam method which has advantages such as phase lag measurements (5).

II. Experimental

A. Specimen Preparation

In order to solve the problem of island growth on the crystal surface which was encountered at the high temperatures required for the silane beam-crystal chemical interaction, new techniques and materials were tried. A new type of crystal prepared by the Topsil corporation using methods which are claimed to give much lower impurity concentration than the czochralski method, was utilized. The crystals were undoped in order to avoid possible interference of the dopant in the surface structure during the experiment. The crystals were in the form of disks 5.0 cm in diameter and 0.25 cm thick with a (111) surface orientation. They were cut by diamond saw into slabs 2.8 cm x 0.6 cm x 0.25 cm in size.

Surface preparation started with polishing with 6 μm diamond paste, cleaning in acetone, methyl ethyl ketone and ethanol, dipping in hydrofluoric acid, rinsing in deionized water, blow drying with N_2 gas, and finally heating resistively at 1150°C in vacuum for about 30 minutes. Scanning electron micrographs of this crystal showed a very rough surface containing irregular islands and pits displaying the trace of scratches made on the crystal during polishing.

Subsequent specimens were polished, cleaned and heated more carefully according to the following treatment:

The crystal was embedded in the top face of a disk of cold mount material about 0.5 cm thick and polished by hand along at 45° to the longitudinal direction of the crystal in order to prevent cracking. (0) grade emery paper was used in this step which was continued until the whole surface of

the crystal was covered only with scratches along the 45° polishing direction. Then, using a new (0) grade emergy paper, the crystal was polished along the direction perpendicular to the initial direction until the whole surface was covered with scratches in this new direction. After cleaning the crystal ultrasonically, it was polished successively with (00), (000), and (0000) grade emery paper in a similar manner. The polishing was continued using 6 μm and 1 μm diamond paste on the automatic rotary wheel. The last step of polishing was done using vibratory plates covered with microcloth polishing pad and containing 0.05 μm γ-Alumina powder dispensed in distilled water. Ultrasonic cleaning was always used between polishing steps. The crystal was removed from the embedding material by heating with hot air, which causes swelling of the material and releases the crystal without damage.

The crystal was cleaned ultrasonically and then degreased in the solution of phosphoric acid (3 parts) H_2O_2 (2 parts). At this stage, the 13-step cleaning method[6] was used for cleaning the crystal.

B. Specimen Heating

As before, an optical pyrometer was used for measuring the temperatures, but a heating filament was installed below the ceramic crystal holder. This filament can be heated independently of the crystal and serves two purposes. First, it is used during baking of the system to bake out the whole assembly holding the crystal (ceramic, tantalum clips, wiring, etc...) and the part of the chamber adjacent to the crystal. Secondly, pre-heating of the crystal by the filament causes the resistance of the crystal drop drastically, thereby making it much easier to heat the crystal resistively to high temperatures.

III. Results

A specimen prepared by the method described above was heated in the vacuum system to 1150°C while a molecular beam of silane impinged on the center. Fig. 1 shows the scanning electron micrographs of this crystal taken after the experiment. It is believed that (7) the triangular vaporization pits on the region of the surface not exposed to the silane beam (Fig. 1-a) results from carbon-contamination. If the surface is clean, vaporization is a 2-D process and no topographic effects occur: in other words thermal etching is the exact inverse of growth. The growth morphology in the region exposed to silane (Fig. 1-b) is also believed to be an indication of heavy carbon contamination, and at the high temperatures involved this would almost certainly be present as β-S_iC.

The crystal used in the experiment was one of the purest types available for epitaxial growth, therefore the bulk of the crystal is not responsible for the contamination. But the crystal surface itself could be the source of the contamination i.e., polishing and cleaning methods should be modified and if necessary new steps must be added.

IV. Planned Experimental Modifications

In-situ Hcℓ etching is one of the most widely used etching steps for preparing silicon specimens. Therefore a doser for Hcℓ has been installed in the vacuum system adjacent to the crystal.

The effect of another step of polishing called Electroless Silicon polish will also be investigated. This step is a chemical-mechanical polishing process which will follow polishing with 0.05 μm γ-Alumina.

Another possible solution is the use of epitaxially-grown surfaces, i.e., a film a few microns thick grown on a substrate by conventional silicon process technology. This material will simply be mounted in the vacuum system and heat cleaned for a few minutes at 1100-1200°K. which is claimed to be adequate to remove the carbon (from adsorbed atmospheric gases) to below the detection limit of several usual detection techniques[7,8].

The vacuum system may also be modified (e.g. by replacing the diffusion pump by a cryopump) to reduce contamination due to background gases.

Once pitting evaporation is eliminated and 2-D evaporation and growth is achieved, the kinetic studies of the silane cracking reaction will be continued.

References:

1. R.S. Rosler, Solid State Tech. P 63 April (1977).

2. B.A. Joyce et. al. Phil. Mag 14, 289, 301 (1966) and 1167 (1967).

3. R.C. Henderson et. al. Surf. Sci. 30, 310 (1972).

4. R.F.C. Farrow, J. Electrochem. Soc. 121 899 (1974).

5. R.H. Jones, D.R. Olander, W.J. Siekhaus, and J.A. Schwarz J. Vac. Sci. Tech. 9 1429 (1972).

6. S.P. Murarka et. al. J. Appl. Phys. 48 No. 9, (1977).

7. Private Communications with B.A. Joyce.

8. R.C. Henderson et. al. J. of Appl. Phys. 42, No. 3 (1971).

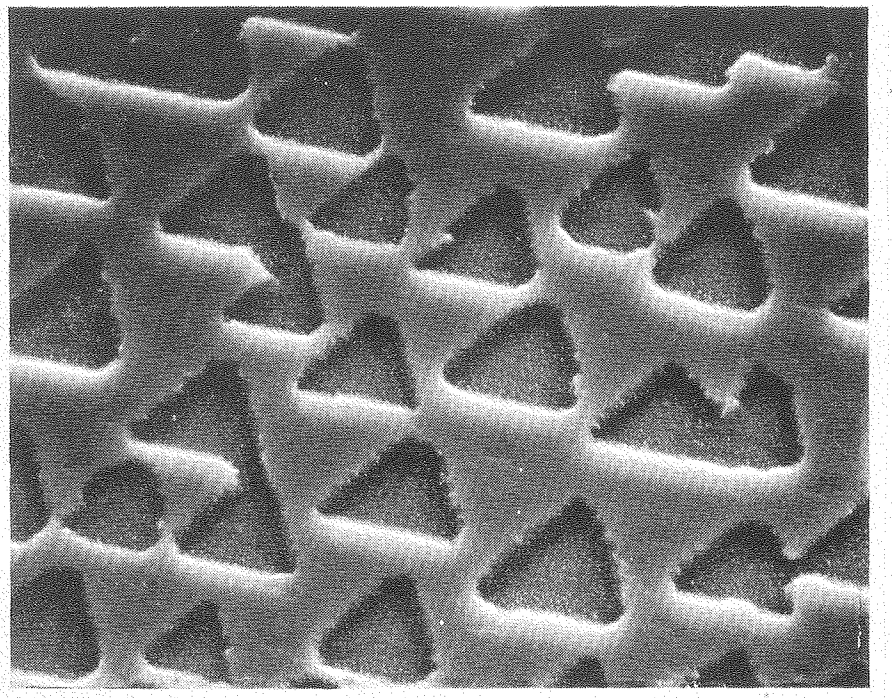

Crystal #17
Area not exposed to silane

5μm

Fig. 1-a

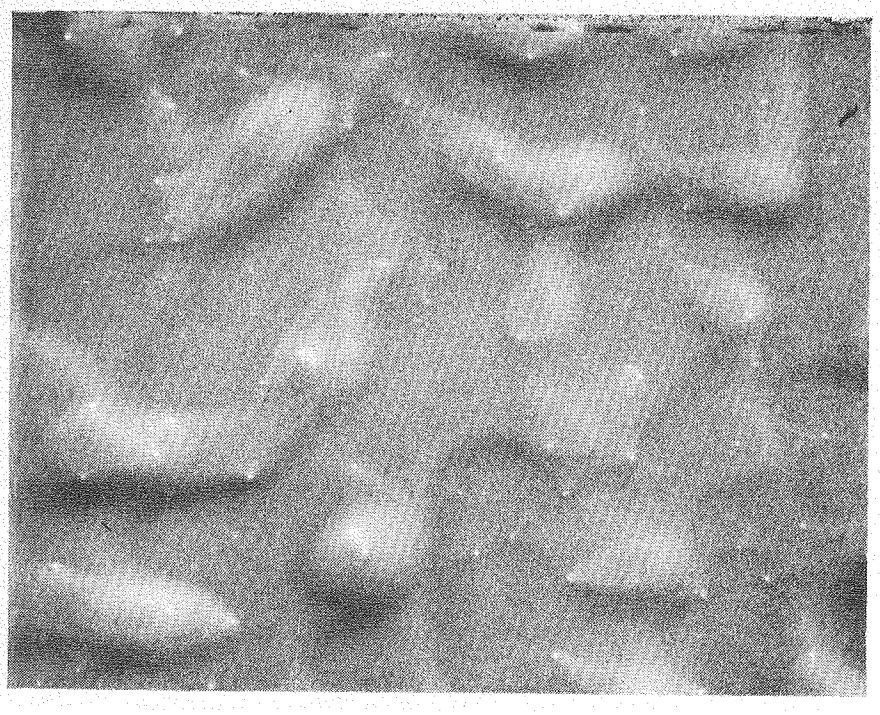

Crystal #17
Area exposed to silane

5μm

Fig. 1-b

XBB 791-731

The Kinetics of Laser Pulse Vaporization of UO_2

by C.H. Tsai

I. Introduction

The laser pulse vaporization technique has been developed recently to investigate the ultra-high temperature thermodynamic properties of UO_2.[1-3] The experimental determination of this thermodynamic information is necessary because of the great inconsistency in theoretical calculations as mentioned in the previous report.

Two techniques, namely the photographic and mass spectrometry techniques, have been conducted independently for vapor pressure interpretation. The transient optical pyrometry is used for surface temperature measurement in each of the methods. A computer code has been developed to calculate the surface temperature and surface composition of uranium oxide during the laser evaporation transient in order to compare with the experimental measurements.

The current year was devoted to the vapor phase angular distribution determination and surface temperature measurement by optical pyrometry, in which the mass spectrometry technique is ultilized. Some preliminary results of these measurements are given.

II. Experiments

A sketch of the experimental set up of laser pulsing on UO_2 is shown in Fig. 1a.

A UO_2 sample is preheated by electron-beam bombardment heater to $\sim 1400^\circ C$, the ductile-to-brittle transition temperature of UO_2[4], in order to avoid sample cracking resulting from the huge thermal gradient induced by laser heating. At this temperature, the absorption cut-off of UO_2 is also shifted to 1.3 μm wavelength (longer than the wavelength of Nd-glass laser 1.06 μm) which avoids in-depth heating by laser radiation penetration into the target.[5]

The laser beam is partially split to a MgO diffuser and absorbed by a pre-calibrated photodiode which gives the power shape as well as the power as a function of time. The laser power together with the laser beam radial intensity profile measured by knife-edge technique as mentioned in the last year report gives the laser peak maximum power density of each experimental run, which provides the input data for corresponding computer run for the temperature calculation.

A single-wavelength (0.65 μm) transient optical pyrometer is used to measure both the surface temperature of the pre-heated target and the surface temperature during laser heating. The transient optical pyrometer calibration is performed by a master manual optical pyrometer pre-calibrated by NBS and a graphite black-body cavity with the capacity of reaching $3000^\circ C$. Above this range, the absorbing glass filters are used to establish the extrapolation up to 6000 K.

Two arrays of small teflon disks and aluminum disks are placed around the target by a collector assembly mounted in z-direction to collect part of the ejected UO_2 from laser-heated spot, as shown in Fig. 1a & 1b. A stainless steel flag is controlled by a linear feedthrough in x-direction to avoid vapor deposits on the collector disks during target pre-heating and it is removed before laser shots. The teflon disks are then irradiated in the Berkeley Research Reactor to determine the angular distribution of vaporized UO_2 by counting the fission product radioactivity and to provide an independent

estimate of the total amount of UO_2 vaporized. Calibrated standards consisting of known amount of uranium from uranyl nitrate solution deposited on teflon disks are used to determine the absolute magnitude of the quantity of uranium deposited on the disks by the laser evaporation process. The aluminum disks are examined microscopically to determine whether the ejected material consists entirely of vapor species or emission of liquid droplets occurs.

III. Results

A. Laser Light Absorption by the Vapor Plume

The degree of thermal ionization in the vapor cloud above the surface has been estimated to be 2.7% at 4400 K.[8] The partially ionized vapor plume does not satisfy the double inequality characterizing an ordinary kinetic plasma[8], so the optical absorption is dominated by Bremsstrahlung absorption. According to the Bremsstrahlung absorption theory[9] assuming all the ions are singly charged, the absorption coefficient is 0.0466 cm^{-1} for 1.06 μm Nd-glass laser and 0.0107 cm^{-1} for 0.65 μm optical pyrometer. Assuming an absorbing layer of 0.5mm[10], the absorption of 1.06 μm laser light is 0.2% and that of 0.65 μm optical pyrometer is 0.15%. It is obvious that the optical absorption is negligible in this temperature range.

B. Temperature Measurement

The maximum surface temperature measured by the transient optical pyrometer is 4200 $\pm$ 60 K for the run at laser total energy of 27.85 Joules. After taking the spectral emissivity of UO_2 at this temperature at 0.65 μm ($\sim$ 0.92[11]) into account, the maximum surface temperature is about 4268 K. The result of the temperature calculation by our computer code is 4410 K and 4200 K with and without considering surface composition depletion respectively. The focal distance of the optical pyrometer is $\sim$ 53 cm, and the diameter of the focal spot corresponding to this focal distance is $\sim$ 1.33 mm. Since the optical pyrometer is sighted 45° to the target normal, the pyrometer focal spot is elliptical with a major axis of $\sim$ 1.88 mm.

According to the laser power intensity profile across radial direction on the target measured by knife-edge technique, the error of the optical pyrometer measurement corresponding to this power variation across the pyrometer focal spot is only 5 K (see Fig. 2).

In order to verify the temperature measurement, graphite and tungsten are being studied to compare the experimental measurement and theoretical calculation by taking the advantages of well-known high temperature properties of both materials.

C. Target Characterization

The irradiated UO_2 target has been examined by scanning electron microscope. Fig. 3a shows the laser-irradiated area. Melting out to an ellipse of major radius 3.81 mm and minor radius 2.35 mm is seen in this micrograph. An apparent ring structure on the target surface is observed within the molten area. The ring structure is attributed to the radial propagation of a central disturbance on the liquid surface in the form of capillary waves.[12] The discontinuous quasi-periodic liquid displacement from the centre of the "pool" due to the recoil force of the evaporating material is believed to be the driving mechanism of this disturbance.

Figs. 3b and 3c show the UO_2 surface under higher magnification with and without melting respectively. The white dots appearing mostly along the grain boundaries in the irradiated area (Fig. 3b) probably uranium metal aggregates which are expected due to the preferential evaporation of oxygen under strong free evaporation.

D. Deposits on the Aluminum Collectors

Figs. 4a and 4b show scanning electron micrographs of the aluminum disk collectors. It is evident that there is condensed UO_2 on the disks, some with donut shape and some spherical. The radii range from 1 μm to 15 μm. Elemental analysis (EDAX) result (Fig. 4c) reveals that they contain uranium, which suggests that either (a) UO_2 liquid droplet ejection

from the melt occurs -- this is also suggested by the small craters in the central area in Fig. 3a -- or (b) liquid droplets are formed by condensation in the collision-dominant continuum layer of the vapor plume.

E. Angular Distribution

A single UO_2 target was subjected to five laser shots to measure the vapor angular distribtion by teflon disk collectors. The amount of UO_2 collected on each teflon disk ranges from 15 μg to 60 μg, which corresponds to about 120 Å to 480 Å thickness of UO_2 layer if uniformly deposited. Taking into account the geometry of the collectors, the total amount of UO_2 evaporated is estimated approximately 2.2 mg, compared to the theoretical calculation of about 7.9 mg assuming Langmuir evaporation.

The angular distribution of mass flux from UO_2 vaporization is shown in Fig. 5. This plot shows that the angular distribution corresponds quite well with the $\cos^2\theta$ distribution. It has been found[6] that the angular variation of the supersonic free jets from sonic orifices obey a $\cos^2\theta$ relationship. This measurement reveals that the flow is not an equilibrium Maxwellian distribution; the vapor flow from strong free evaporation into vaccum can be simulated by a supersonic free-jet from a sonic orifice which is consistent with the conclusion of dynamic sampling method by mass spectrometry.[7]

References

1. R.W. Ohse, P.G. Barrie, H.G. Bogensberger and E.A. Fischer, IAEA Symp. on Thermodynamics of Nuclear Materials, Paper IAEA-SM-190/8, Vienna Oct. 1974.

2. A. Bober, J.U. Karow and K. Schretzmann, IAEA Symp. on Thermodynamics of Nuclear Materials, Paper IAEA-SM-190/34, Vienna Oct. 1974.

3. N. Asami, M. Nichikawa and M. Taguchi, IAEA Symp. on Thermodynamics of Nuclear Materials, Paper IAEA-SM-190/3, Vienna Oct. 1974.

4. D.R. Olander, "Fundamental Aspects of Nuclear REactor Fuel Elements", ERDA Technical Information Center, Oak Ridge, Tennessee April 1976.

5. M.J. Davies, Ph.D. Thesis, Dept. of Inorganic and Structural Chemistry, University of Leeds, Jan. 1970.

6. H. Ashkanas and F.S. Sherman, Rarefied Gas Dynamics - 4th Symposium, Vol. II, pp. 84-105, 1966.

7. K.A. Lincoln and M.A. Covington, Int. J. of Mass Spectrometry and Ion Physics, 16 (1975) 191-208.

8. H.U. Karow, KFK-2390, Feb. 1977.

9. Ya.B. Zel'dovich and Yu.P. Raizer, "Physics of Schock Waves and High-Temperature Hydrodynamic Phenomena", Vol. I, Academic Press, New York and London 1966.

10. R.W. Ohse and P.G. Berrie, J. Nucl. Mater. 59 (1976) 112-124.

11. M. Bober and H.U. Karow, 7th Symposium on Thermophysical Properties, NBS Washington, D.C., 1977.

12. J. Magill and R.W. Ohse, J. of Nucl. Mat. 71 (1977) 191-193.

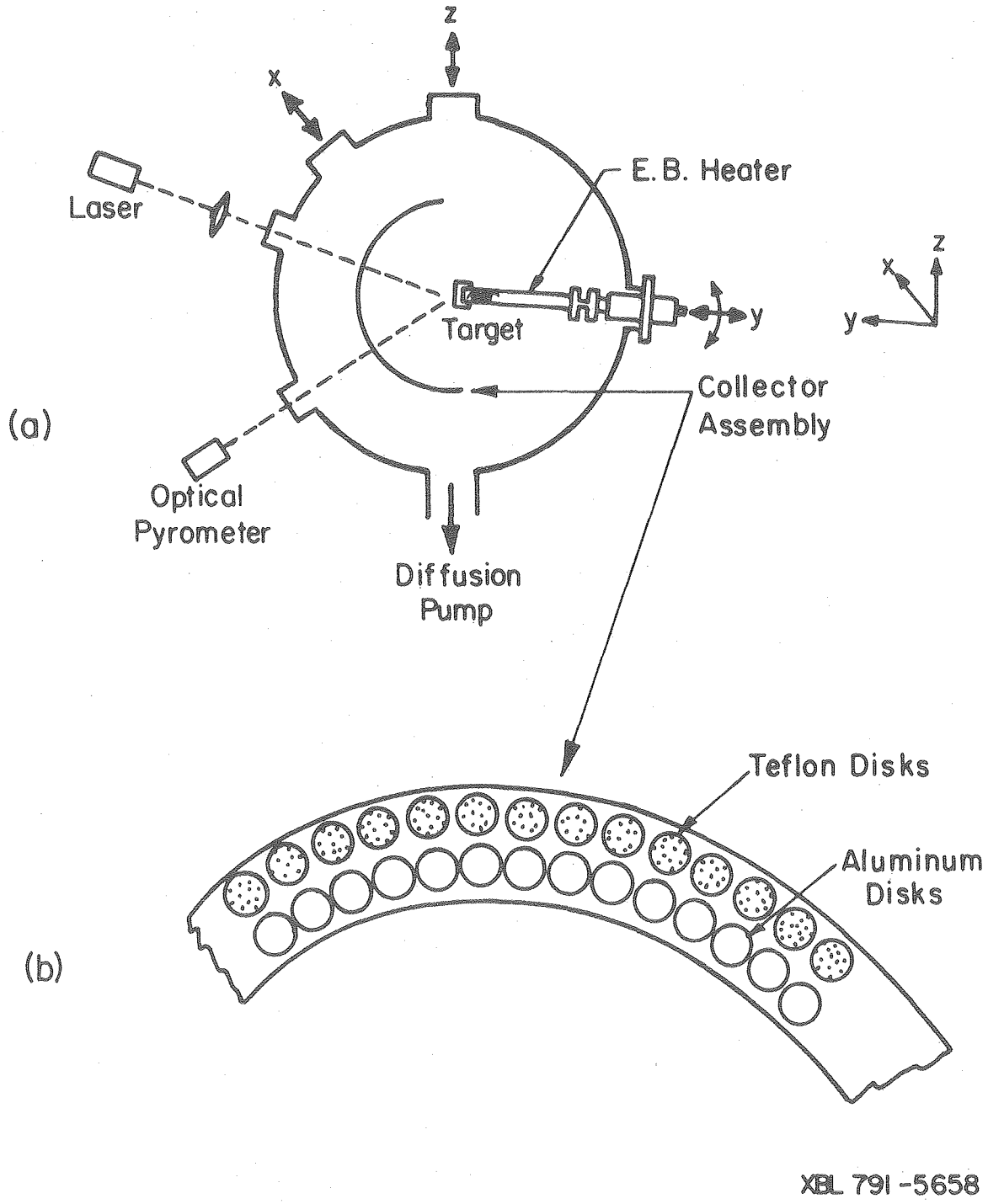

Figure 1. The collector assembly for angular distribution measurement and liquid droplet collection in LBL's apparatus.

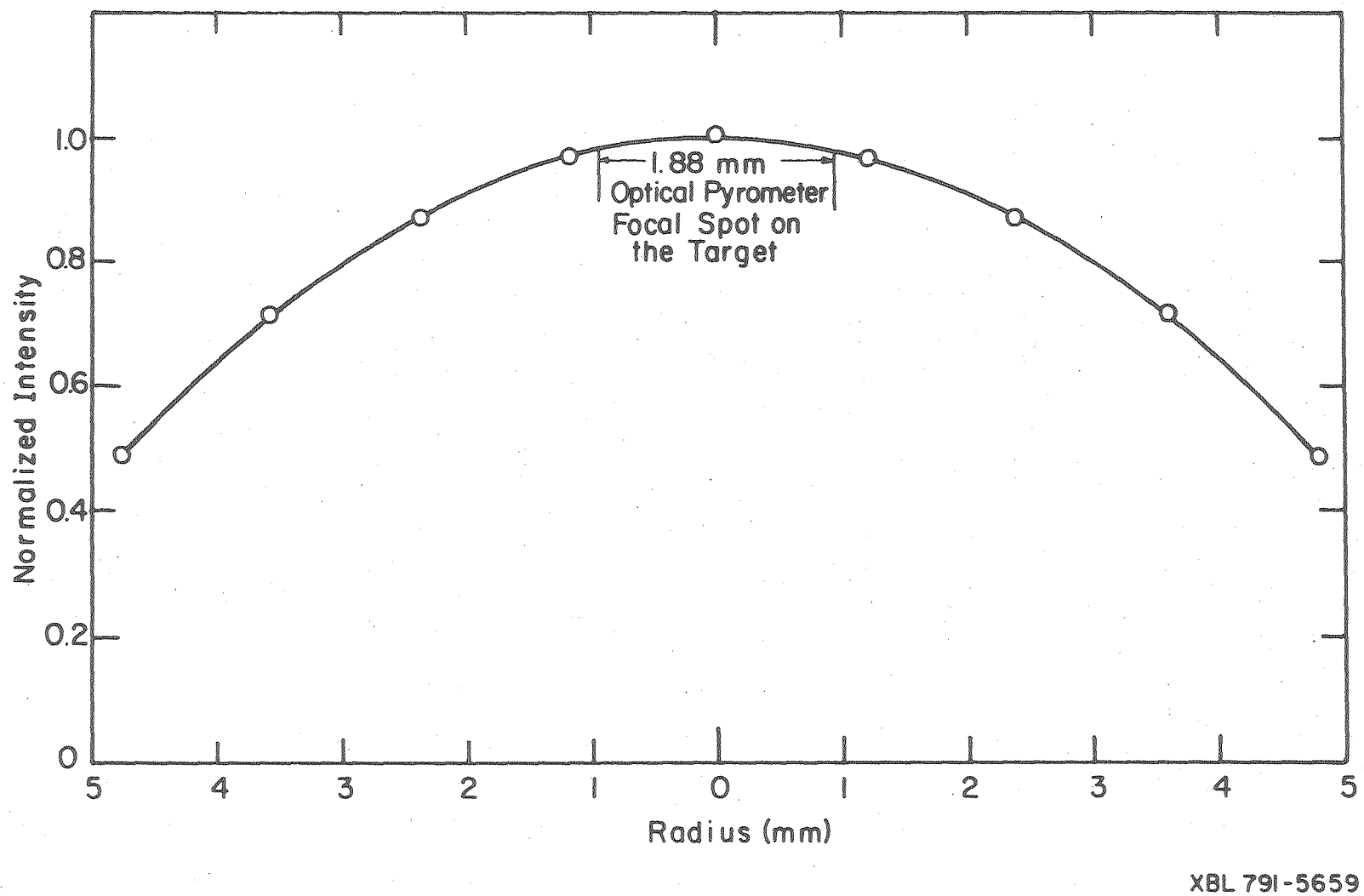

Figure 2. Normalized laser power intensity radial profile.

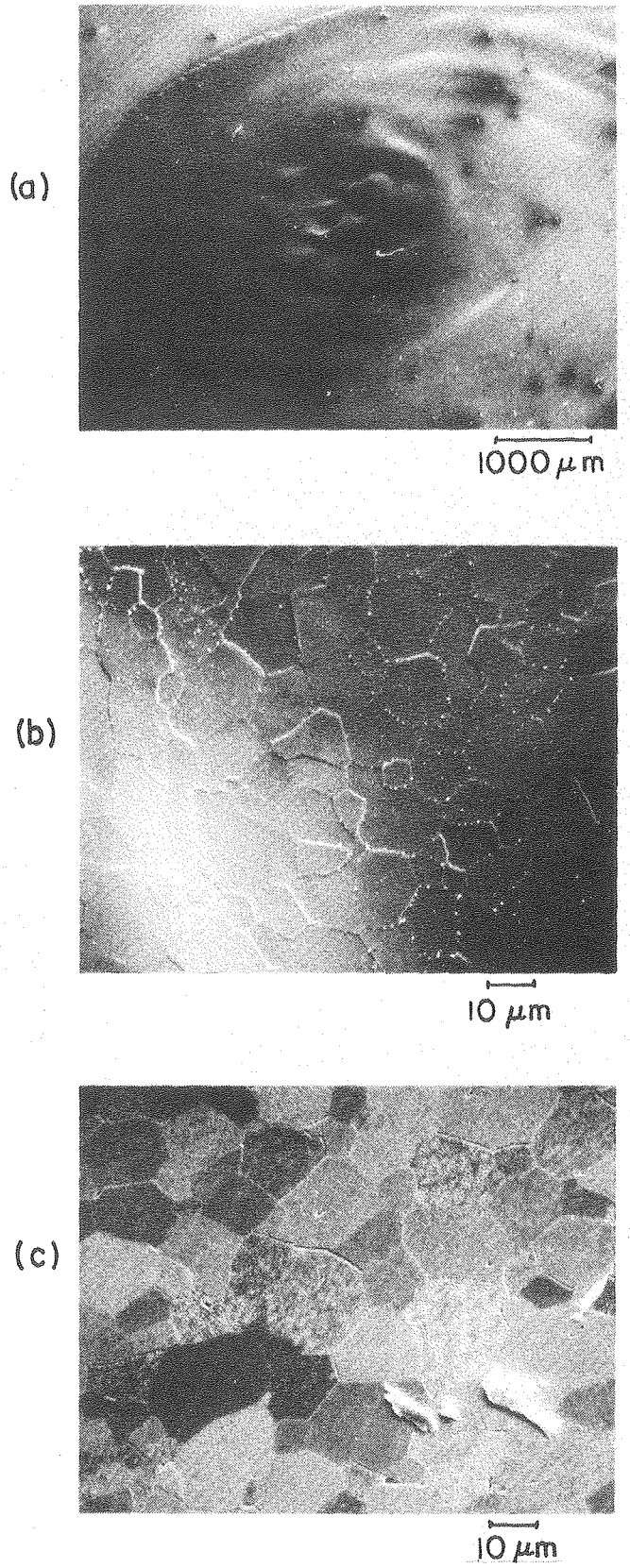

XBB 792-1258A

Figure 3. Scanning electron microphotographs of molten UO_2 surface (a) and (b), and non-molten surface (c).

(a)

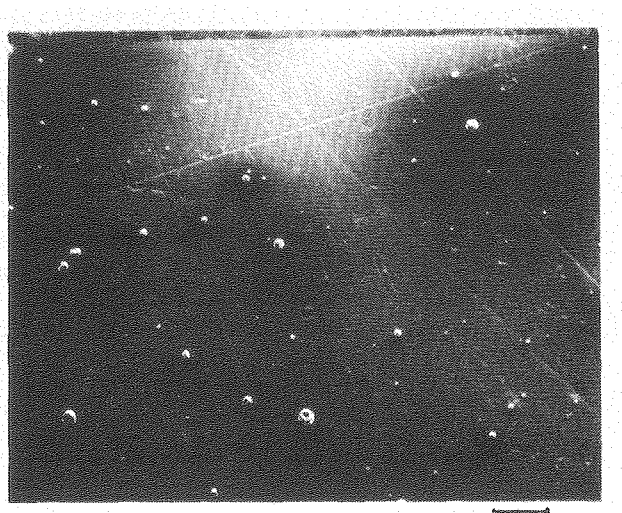

100 μm

(b)

10 μm

(c)

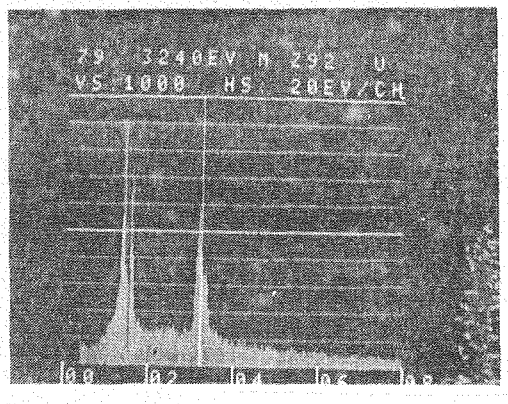

XBB 792-1257A

Figure 4. Scanning electron microphotographs of aluminum disk collector surface (a) and (b), and the EDAX analysis (c).

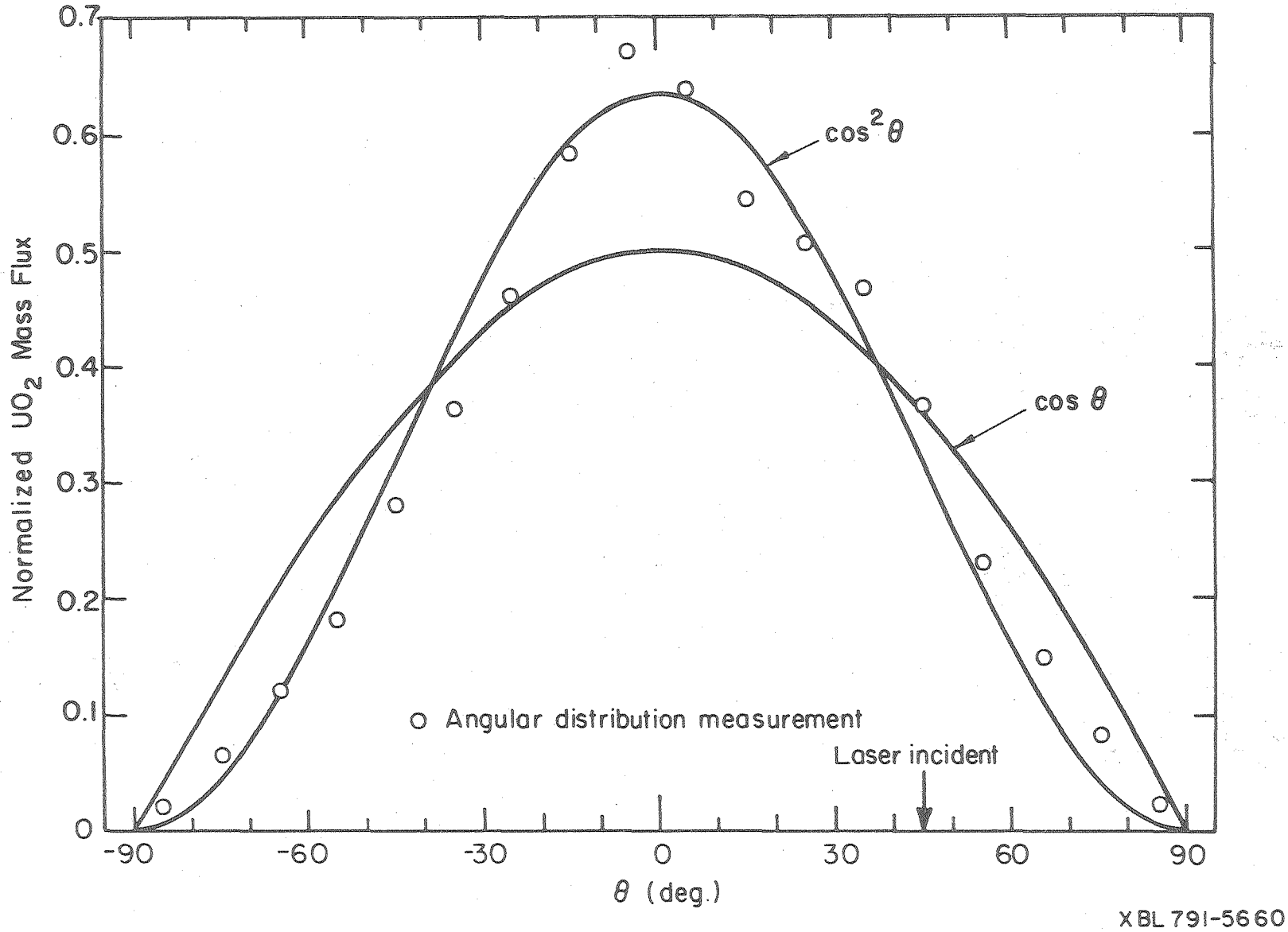

Figure 5. Angular distribution of mass flux in vapor plume from UO_2 vaporization.

RETENTION AND RELEASE OF WATER VAPOR BY URANIUM DIOXIDE

by Douglas Sherman

I. INTRODUCTION

Uranium dioxide is known to absorb water vapor from the air. When the UO_2 is subsequently heated the water is released. This water is a potential source of hydrogen which can cause hydriding of zircaloy cladding. In earlier experiments, (1-3) degassing of UO_2 which had been stored in air resulted in predominantly low-temperature release of water vapor.

In recent work in this laboratory (4) on the retention and release kinetics of water vapor by UO_2, the samples were infused with D_2O instead of H_2O in order to avoid the large H_2O background in the vacuum system. In addition, the release of D_2O during degassing was monitored *in situ* by a mass spectrometer instead of a post-release transfer of the gas to a separate chamber for analyses, as in Refs. 1-3.

The experimental technique has been described in the previous report.(4) Briefly it consists of monitoring the release of a modulated molecular beam of D_2O by a mass spectrometer (Fig. 1). The beam is produced by heating the pellets in a refractory metal crucible which is suspended in a tungsten mesh furnace. The entire crucible assembly is kept at eleveated temperatures of up to 600°C so that no D_2O can be absorbed on the inner walls. The outgassed D_2O then effuses from the exit capillary and is chopped, thus producing a modulated molecular beam. The output from the mass spectrometer which detects this molecular beam is fed into a lock-in amplifier which eliminates the d.c. component of the signal, thereby achieving a sensitivity of $\sim 10^{-12}$g D_2O/sec. The mass spectrometer is calibrated with a known flow rate of neon.

The experiment reported in Ref. 4 was conducted over the range of room

temperature to 1600°C, using a platinum crucible. A total of 12 μg D_2O/g UO_2 was reported to have been released, 95% of it at temperatures above 1000°C.

This year, an attempt was made to reproduce these results. In this duplicate experiment, similar results to those reported earlier were observed. In addition, however, it was decided to investigate to see if the mass spectrometer signal really corresponded to D_2O release. The mass spectrometer was tuned to mass 9 where no signal could be expected. On raising the voltage in the furnace, a burst in the signal was observed of similar magnitude as that of mass 20, which was supposed to be D_2O. Since no signal should have been detected at mass 9, this indicated that the high temperature "release of D_2O" that had been observed here and in the first experiment was due entirely to electronic pickup from the furnace.

To avoid electronic pickup by the mass spectrometer, an aluminum sheath which encased the mass spectrometer (except for a hole to admit the molecular beam) was installed. A blank was run and no appreciable signal was detected, even at high temperatures. A neon calibration was run to insure that the mass spectrometer could detect mass 20 singals.

II EXPERIMENTS OF JULY 1978

Three different types of UO_2 pellets of known open and closed porosity were prepared by Exxon Nuclear Co. These are designated as runs 1, 2, and 3 in Table 1.

The samples were outgassed at 250°C for 24 hours in vacuum, cooled and immersed immediately in liquid D_2O for 2-4 hours. Excess D_2O was removed by rolling in a lint-free towel, and the samples were transferred to the crucible and placed in the vacuum system. To remove any loosely bound surface D_2O the samples were evacuated at room temperature for 18 hours prior to the temp-

erature increase.

To measure the background, a blank (empty crucible) was run for the entire temperature range. During the outgassing the temperature was ramped up continuously instead of in discrete steps. In Run 1, the high open and closed porosity sample was outgassed for 5.5 hours with a linear temperature ramp of 300°C/hr. As seen in Fig. 2 the release rate had a major peak at 120°C of 480 μg/hr. This decayed to 15 μg/hr by 300°C. The background rate of approximately 0.3 μg/hr was reached at 1100 C and persisted at higher temperatures. A total of 17 μg D_2O/g UO_2 was released with 94% appearing at temperatures <300°C. The large amount of absorbed D_2O is due to the high open porosity of this sample.

Samples 2 and 3 were outgassed 6.5 and 1.8 hours at linear temperature increase rates of 250°C/hr and 900°C/hr respectively. For these two samples, which had low open porosity, the amount of D_2O released was negligible (see Fig. 3). In Run 2 the release rate was at or below background. In Run 3 the release rate was double the background level determined prior to Run 2, but because of uncertainties in calibration of the two runs, this release rate is probably at background as well. For both samples there was no observed release of D_2O at high temperature. From these experiments, it appears that water adsorbed on sintered pellets is only loosely bound. A porous sample (no. 1), absorbed a great deal of water, but the moisture was removed at very low temperature. In the samples with low open porosity (nos. 2 and 3) no D_2O was observed at any temperature, obviously because very little D_2O had been absorbed. No effect of closed porosity was observed.

III POROSITY MEASUREMENTS

The open and closed porosity of some of the UO_2 samples was determined using a standard technique. (5) The samples were infused with H_2O in the apparatus shown in Fig. 4. The samples were first heated in vacuum at 250°C for 24 hours.

They were then cooled and weighed. The samples were replaced in the apparatus and heated in vacuum for 24 hours to 250°C, then cooled and immediately immersed in H_2O. The samples were rolled in a lint-free towel to remove excess water and then weighed. The difference in the two weights divided by the dry weight is the open porosity. The closed porosity is determined by the suspension technique where samples are weighed while suspended in water. The difference between the suspended and dry weights divided into the dry weight gives the closed porosity. Four different samples were measured. All had been used in the previous investigation (4). The results are compared to these obtained at BNWL (Table 2), who used an immersion technique on the same samples to determine their porosity (6).

IV EXPERIMENTS OF DECEMBER, 1978

In order to observe high temperature release of D_2O it is believed that the UO_2 had to be infused with D_2 and/or D_2O at high temperature. Exxon Nuclear Co. prepared UO_2 pellets by sintering in a D_2-D_2O atmosphere at 1720°C (used in Runs 4, 5, and 7, see Table 1).

These pellets were heated up to 2740°C, very close to the melting point, to investigate the high temperature release of D_2O and D_2. The whole assembly above the heater approached temperatures of 600°C at the highest furnace temperatures. The high temperatures of the furnace was monitored with an optical pyrometer.

Four different runs were conducted (see Table 1). The first two, denoted as runs 4 and 5, were conducted using pellets sintered in D_2O/D_2 and the release of D_2O was monitored. Run 6 was a blank which used a pellet from the same batch as run 2 which had been sintered in H_2O/H_2 and had shown no appreciable release of D_2O in a previous outgassing. The last run, number 7 was conducted using the same pellets as used in runs 4 and 5, but the mass spectrometer was tuned to mass 4 to detect release of D_2.

Run 4 was conducted for 9.3 hours. The results are shown in Figs. 5 and 6. Because low temperature water release was not of great interest, the temperature of the crucible was raised rapidly to 910°C. The signal reached a maximum of 107 μg/hr within 1.8 minutes. The system was kept at this temperature until the signal decreased to 3 μg/hr. The rest of the outgassing was conducted with the temperature being raised in discrete steps, the signal reaching a maximum and then decaying to almost background. The signals observed during the 2440°C and 2640°C anneals were different in character from the lower temperature releases in that the signal did not immediately reach a maximum and then decay exponentially. This may be due to the sample changing phase with the opening of the closed pores or some other internal reorganization of the sample. On raising the temperature from 2700 to 2720°C no more D_2O was observed and the experiment was terminated. A total of 46 μg D_2O was released in the outgas with ~24 μg D_2O being released at temperatures <1000°C.

Run 5 was an attempt to duplicate run 4 with similar temperature increments. To see more temperature behavior the first outgas was at 550°C, with subsequent anneals of 910 and 1125°C. The other anneals were similar to those in run 4. The results of run 5 are shown in Fig. 7 and 8. The maximum signal was observed to be 38 μg/hr. Like the previous run, the very high temperature outgasses showed a different behavior with no immediate rise followed by decay. In addition, there was a sharp rise during the 2450°C outgas after an initial rise had been observed. This burst in signal was probably due to some change of phase or structure in the sample which caused a sudden D_2O release from the sample. After seeing no appreciable rise in signal at 2760°C the experiment was terminated after 6.5 hours of outgassing. The total D_2O observed was 17 μg with 7.5 μg of that above 1000°C. This is less than in run 4 with the difference due to some experimental uncertainties and possible differences in the samples.

Run number 6, which is the background run, is superimposed on Figs. 5 and 7 in dashed lines. It is seen that at the end of the outgas the signal had almost reached background.

In order to observe the release of D_2 from the samples in run 7 the mass spectrometer was tuned to mass 4. The mass spectrometer was calibrated with a known flow rate of deuterium prior to the outgassing experiment. The outgas was conducted similarly to that of runs 4 and 5 but for a much smaller time. Due to the much higher diffusivity of D_2 as opposed to D_2O, the anneals at individual temperatures were short because the D_2 was quickly released after the temperature had been raised. In addition, no D_2 was observed at low temperatures, so the temperature was quickly raised to 1620°C, then increased in discrete steps as before. The experiment was terminated after an outgassing of 161 minutes. As before, a sudden pulse of D_2 was observed during the middle of the 2590°C anneal. This burst occurred at about the same temperature as the D_2O burst in run 5 and may again be due to the sudden opening of closed porosity in the UO_2 sample. Accounting for the mass difference between D_2 and D_2O the signal levels shown in Fig. 9 and 10 have been multiplied by 5 to permit comparison with the D_2O release tests (runs 4 and 5). Nevertheless, the D_2 release rates are much lower than in the D_2O runs. A total of 7 μg D_2O (equivalent) was released, with all of it being observed at temperatures above 1000°C.

Although the melting temperature of UO_2 was not achieved in Runs 4-7, complete evaporation of the sample occurred. Because of the temperature gradient in the tungsten crucibles, the UO_2 was found after the experiments as a solid block ~4 cm above the bottom of the crucible where the pellets had been originally placed. This movement of the specimens is attributed to vapor transport of the UO_2, and insured complete release of D_2 or D_2O even though melting did not occur.

According to the results of Runs 4, 5, and 7 shown in Table 1, we conclude

that 2-4 μg D_2O/g UO_2 (including D_2O--equivalent of D_2) are retained by UO_2 pellets which are sintered in a D_2O/D_2 atmosphere. Because of the equilibrium $D_2 + \frac{1}{2}O_2 = D_2O$ which probably occurs during the release process, it is not known which component of the sintering gas is responsible for the retained deuterium. The D_2O/D_2 ratio of the gases released at temperatures > 1000°C is between 1 and 3, which is compatible with stoichiometric UO_2 only at temperatures > ∿ 2200°C. It therefore appears that complete equilibrium of the released D_2O with the oxygen potential of the fuel does not occur. The different rates of release of D_2O and D_2 suggest that the ratio of these two species is not controlled by decomposition processes occurring outside the specimens, i.e., on the crucible walls.

REFERENCES

1. C. N. Spalaris and F. H. Magerth, "Residual and Fission Gas Release from Uranium Dioxide", GEAP-4314 (1963).

2. A. S. Denovan, R. W. Ashley and T. H. Longhurst, "Internal Sources of Hydrogen in Unirradiated UO_2 Fuel Elements", AECL-4063 (1971).

3. H. M. Ferrari, "Nitrogen Release from UO_2 Pellets at Elevated Temperatures", Nuclear Science and Engineering, Vol. 17, (1963).

4. D. R. Olander, "Retention and Release of Hydrogen and Water Vapor by Uranium Dioxide", EPRI Final Report on Project RP 617-1 (1978).

5. Standard Test Method for Water Absorption, Bulk Density, Apparent Porosity, and Apparent Specific Gravity of Fired Whiteware Products, ASTM G373-72.

6. The assistance of P.E. Hart of BNWL in performing these measurements is gratefully acknowledged.

TABLE 1 SUMMARY OF UO_2 PELLET OUTGASSING EXPERIMENTS

Run No.	Date	Pellet Characteristics: Porosity,% open	Pellet Characteristics: Porosity,% closed	Pellet Characteristics: Sintering Conditions	Wt,g	D_2O loading	Max Temp °C	D_2O release, µg/g UO_2 T<1000°C	D_2O release, µg/g UO_2 T>1000°C	Comments
1	7/28			1450°C, 2 hrs	16.2	A	1800	17.5	0.3	
2	7/28			1750°C, 6 hrs	18.2	A	1700	0	0	
3	7/28			1750°C, 6 hrs	25.2	A	1700	0	0	
4	12/78			1700°C,6 hrs	14.2	B	2740	1.6	1.7	
5	12/78			1700°C,6 hrs	14.2	B	2760	1.7	0.5	
6	12/78			same as 2	9.1	none	2740	0.03	0.06	control
7	12/78			1750°C,6 hrs	14.2	B	2740	0	0.5	D_2 release

A sintered in H_2O/H_2; immersed in boiling D_2O prior to outgassing experiment

B sintered in D_2O/D_2 (40°C dew point)

C equivalent D_2O release = D_2 released x 5.

TABLE 2. POROSITY MEASUREMENTS

Sample	Open Porosity		Geometric Density	
	This work (%)	BNWL (%)	This work (g/cc)	BNWL (g/cc)
I	0.18	0.08	10.13	10.16
II	0.13	0.015	10.20	10.23
III	0.16	0.020	10.13	10.20
IV	0.22	0.04	10.21	10.22

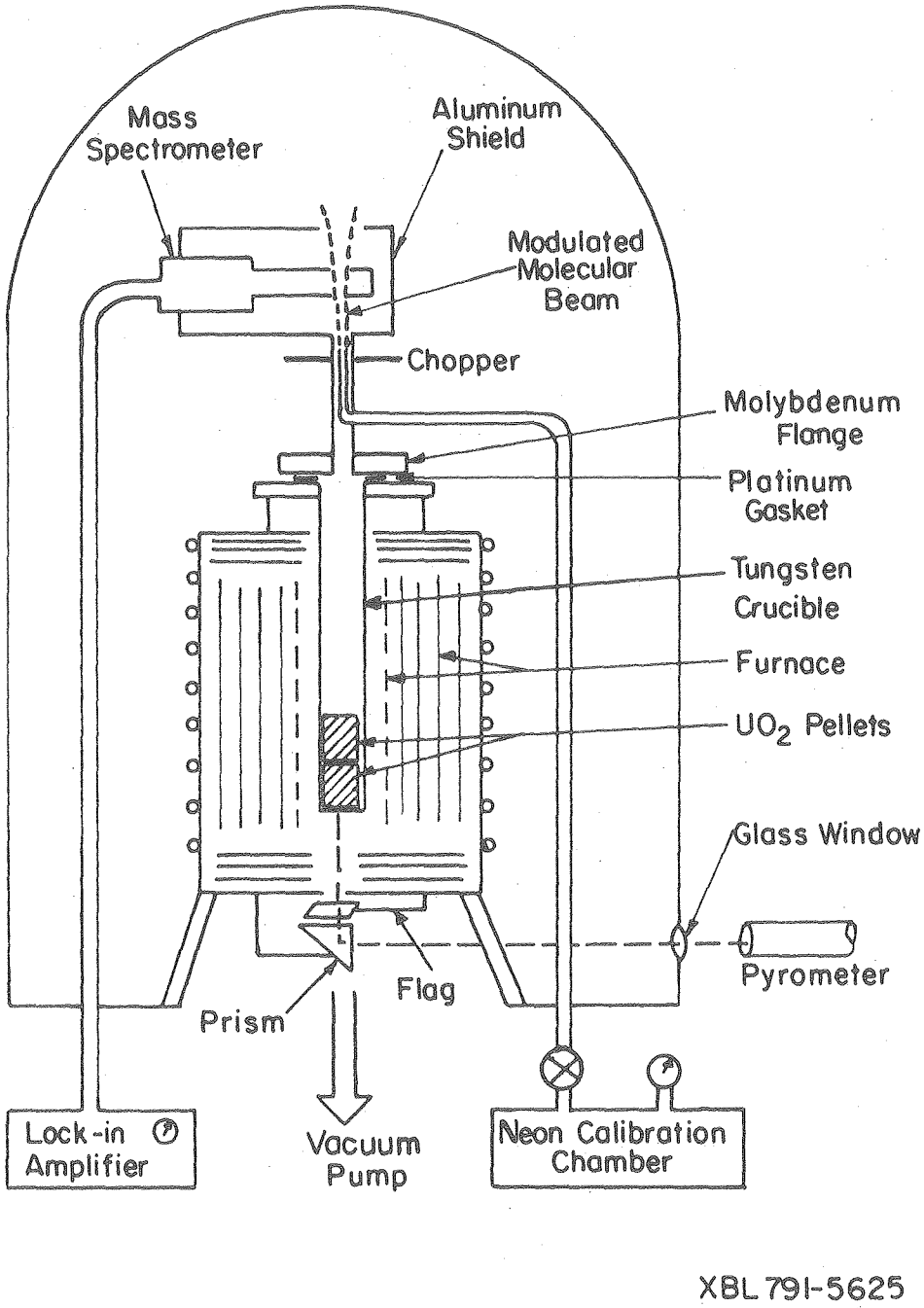

Figure 1. Apparatus for measuring release of gases from UO_2.

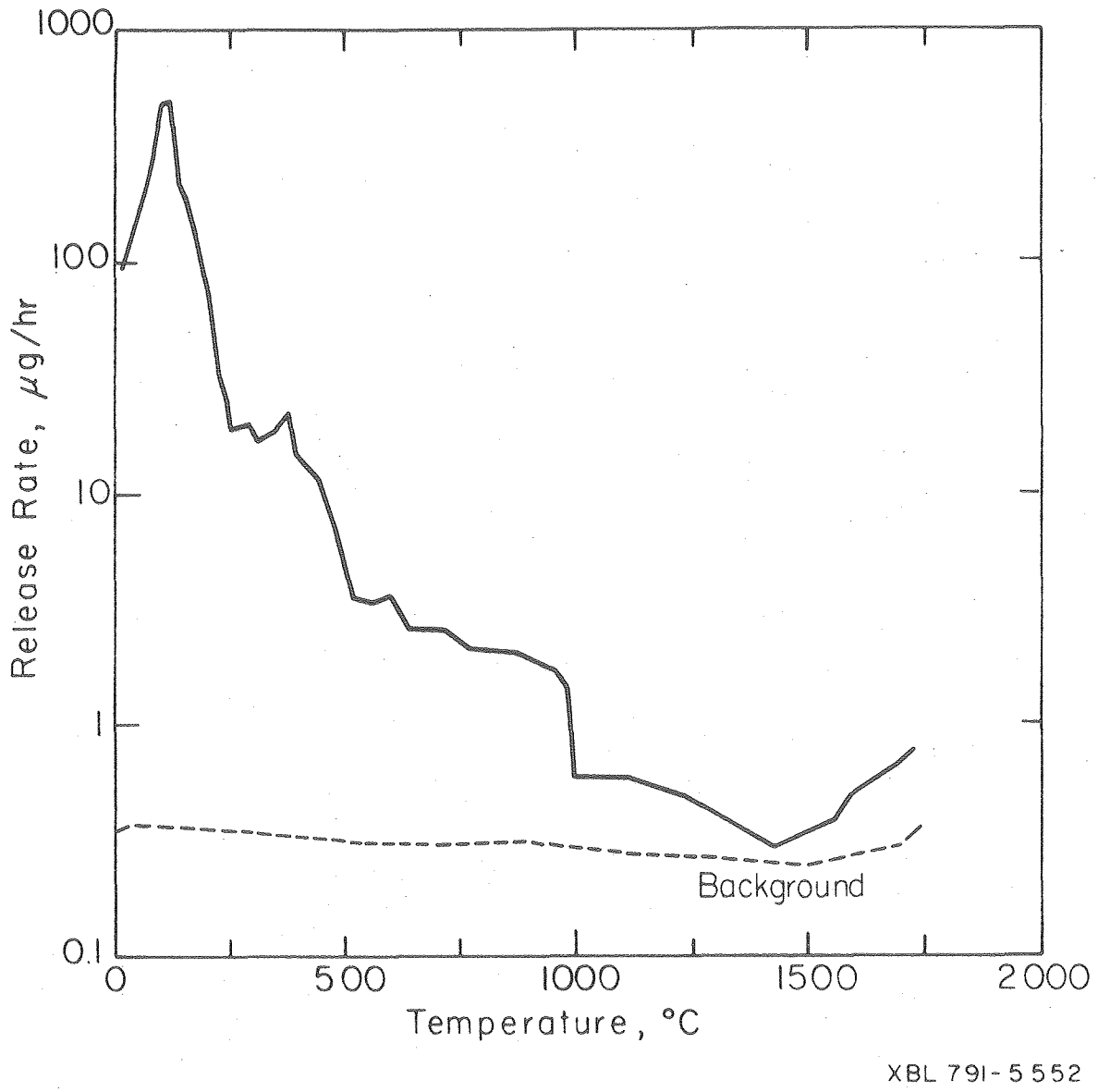

Figure 2. Rate of release of D_2O from UO_2 for Run No. 1.

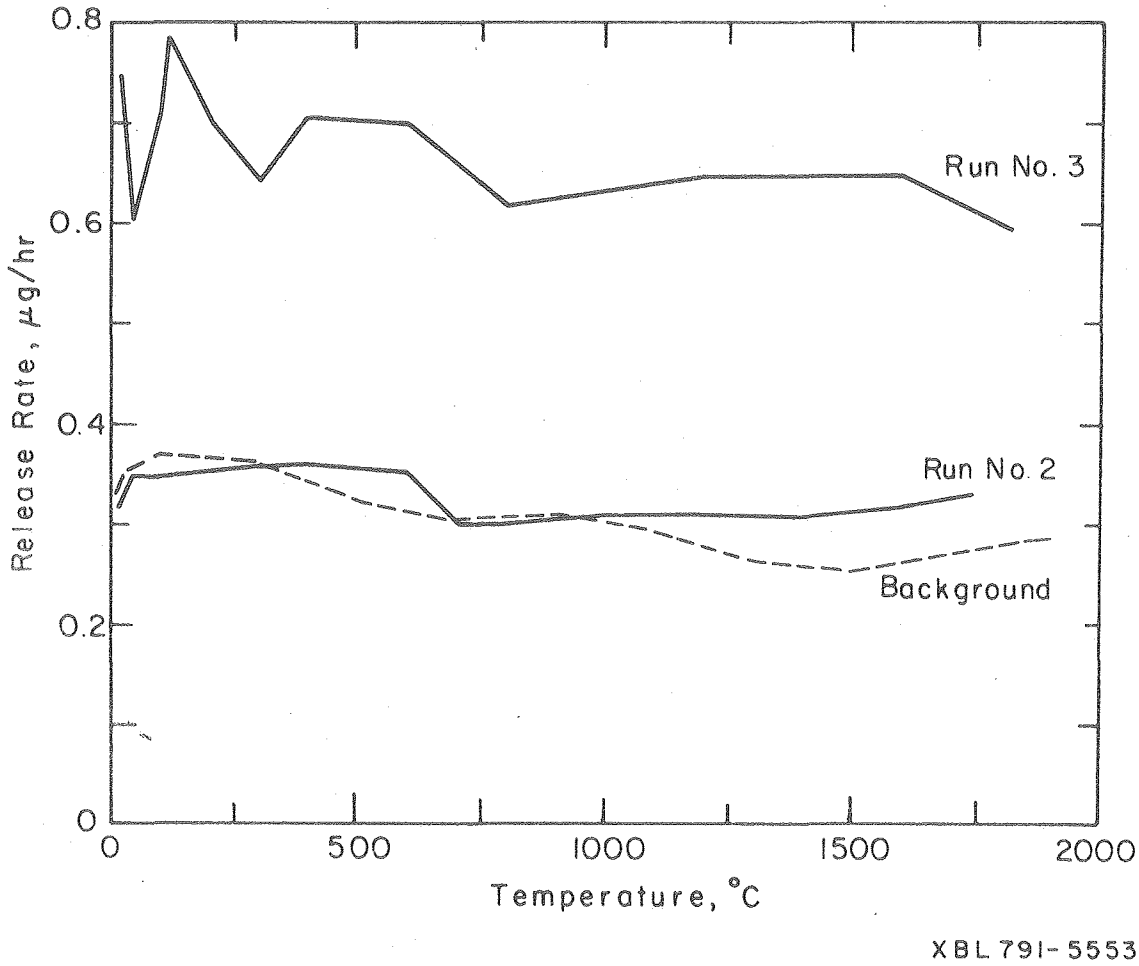

Figure 3. Rate of release of D_2O from UO_2 for Run Nos. 2 and 3.

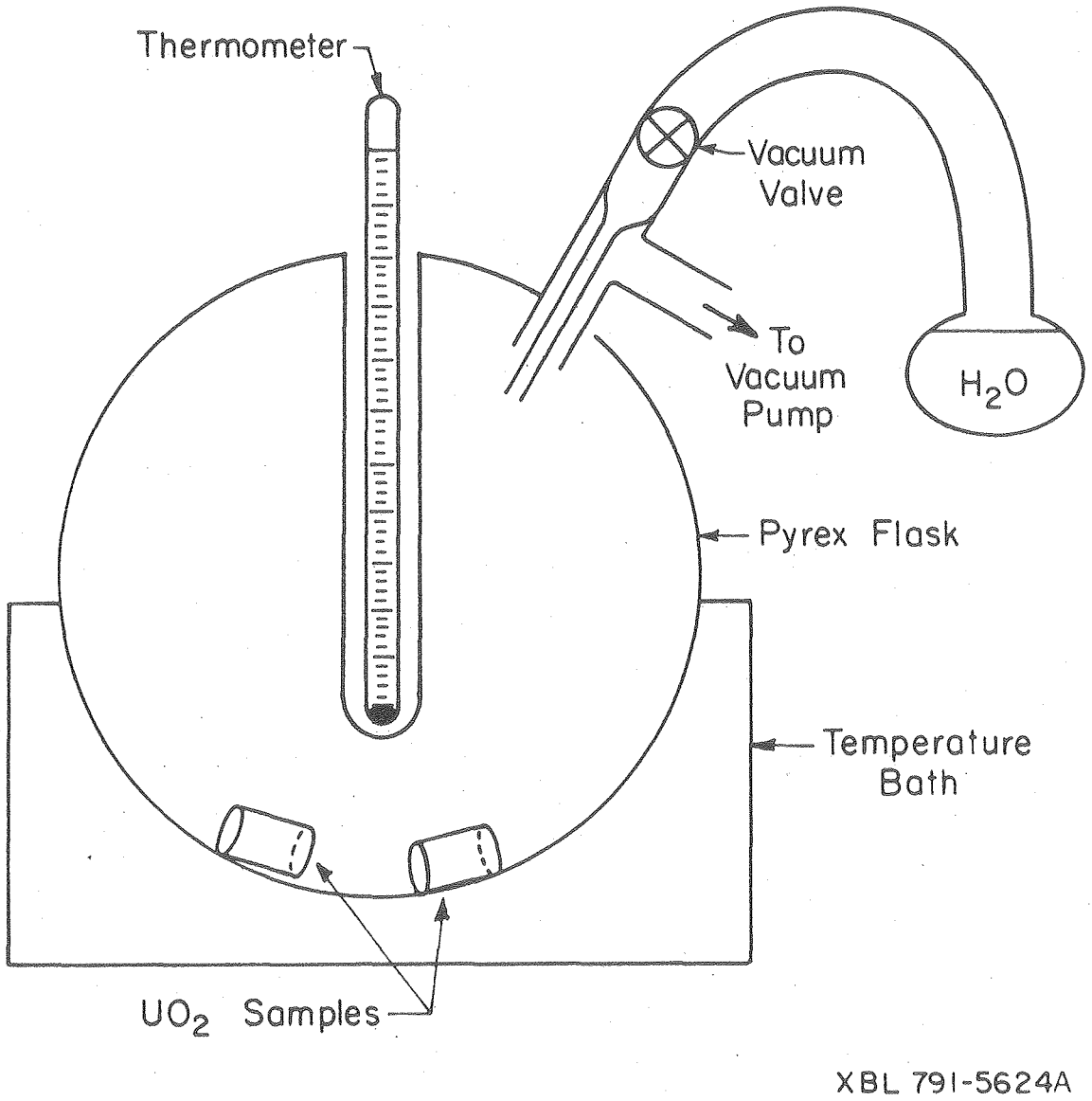

Figure 4. Apparatus for determining open porosity of UO_2 samples.

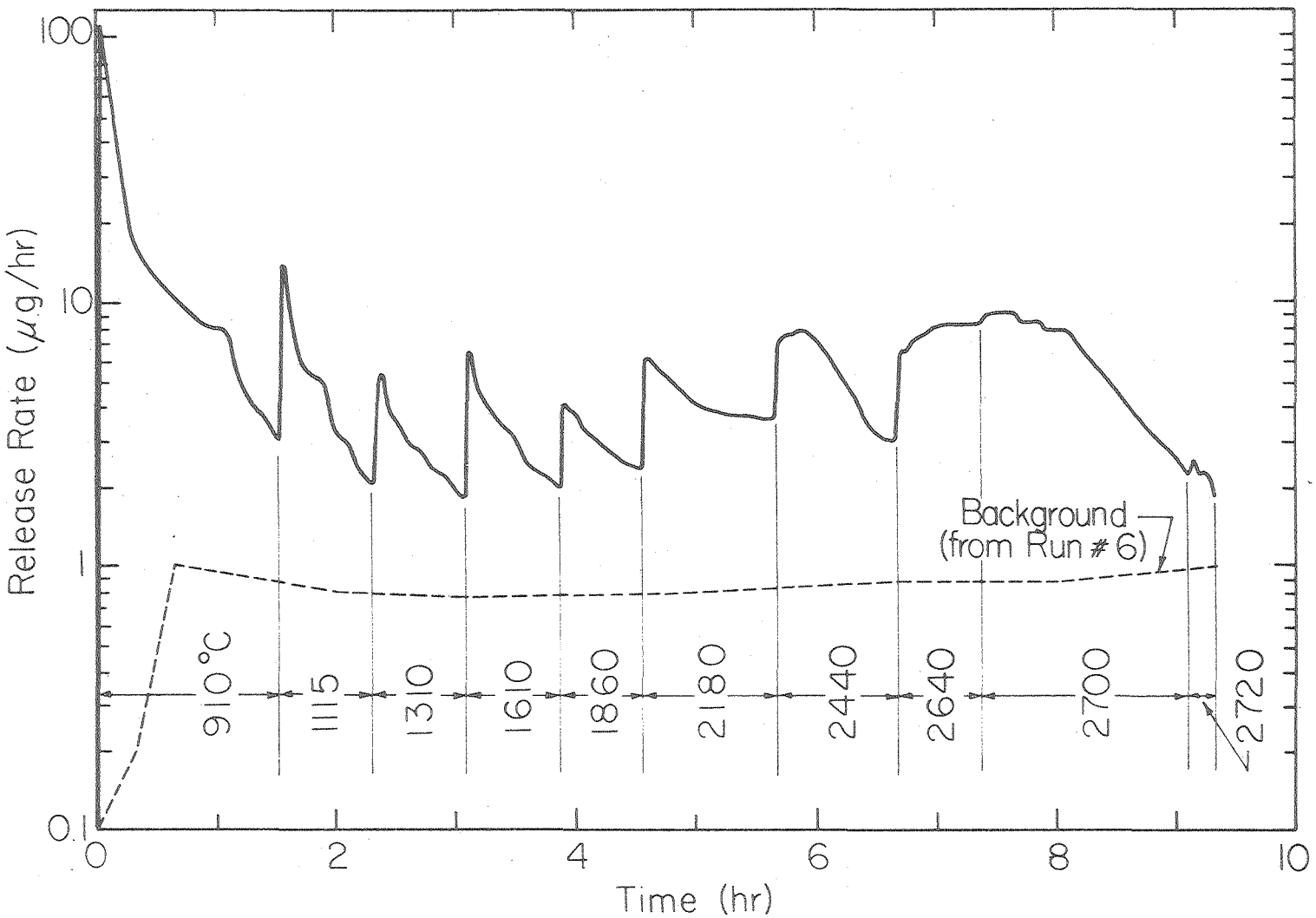

XBL791-5558

Figure 5. Rate of release of D_2O from UO_2 from Run No. 4

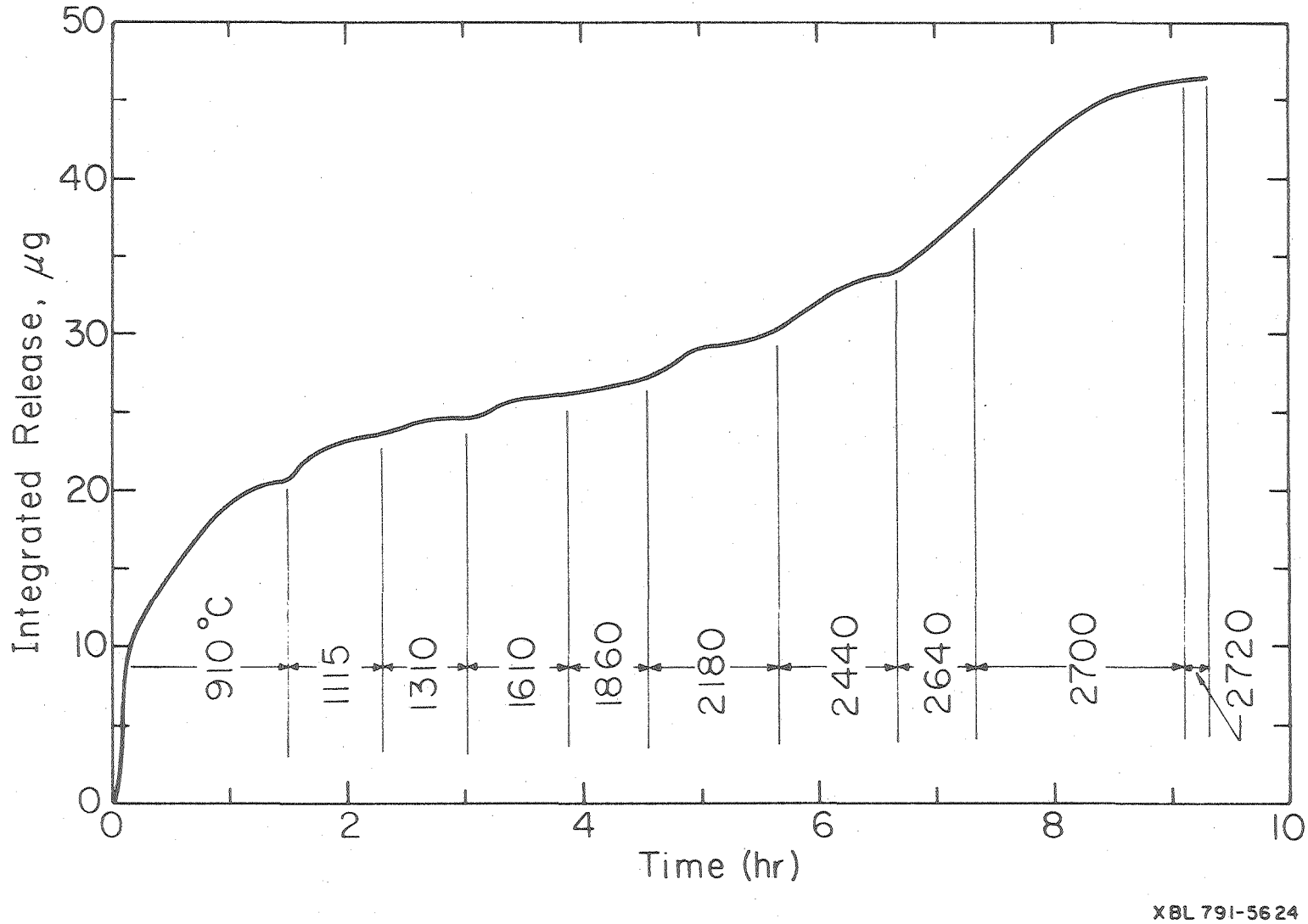

Figure 6. Cumulative release of D_2O from UO_2 for Run No. 4.

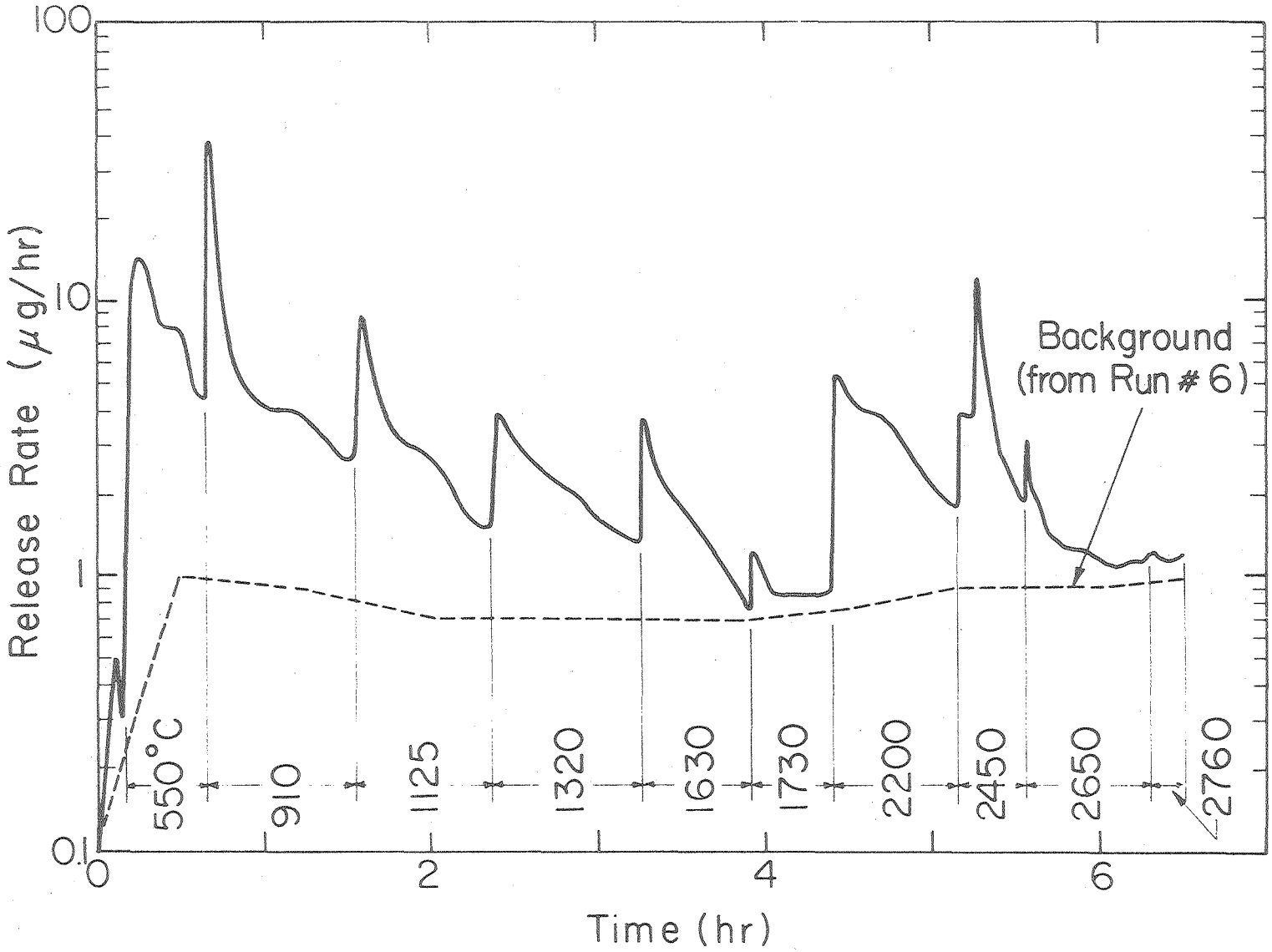

XBL791-5556

Figure 7. Rate of release of D_2O from UO_2 for Run No. 5.

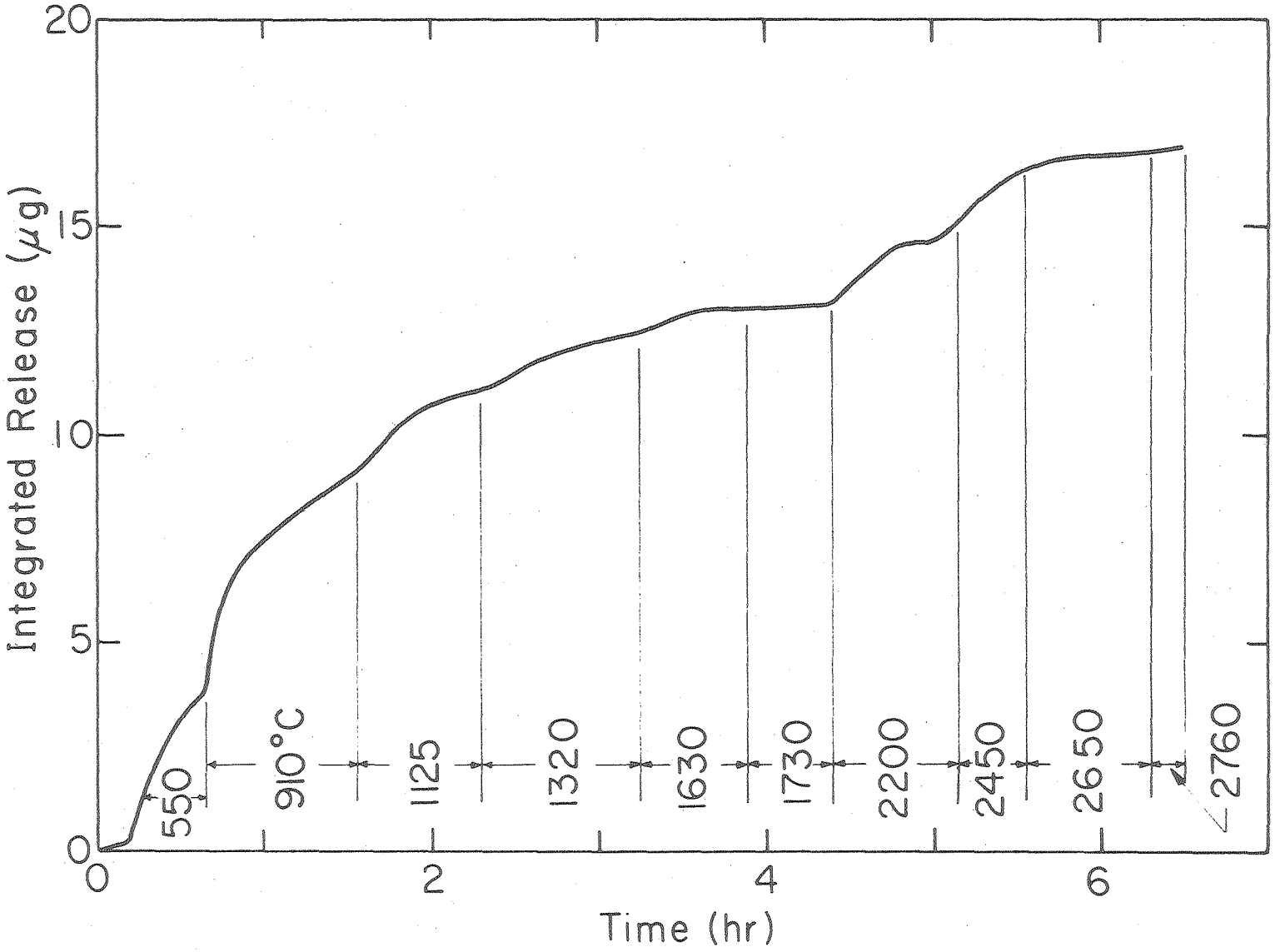

XBL791-5557

Figure 8. Cumulative release of D_2O from UO_2 for Run No. 5.

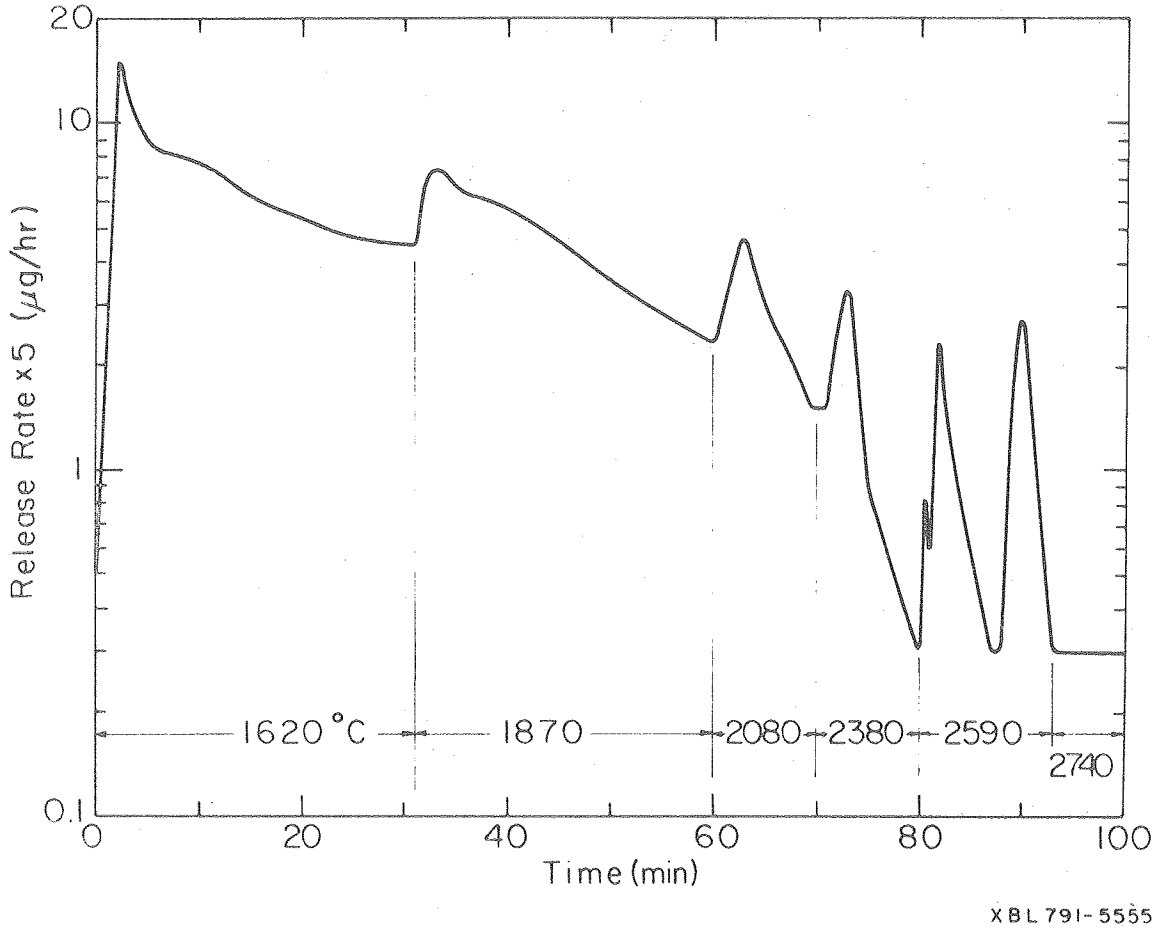

Figure 9. Rate of release of D_2 from UO_2 for Run No. 7.

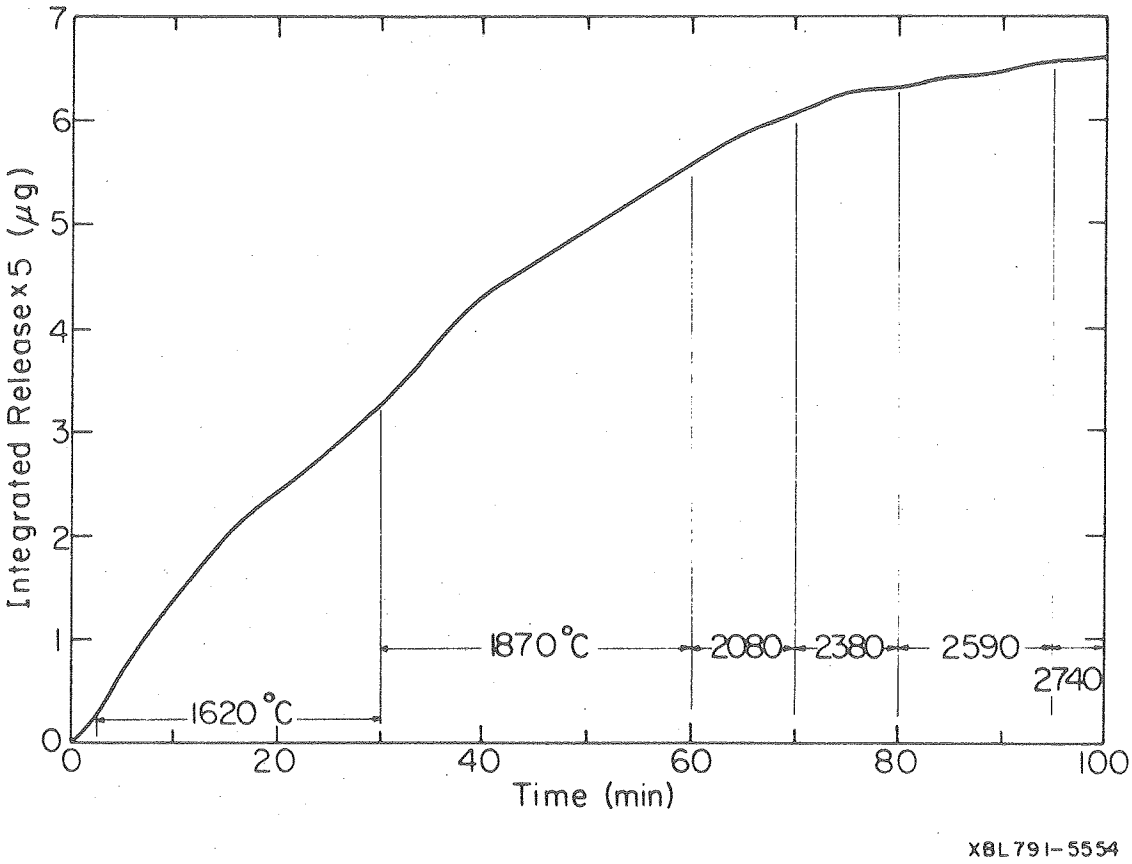

Figure 10. Cumulative release of D_2 from UO_2 for Run No. 4.

Thermal Gradient Migration of Metallic Inclusions in UO_2

by R.L. Yang

I. Introduction

The purpose of this experiment is to build a temperature gradient furance to study directly the migration mechanism of metallic fission product inclusions in UO_2 under the influence of a temperature gradient.

II. Experiment

A. Sample Preparation

The UO_2 used in this experiment is supplied by General Electric Vallecitos Lab. They are 95 $\pm$ 1% T.D. pellets, 1.3 cm long, with average grain size $\sim$ 15 μm. The pellets are centerless - ground to fit into a tungsten crucible leaving a radial gap about 20 μm between the specimen and the crucible. Two 0.1 cm thick wafers are sliced off each pellet using a thin diamond blade. Both faces of the UO_2 wafers and pellets are first ground on 400, 600 SiC paper, and finally polished with 6 μm diamond paste. A layers of 3-6 μm spherical tungsten powder inserted between the UO_2 wafers and pellet (Fig. 1). (Which simulate the metallic fission product inclusion). The tungsten powders are deposited on the UO_2 surfaces by the following method: Two drops of Triton x 100 (a dispersant) are added to 0.1 gram of tungsten powder in a 100 mℓ beaker, then 40 mℓ of methyl alcohol are added to the beaker. The beaker is then placed in an ultrasonic cleaner for 5 minutes to shake loose any agglomerated tungsten particles. After turning off the ultrasonic cleaner. A polished UO_2 pellet (or wafer) is placed in the liquid for $\sim$ 20 seconds to collect a layer of tungsten powder. After taking the UO_2 pellet out of the liquid, the pellet is allowed to dry slowly so that the separated tungsten powders do not coagulate during the drying

process. A typical photomicrograph of the UO_2 surface with tungsten powders on it is shown in Fig. 2

B. Sintering the Pellet-Wafer Assemblies

After tungsten powders are deposited, two UO_2 samples, each consisting of two UO_2 wafers, one UO_2 pellet and two layers of tungsten powder, separated by a molybdenum disk, are pressed into a molybdenum yoke for sintering (Fig. 3). To insure that the UO_2 is under high enough stress at sintering temperature to deform plastically, a 12.5 foot-pound torque is applied to the tantalum nut on the sintering yoke at room temperature before it is placed in the furance (Fig. 4). The lower part of the yoke is heated in the furnace to $\sim 2000^{\circ}C$ for 12 hours in 4% H_2 + 96% argon flowing at 2.5 C.F.H. The gas is passed through magnesium perchlorate trap (to eliminate water) and heated titanium chips (to eliminate water and oxygen) before it is fed to the bell jar. The purpose of this procedure is three-fold. 1. To provide an atomsphere capable of reducing the UO_2 to stochiometric or substochiometric uranium oxide, so that the urania will not oxidize the tungsten inclusions in the subsequent thermal gradient experiment. 2. To sinter the UO_2 to eliminate the gap between the UO_2 wafers and the pellet and to insure that the tungsten powder is embedded in the UO_2. 3. To densify the UO_2 sample.

Two pellet-wafer assemblies are sintered simultanously. One sample is used in the temperature gradient migration experiment and the other is sliced longitudinally, polished and checked microscopically to serve as a reference. A photomicrograph of a UO_2 pellet-wafer assembly after sintering is shown in Fig. 5.

The sintering procedure is successful in the following ways: 1. The urania is reduced so it does not ineract with the tungsten inclusions and the tungsten crucible. 2. The tungsten inclusions were well inbedded into UO_2 sample after the sintering process: no voids surround the tungsten particles which might impede the motion of tungsten inclusions during subsequent thermal gradient heat treatement. 3. The UO_2 sample undergoes a great deal of structual changes e.g., densification and grain growth, during the sintering process. The microstructure of UO_2 before and after the sintering process is shown in Fig. 6.

C. Thermal Gradient Furnace

Because UO_2 is heated in vacuum, it must be encapsulated to prevent excessive vaporization. The pellet-wafer assemblies are contained in a tungsten crucible with an integral top lid in which a 1 mm diameter, 6 mm long radial hole is drilled by spark discharge for temperature measurement.

A schematic diagram of the temperature gradient furnace is shown in Fig. 7.

After a sintered UO_2 pellet-wafer assembly (7) is inserted into the tungsten crucible (5) a tantalum collar (10) is electron beam welded to the bottom of the crucible. The tungsten crucicle, with the UO_2 sample in it, is then put on top of a tantalum push rod (12). The tantalum yoke(13) holds the tungsten crucible down while the stainless steel nut (16) pushes the tantalum rod against the bottom of UO_2 sample to keep it in close contact with the top of tungsten crucible. A W/W-Re therm-couple(11) is inserted into a slot in the tantalum push rod to measure the bottom temperature of UO_2 sample. To make the bottom temperature of UO_2 constant, a tantalum partial sleeve ring (9) is placed between the top of tantalum push rod and the tungsten crucible. Radiation shields

(8) and alumina insulators (14) are put between the tantalum yoke and the to tungsten crucible to keep the yoke cool.

The top of the tungsten crucible is heated by electron bombardment from a 0.020 inch tungsten filament which is ∿ 3 mm away from the top lid of the crucible. The bottom temperature is controlled by the tantalum push rod which acts as a heat sink. A stainless steel dome-shaped shield and rotary glass carousel is used to protect the viewing path from being coated, so that the top temperature can be measured by a pyrometer during the entire thermal gradient migration experiment.

D. Experimental Procedure

The experiment is carried out in a vacuum of 2×10^{-6} torr. When heating the specimen, the temperature is increased slowly to avoid cracking the UO_2. When the top temperature reaches ∿ 2650°C (at the black body hole in the crucible), the bottom temperature is ∿ 1200°C. There is a 1000°C/cm temperature gradient across the UO_2 sample. The sample is held under these condition for ∿ 10 hrs. Following the thermal gradient heat treatment, the specimen is sectioned longitudinally, ground with 120, 240, 320, 400, 600 grit SiC paper subsequently and finally polished with 6 μm and 1 μm diamond paste. Then, it is observed microscopically to determine the migration distance of the inclusion. The grinding/polishing process is repeated several times to obtain good statistical results by uncovering additional tungsten inclusions.

III Results

Several migration experiments were carried out in the new tungsten crucible. A sketch of the UO_2 specimen after thermal gradient experiment is shown in Fig. 8. A concave gap is formed between the UO_2 specimen and the tungsten lid. The gap arises from the porosity in UO_2 sample (which is not completely eliminated by the sintering step) and the residual cracks in between the UO_2 wafers and pellet. Both of these void source migrate

to the hot lid under the influence of thermal gradient. From the experiments, however, we saw some of the tungsten spheres migrate up to the hot region. However, migration is limited to powders on the periphery (∿ 2 mm way from UO_2 surfaces). A possible explanation for this is that due to the presence of the gap which was formed shortly after the temperature gradient is imposed, the temperature in the central region is significantly lower than at the periphery. Therefore, powders in the central region do not migrate.

IV. Future Work

1. The main problem is how to eliminate or reduce the gap caused by porosity migration to the top lid. There are two approaches to solve this problem. One is to melt UO_2 to obtain a porosity-free UO_2 sample. The other is to sinter the UO_2 sample instead of isothemally in temperature gradient in a fixture shown in Fig. 9. Under the temperature gradient, the porosity should migrate to the hot region, thus leaving high density UO_2 behind. By repeating this process several times, we hope to obtain a very low porosity UO_2 sample to be used in thermal gradient migration experiment.

2. A gold foil is to be inserted between the tantalum push rod and the bottom of UO_2 sample to insure the bottom temperature of UO_2 is constant.

3. A stainless steel spring (as the one shown in Fig. 9) is going to be used in thermal gradient migration experiment. When the UO_2 densified leaving a gap, the stainless spring will expand and close the gap between UO_2 and the lid of the tungsten crucible.

V. Temperature Profile Calculation

The two measured temperatures (T_1 at the hole in the top lid and T_2 at the bottom of the UO_2 pellet) and the heat flux input by E.B. heating serve as a basis for calculating the temperature distribution in the specimen. This requires numerical solution of the heat

conduction equation in the cylindrical coordinates with the non-linear boundary condition of radiation heat transfer. We calculate the temperature distribution using HEATING 5 code developed by Oak Ridge National Lab. A network of 40 lattice lines parallel to the cylindrical coordinates γ and z were laid across the specimen. The intersection of the lines form 420 nodes. The heat conduction equation is replaced by a system of finite difference heat balance equations at each node. To take into account of the difference in thermal conductivity in UO_2 and tungsten, and the various boundary conditions, we divided the specimen into 9 zones, with 4 different boundary conditions (Fig. 10). The thermal conductivity of tungsten is assumed to be constant at 1 W/cm°K in this temperature ranges. The thermal conductivity of UO_2 is allowed to vary with temperature. The accuracy of this calculation depends, among other things, on the validity of the following assumptions: 1. The specimen is in good thermal contact with tungsten crucible on the sides. This should be a very good assumption because UO_2 expands much more than tungsten container at this temperature and in addition any radial gap between the UO_2 and tungsten crucible would be closed by evaporation after very short heating periods. 2. Thermal radiation makes up most of the heat transfer in the gap between top and UO_2 sample and tungsten lid (region 4 in Fig. 10). This assumption is valid because the contribution from the conduction of the gas in the gap is small compared to radiation heat transfer at such high temperature. 3. The bottom temperature of UO_2 sample is constant (T_2).

An estimated heat flux q to the top lid is used to calculate the temperature distribution, then the calculated temperature at the black body hole (T_1) is compared with the value measured by optical pyrometer. Adjustments of the value of the input heat flux are made until the calculated value of T_1 and the experimentally measured value are the same. The temperature distributions in UO_2 specimen, with or without a top gap, are shown in Fig. 11 and 12 respectively.

1. filament holder
2. high purity alumina insulator
3. stainless steel post
4. tungsten filament
5. tungsten crucible
6. black body hole ($\ell/d \simeq 5$)
7. sintered UO_2 pellet
8. tantalum radiation shield
9. tantalum partial sleeve
10. tantalum collar
11. W-Re thermocouple
12. tantalum push rod
13. tantalum yoke
14. alumina washer (heat insulator)
15. molybdenum collar
16. stainless steel nut
17. shield
18. rotary glass shield
19. pyrometer
20. brew furnace

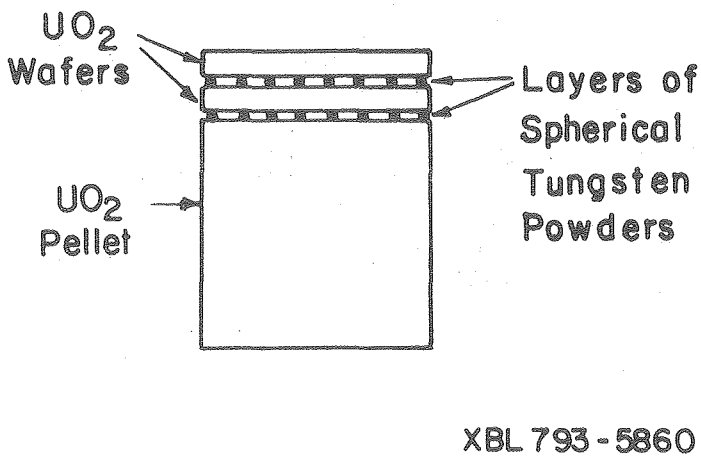

Figure 1. UO_2 pellet-wafer assembly.

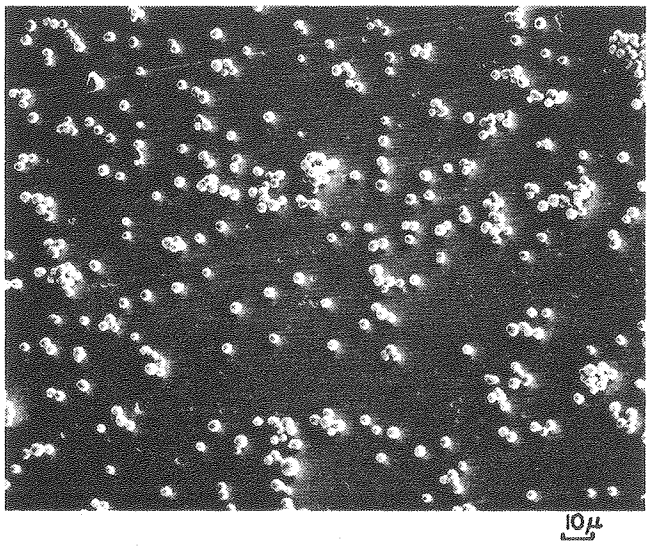

Figure 2. Photomicrograph of UO_2 surface with tungsten powders deposited on the surface.

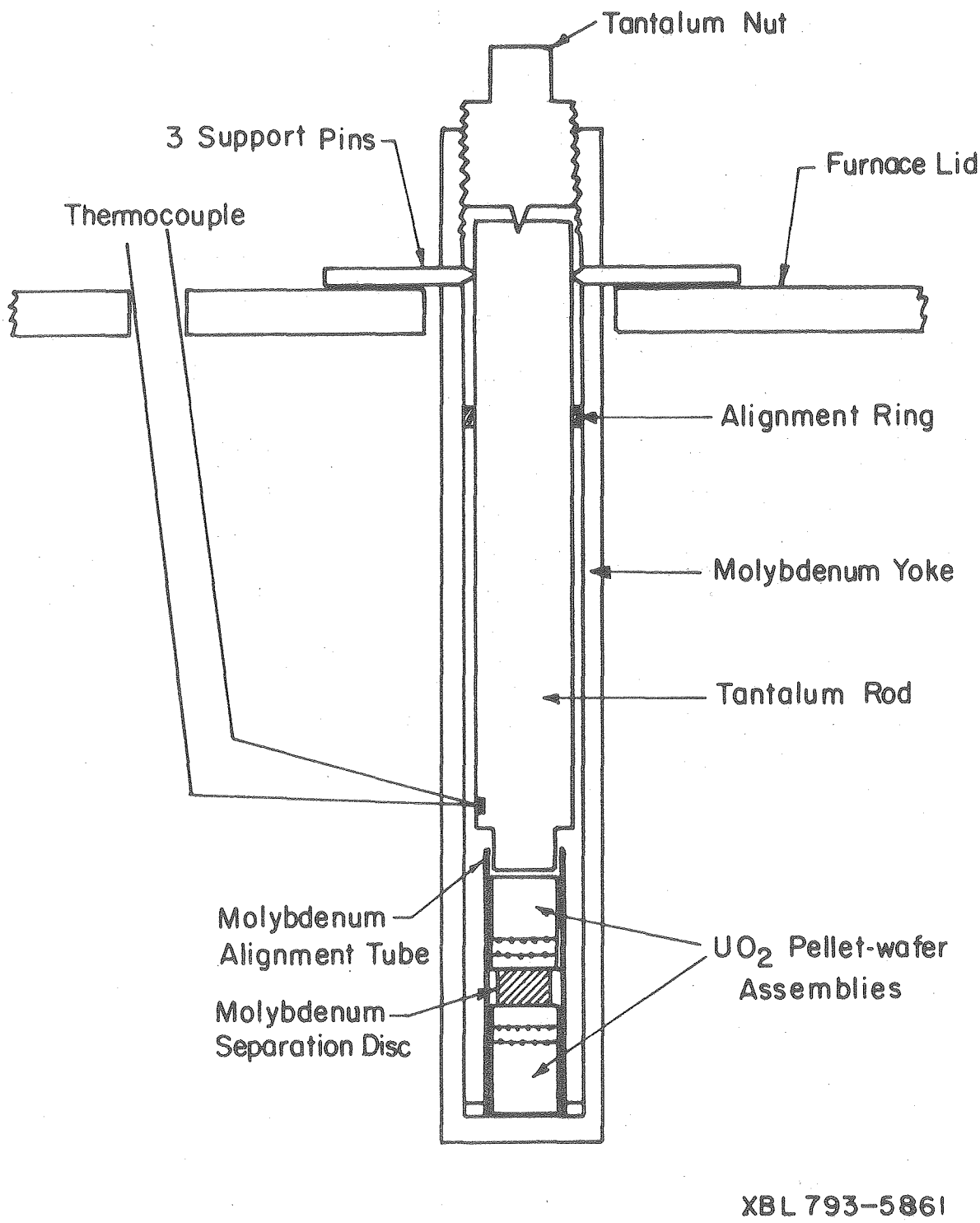

Figure 3. Sintering yoke for UO_2 pellet-wafer assembly.

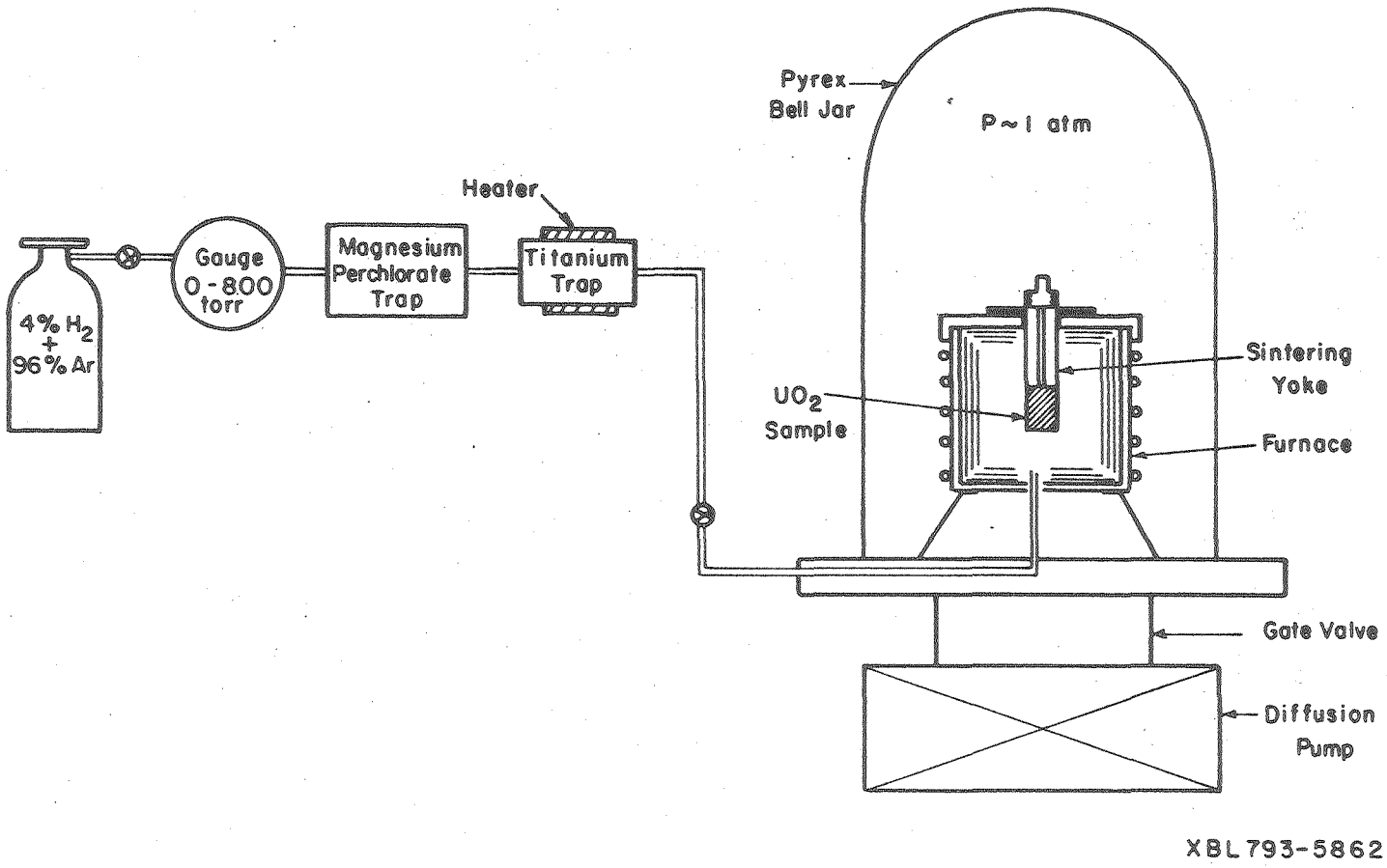

Figure 4. Apparatus for UO_2 sintering.

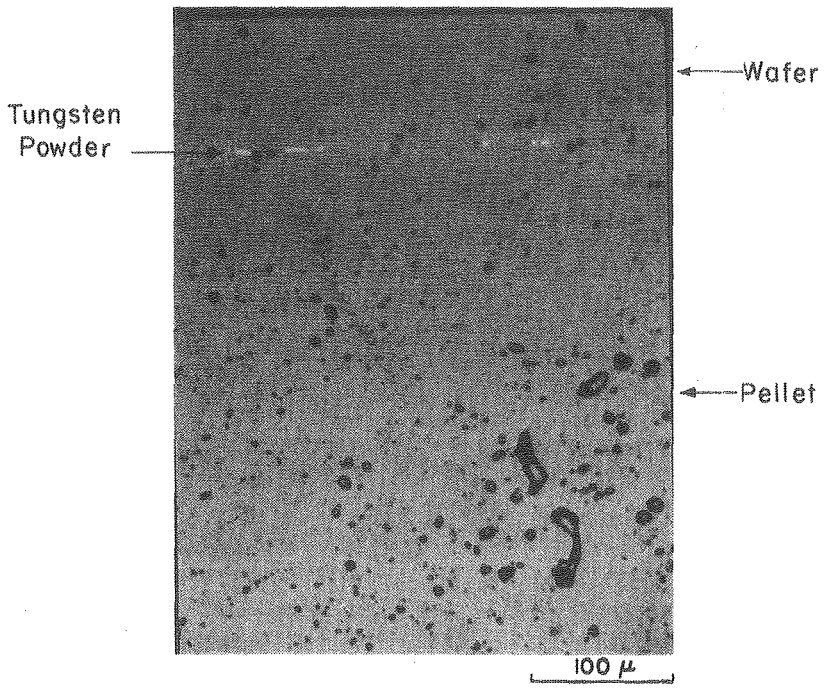

Figure 5. Microstructure longitudinal cross section of UO_2 pellet-pellet-wafer assembly after sintering.

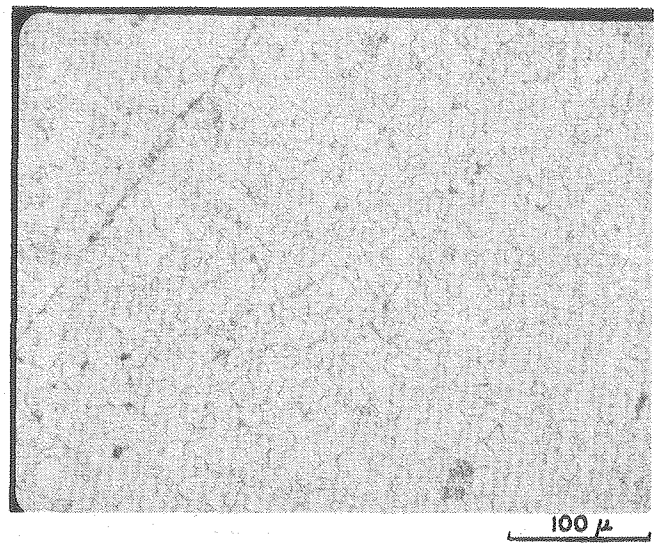

(a) Microstructure of UO_2 Before Sintering

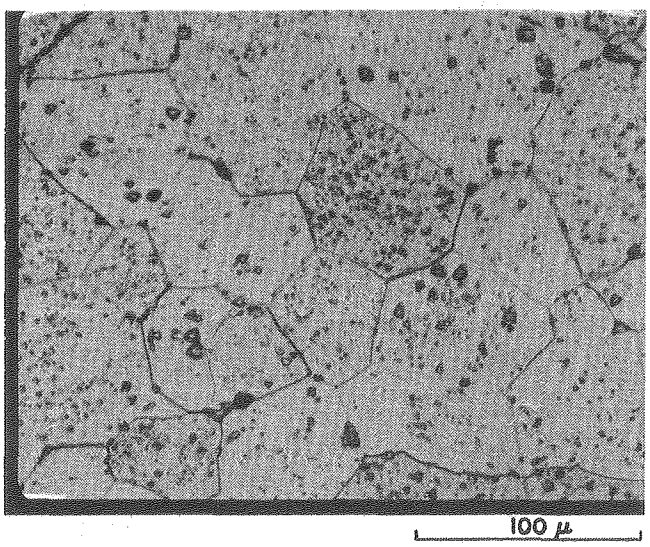

(b) Microstructure of UO_2 After Sintering

Figure 6. Microstructure of UO_2 before and after sintering process.

XBB 802-2315

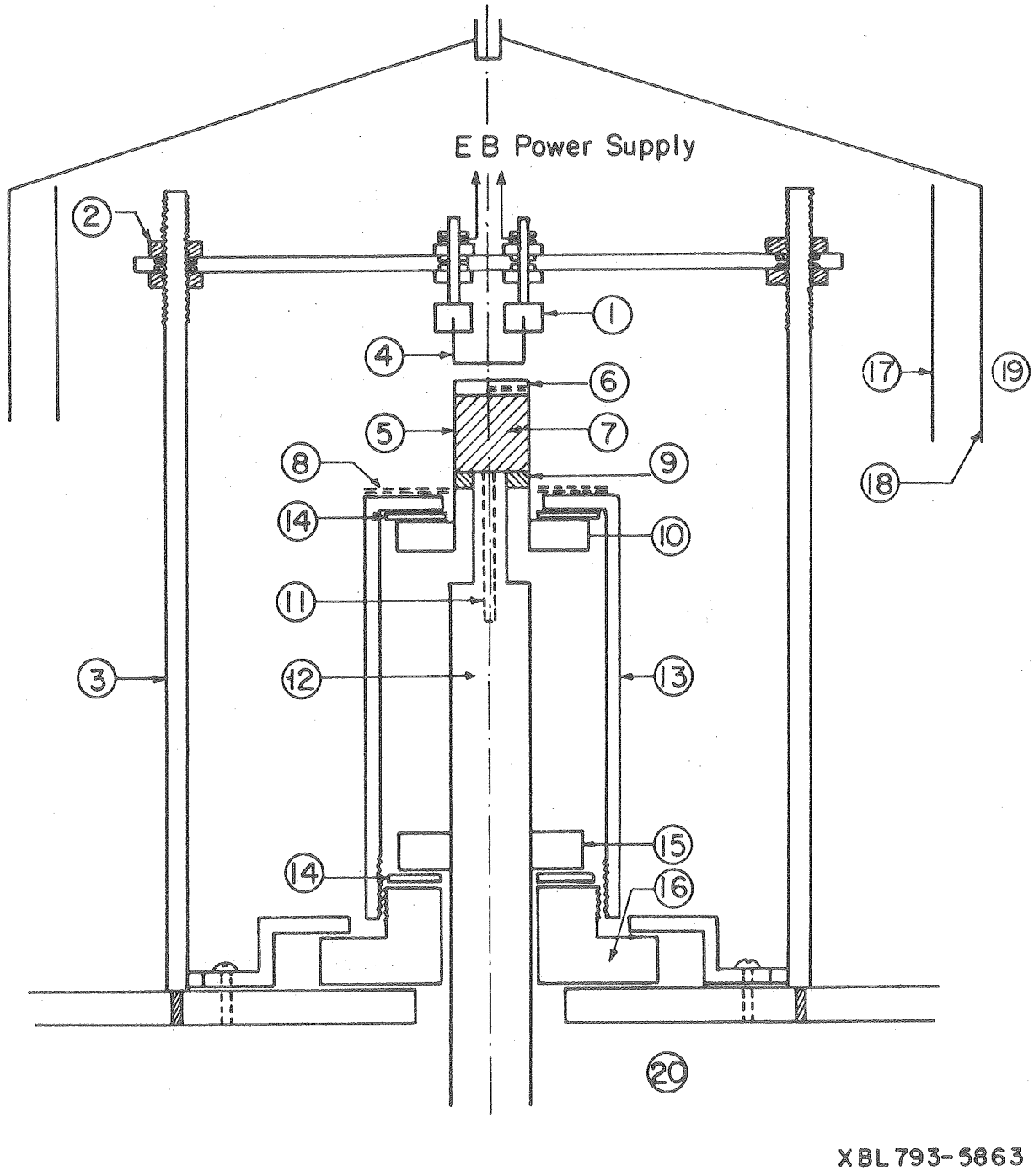

Figure 7. Temperature gradient furnace.

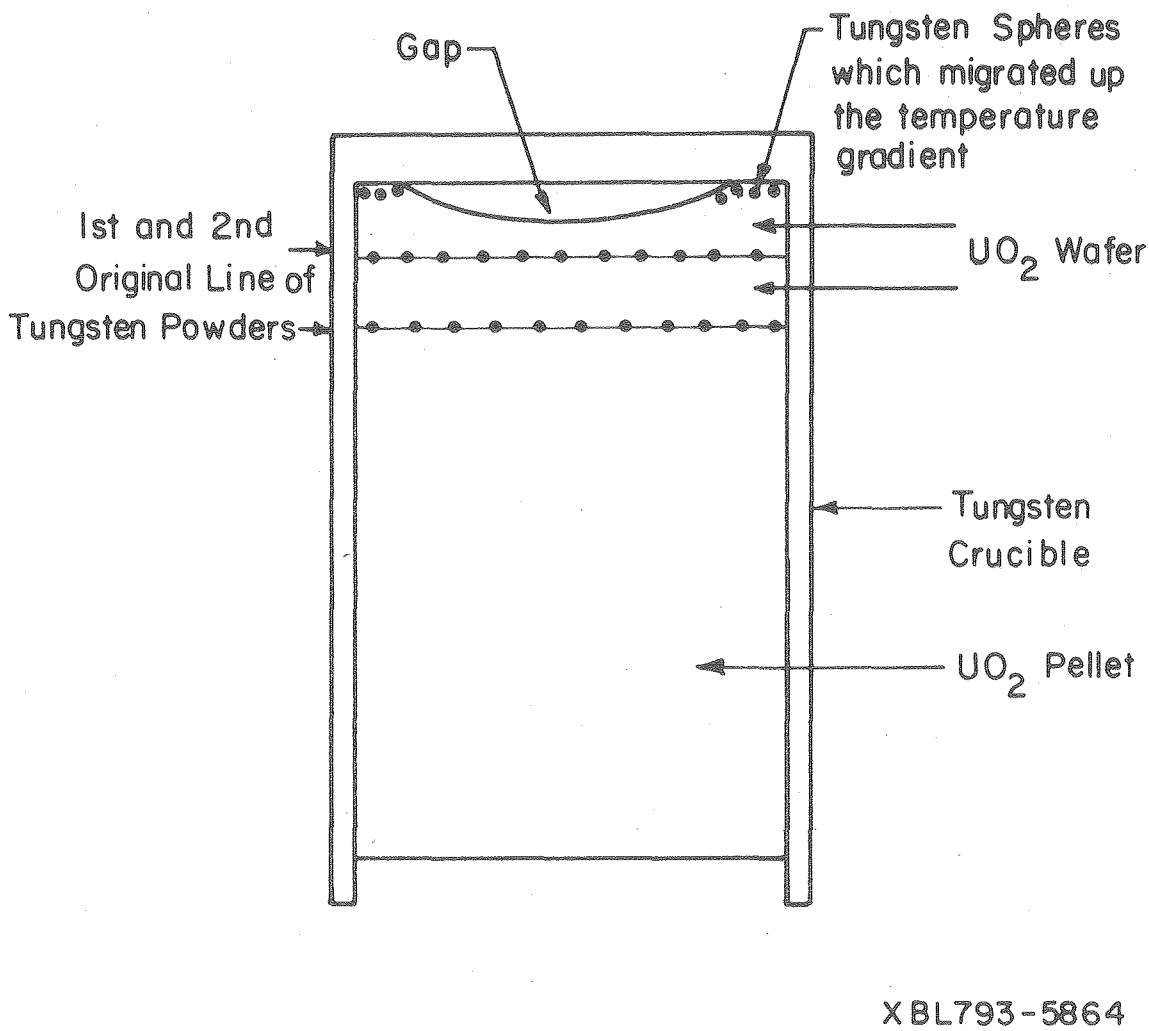

Figure 8. Schematic diagram of UO_2 pellet-wafer assembly after thermal gradient migration experiment.

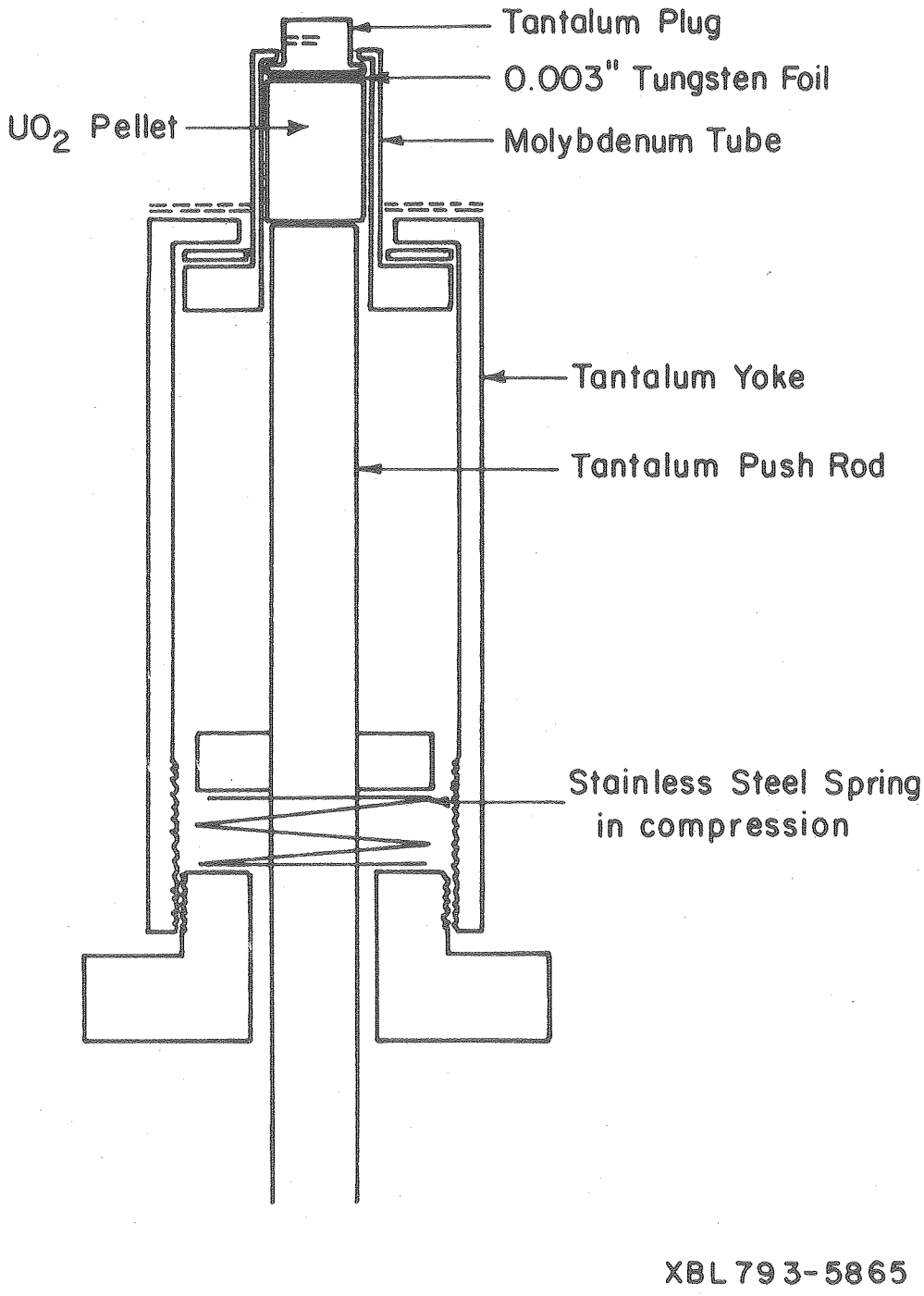

Figure 9. Fixture to reduce the porosity in UO_2.

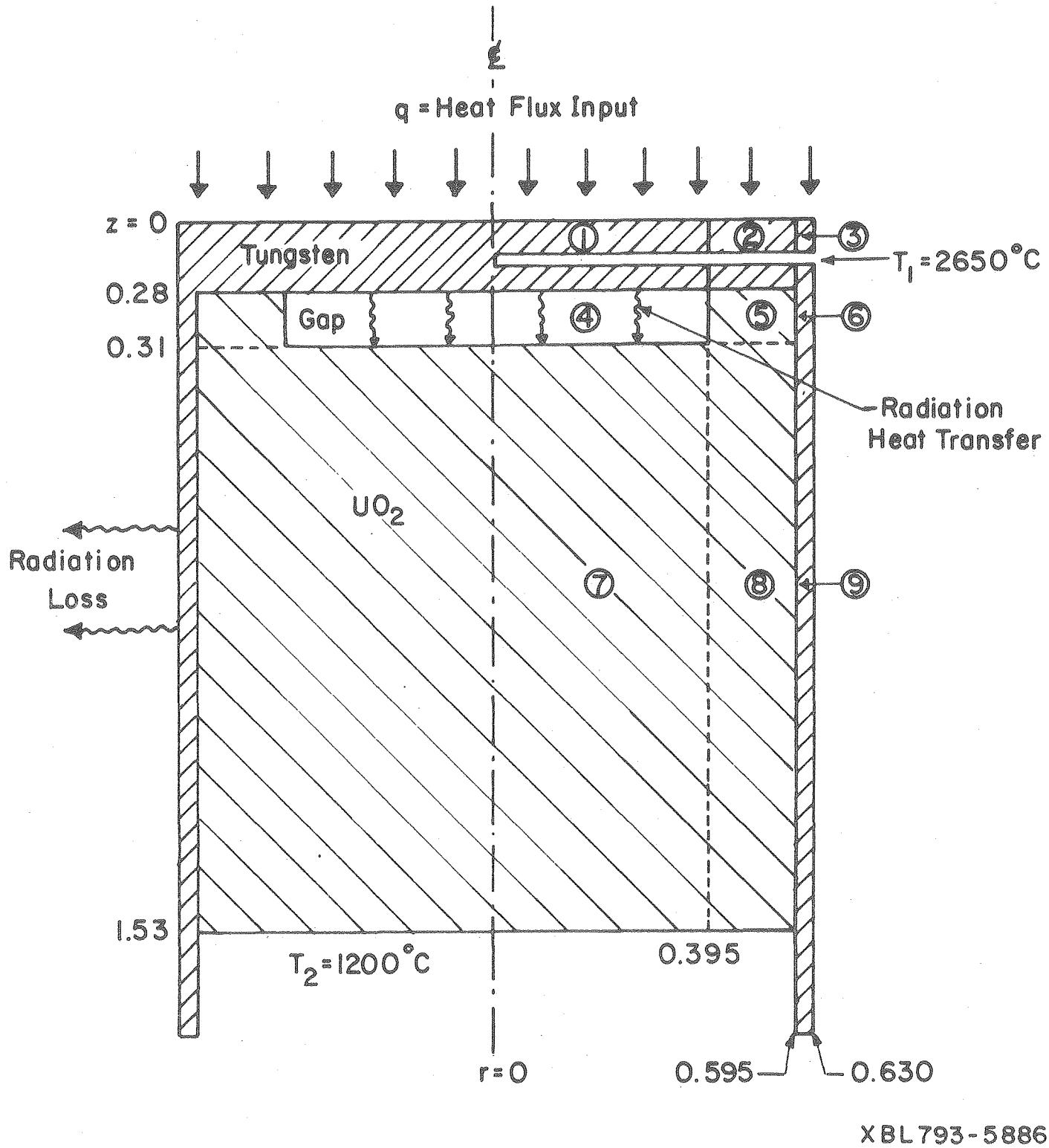

Figure 10. Cross section of the specimen for temperature calculation (all dimensions in cm).

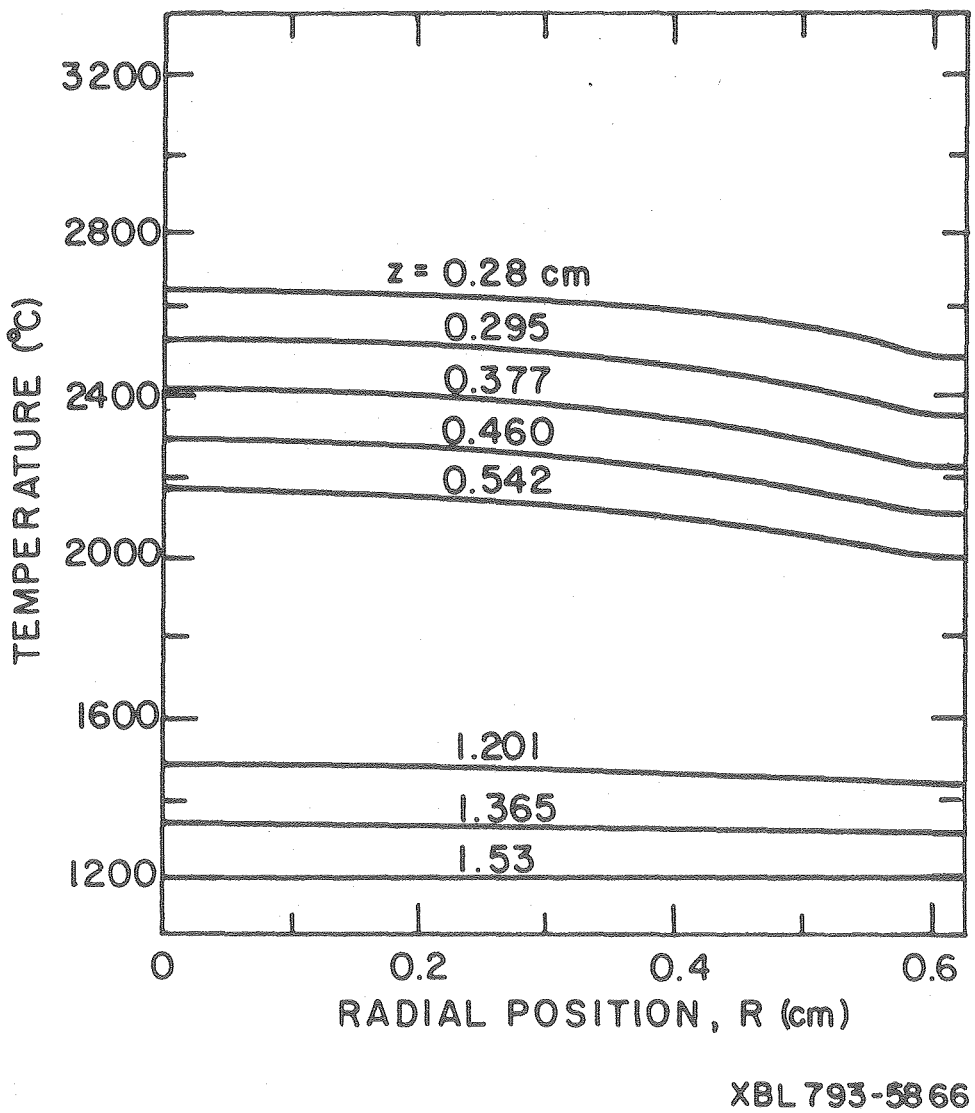

Figure 11. Temperature distribution in UO_2 when top of UO_2 is in good thermal contact with tungsten lid (no gap).

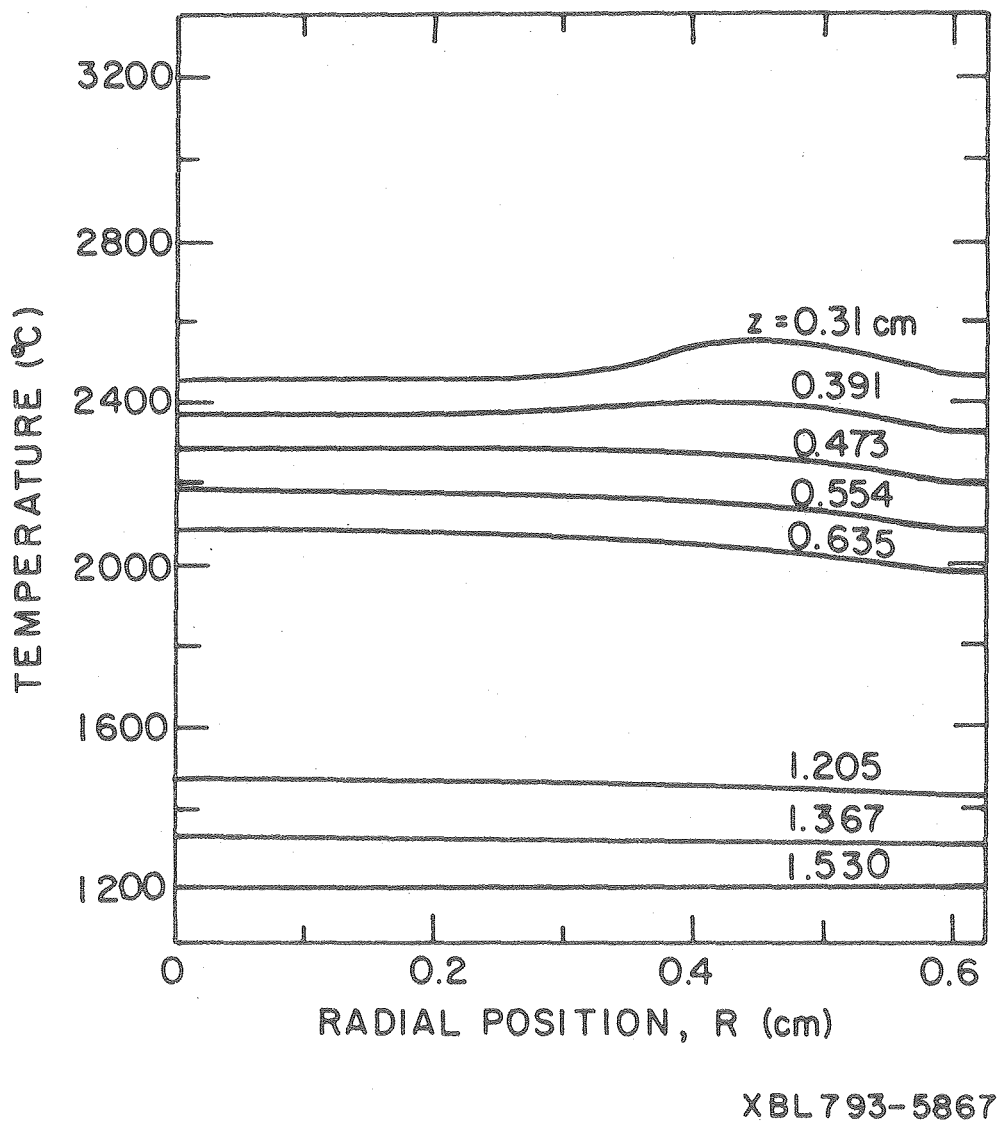

Figure 12. Temperature distribution in UO_2 when there is a central void formed on top of UO_2 (geometry of Fig. 10).

Molecular Beam Studies of Atomic Hydrogen Reduction of Oxides

By Douglas F. Dooley

I. Introduction

Oxide insulator materials exposed to the hot hydrogen fuel of a CTR plasma will be subject to chemical as well as physical corrosion (1,2). To better understand the nature of the chemical attack, the reduction reactions of thermal atomic hydrogen with refractory oxides, UO_2 and $A\ell_2O_3$, are being studied by the modulated molecular beam method (3,4).

Although previous studies have made qualitative observations of atomic hydrogen/oxide reactions and other have predicted corrosion rates based on thermodynamic equilibrium models, there is little information about the elementary reaction steps which comprise the overall reduction reaction and the values of the associated rate constants. This information can be obtained by modulated molecular beam mass spectrometry, which is a technique of studying heterogeneous chemical reactions in a detail not attainable by conventional chemical kinetic experiments.

II. Experimental

D_2 rather than H_2 is used as a reactant. The lower mass spectrometer noise background at the D_2O (mass 20) peak compared to the H_2O (mass 18) peak allows measurement of lower reaction probabilities in less time with high precision.

A palladium "diffusion filter" has been installed on the reactant deuterium gas line to eliminate beam impurities.

A beam monitor mass spectometer has been installed on the molecular beam axis. Monitoring the beam indicates that the impurity content is below the detection limit (1 part in 10^5). The purpose of the direct - line mass spectrometer is to measure the D to D_2 ratio in the reactant beam directly rather than by the other mass spectrometer in the system which detects scattered

species only. The D/D_2 ratio in the reflected beam, in general, is not the same as in the reactant beam since recombination of D atoms to form D_2 may occur on the target surface.

In the past, the deuterium effusion oven was supplied with power for electrical resistance heating through a single vacuum feedthrough which eventually failed due to current in excess of rated capacity. The subsiquent loss of vacuum resulted in damage to the tungsten oven assembly. Dual feedthroughs of greater current capacity were installed to prevent recurrence of this problem.

The reactant atomic deuterium beam formed by effusion from the thermal dissociation source is modulated by a mechanical chopper prior to striking the surface of the heated oxide target. Severe reaction between the $A\ell_2O_3$ samples, and tantulum target holders occured at high temperature. To prevent such reactions, the oxide targets are now wrapped in rhenium foil prior to clamping in the target holder.

D_2O molecules as well as other species produced by the reduction reaction are defected by a mass spectrometer. The output signal is processed by a lock-in amplifier and analyzed to determine the mechanism of the reduction reaction.

III. Results

Results of the UO_2/H investigation indicate that reduction of UO_2 by atomic hydrogen proceeds by the production of water vapor and hypostoichiometric urania:

$$\frac{1}{x} UO_2 + 2H \rightarrow \frac{1}{x} UO_{2-x} + H_2O_{(g)} \qquad (1)$$

The reaction probability for water production as a function of UO_2 temperature was measured at a fixed H atom beam intensity and modulation frequency. The reaction probability increased from the noise level at low temperatures to a high temperature plateau at 1300°C. At the plateau, approximately one H atom out of seven striking the surface undergoes reaction and returns to the gas phase as water.

Data on the reduction of $A\ell_2O_3$ have been taken at temperatures from 300°C to 2040°C (the melting point) at a fixed equivalent hydrogen pressure ($\sim 5 \times 10^{-4}$ torr). Water production by reduction of $A\ell_2O_3$ remains too low to be defected (i.e., reaction probability $\lesssim 10^{-4}$) until the temperature is greater than 1300°C. The low reactivity of $A\ell_2O_3$ to H below 1300°C is consistent with the other findings (5,6). At higher temperatures, both H_2O and $A\ell$ are detected by the mass spectrometer as gaseous reaction products. Other products, such as $A\ell O$, $A\ell H$, $A\ell OH$, $A\ell OH$, $A\ell_2O$, and $A\ell_2OH$ were sought but not found. The reaction probability increases with temperature, but remains two orders of magnitude below the maximum value for the UO_2/H reaction. These data indicate that the reaction proceeds according to:

$$\frac{1}{3} A\ell_2O_3 + 2H \longrightarrow \frac{2}{3} A\ell(g) + H_2O(g) \qquad (2)$$

Contray to UO_2, the range of deviation from stoichiometry of $A\ell_2O_{3-x}$ is probably so small that even slight reduction of $A\ell_2O_3$ requires production of the metal. Because alumina cannot be rendered hypostoichiometric, its reduction by atomic hydrogen results in production of aluminum metal.

IV Discussion

The relative ease which UO_2 is reduced by atomic hydrogen compared with Al_2O_3 is due to two factors. The first is related to the thermochemistry of reactions (1) and (2). Although thermodynamics cannot be invoked to predict chemical kinetics, one can at least expect that thermochemically favored reactions should be the most readily observed.

A rough estimate of the ease of reducing Al_2O_3 by atomic hydrogen can be obtained from the standard free energy change of reaction (2), which is:

$$\Delta G^{o}_{(2)} = -\frac{1}{2}\Delta G^{o}_{Al_2O_3} - 2\Delta G^{o}_{H} + \Delta G^{o}_{H_2O} \qquad (2a)$$

where ΔG^{o}_{H} and $\Delta G^{o}_{H_2O}$ are the standard free energies of formation of atomic hydrogen and water, respectively, and $\Delta G^{o}_{Al_2O_3}$ is the free energy of formation of alumina (per mole of O_2). The equilibrium oxygen pressure over the Al/Al_2O_3 couple is given by: $\Delta G^{o}_{Al_2O_3} = RT\ln p_{O_2}$ where R is the gas constant. The comparable quantity of UO_2 is the oxygen potential $\overline{\Delta G_{O_2}}$. Hence, the standard free energy change for reaction (1) for small x is:

$$\Delta G^{o}_{(1)} = -\frac{1}{2}\overline{\Delta G_{O_2}} - 2\Delta G^{o}_{H} + \Delta G^{o}_{H_2O} \qquad (1a)$$

The free energy change of reaction (1a) at 1000 K is -310 kJ/mole (for x = 0 in UO_{2-x}), whereas that of reaction (2a) is -71 kJ/mole. The fact that both of these free energy changes are substantially negative suggest that, barring kinetic restrictions, reduction of the oxides should proceed in atomic hydrogen. However, urania should be easier to reduce that alumina because removal of oxygen from UO_2 does not require production of the metal.

The second feature which favors efficient reduction of UO_2 but not of Al_2O_3 is the oxygen diffusivity. As the reduction reaction proceeds at the surface, oxygen depletion of the surface layers will quickly stop the reaction unless oxygen can be transported to the surface from the bulk solid. The self-diffusion coefficient of oxygen in hypostoichiometric urania has not been measured, but is probably very large (7), whereas oxygen migration in alumina is smaller, probably by many orders of magnitude (8). Consequently, oxygen transport from the interior of the solid to the reacting surface takes place easily in UO_2 but in alumina, evaporation of the aluminum metal reaction product appears to be necessary to prevent a protective scale of Al from halting the surface reduction process.

V. Future Experiments

1) Fresh $A\ell_2O_3$ samples have been prepared for study at the high temperatures where the reaction probability is large. Although the mass spectrometer noise background at these elevated temperatures makes measurements difficult, attempts will be made to obtain precise phase lag as well as reaction probability data since both these quantities are necessary to properly interpret the reaction mechanism.

2) Some observers have reported enhanced reduction reactions of $A\ell_2O_3$ in the presence of H_2O vapor (9,10). The effect of H_2O vapor on the reduction reaction will be investigated by the use of a doser to provide a D.C. source of H_2O vapor to the $A\ell_2O_3$ surface.

The previous UO_2 samples studied were probably hyperstochiometric due to prolonged exposure to atmospheric oxygen and moisture. Furture experiments will investigate the effect of changing oxygen-to-metal ratio upon reactivity by using both stochiometric UO_2 and hypostochiometric UO_2 polycrystalline wafers as targets. A single-crystal UO_2 target will also be studied to determine the effect of grain boundries and crystal orientation upon reactivity. During these experiments, the possibility of the existeance of volitile uranium - bearing species from the UO_2 reduction reaction will be checked.

References

1. D.M. Gruen, Chemical Effects of Thermonuclear Plasma Interactions With Insulator and Metal Surfaces. J. Nucl. Mater., 53, 220 (1974).

2. J.W. Tester, R.C. Feber, C.D. Herrick, Heat Transfer and Chemical Stability Calculation For Controlled Thermonuclear Reactor (CTR), USAEC Report LA 5328-MS (July 1973).

3. R.H. Jones, W.J. Siekhaus, J.A. Schwurz and D.R. Olander, Investigation of Gas-Solid Reaction By Modulated Molecular Beam Mass Spectrometry, J. Vac. Sci. and Technol. 9, 1429 (1972)

4. D.R. Olander, Heterogeneous Chemical Kinetics by Modulated Molecular Beam Mass Spectrometry, J. Colloid and Interface Sci., 58, 169 (1977)

5. S. Veprek, Private Communication (June 16, 1978).

6. L.J. Trostel, Jr. Stability of Alumina and Zirconia in Hydrogen Ceramic Bull. 44, pp. 950 - 952 (1965).

7. G.E. Murch and R.J. Thorn, J. Nucl. Mater. 71, 219 (1978).

8. Y. Oishi and W.D. Kingery, J. Chem. Phys. 33, 480 (1960).

9. D.J.M. Bevan, J.P. Shelton, J.S. Anderson, Properties of Some Simple Oxides and Spinels at High Temperatures, J. Chem. Soc. (condon) 1948, pp. 1729-41.

10. F. Sandford, E. Ericsson, Effect of Composition of Kiln Atmosphere In The Firing Of Refractory Oxides, J. Am. Ceram. Soc. 41 (12) 527-31 (1958).